Supporting Information

Holmium(III) molecular nanomagnets for optical thermometry exploring the luminescence re-absorption effect

Junhao Wang,[a] Jakub J. Zakrzewski,[b] Mikolaj Zychowicz,[bc] Veacheslav Vieru,[cd] Liviu F. Chibotaru,[c] Koji Nakabayashi,[a] Szymon Chorazy,*[b] and Shin-ichi Ohkoshi*[a]

[a]Department of Chemistry, School of Science, The University of Tokyo, 7-3-1 Hongo, Bunkyo-ku, Tokyo 113-0033, Japan. [b]Faculty of Chemistry, Jagiellonian University, Gronostajowa 2, 30-387 Krakow, Poland. [c]Theory of Nanomaterials Group, Katholieke Universiteit Leuven, 3001 Leuven, Belgium. [d]Faculty of Science and Engineering, Maastricht University, Paul-Henri Spaaklaan 1, 6229 EN Maastricht, The Netherlands.
Corresponding authors: chorazy@chemia.uj.edu.pl; ohkoshi@chem.s.u-tokyo.ac.jp

Experimental details

Materials

Holmium(III) chloride hexahydrate ($HoCl_3 \cdot 6H_2O$, CAS: 14914-84-2, Wako Pure Chemicals Industries, Ltd), yttrium(III) chloride hexahydrate ($YCl_3 \cdot 6H_2O$, CAS: 10025-94-2, Wako Pure Chemicals Industries, Ltd), 4-pyridone (4-hydroxypyridine, 4-pyridinol, CAS: 626-64-2, Sigma-Aldrich), potassium hexacyanocobaltate(III) ($K_3[Co(CN)_6]$, CAS: 13963-58-1, Sigma-Aldrich), potassium cyanide (KCN, CAS: 151-50-8, Wako Pure Chemicals Industries, Ltd), rhodium(III) chloride ($RhCl_3 \cdot xH_2O$, Rh: 38–40%, CAS: 20765-98-4, Sigma-Aldrich), and potassium hexacyanoiridate(III) ($K_3[Ir(CN)_6]$, CAS: 20792-41-0, abcr GmbH) were used without further purification. Potassium hexacyanorhodate(III), $K_3[Rh(CN)_6]$, was synthesized from $RhCl_3$ and KCN using a previously reported method.[S1–S2]

(S1) J. Wang, S. Chorazy, K. Nakabayashi, B. Sieklucka and S. Ohkoshi, *J. Mater. Chem. C*, 2018, **6**, 473–481.

(S2) M. C. Read, J. Glaser, I. Persson and M. Sandström, *J. Chem. Soc. Dalton Trans*., 1994, 3243–3248.

Synthetic procedures and basic physicochemical characterization

Synthesis of 1 (Ho–Co compound)

A precursor solution I was prepared by dissolving 91 mg (0.24 mmol) of $HoCl_3 \cdot 6H_2O$ and 230 mg (2.4 mmol) of 4-pyridone in 1 mL of distilled water. The solution I was heated to reach the boiling point, and it was quickly added to the aqueous solution II (1 mL) containing 80 mg (0.24 mmol) of $K_3[Co(CN)_6]$. The resulting mixture was vigorously stirred at room temperature for several seconds which was followed by suction filtration to remove the small amount of an amorphous precipitate. The obtained clear solution was left for crystallization in the darkness. After a few days, yellowish block crystals of **1** appeared. They were collected by suction filtration, washed with the water and ethanol, and dried on the air overnight. The formula of **1**, **$\{[Ho(4\text{-pyridone})_4(H_2O)_2][Co(CN)_6]\} \cdot 2H_2O$**, was determined by a single-crystal X-ray diffraction (SC-XRD) method. It was confirmed by the CHN elemental analysis and TGA studies (Fig. S2). The obtained product was stable on the air as proven by the CHN elemental analysis and a powder X-ray diffraction (P-XRD) method (Fig. S5). Yield: 113 mg, 57% (based on Ho). The IR spectrum for **1** with the interpretation is given in Fig. S1 and Table S1. Elem. anal. Calcd. for $Ho_1Co_1C_{26}H_{28}N_{10}O_8$ (M_W = 832.4 g·mol^{-1}): C, 37.5%; H, 3.4%; 16.8%. Found: C, 37.4%; H, 3.4%; N, 16.7%.

Synthesis of 2 (Ho–Rh compound)

The synthetic route towards compound **2** was generally analogous to those presented above for **1** with using $K_3[Rh(CN)_6]$ instead of $K_3[Co(CN)_6]$. However, we found that the crystallization of **2** is less efficient and takes much longer time than observed for **1** which can be explained by the lower reactivity of $K_3[Rh(CN)_6]$. Therefore, the crystallization process was optimized, and the final synthetic procedure is as follows. Two precursor solutions (I and II) were prepared. The solution I contained 45 mg (0.12 mmol) of $HoCl_3 \cdot 6H_2O$ and 115 mg (1.2 mmol) of 4-pyridone, dissolved together in 0.3 mL of distilled water. The solution II contained 60 mg (0.16 mmol) of $K_3[Rh(CN)_6]$ dissolved in 0.3 mL of distilled water. The solution I was heated up to the boiling point, and quickly added to the freshly prepared solution II. It was followed by the vigorous stirring for several seconds. The resulting mixture was filtrated and left for crystallization in the dark. After several days, light yellow block crystals of **2** were collected, washed with water and ethanol, and dried on the air overnight. The composition of **2**, **$\{[Ho(4\text{-pyridone})_4(H_2O)_2][Rh(CN)_6]\} \cdot 3H_2O$**, was indicated by a SC-XRD method and confirmed by the CHN elemental analysis confronted with the TGA experiment (Fig. S2). Note that the third crystallization water molecule per {HoRh} unit could not be detected within the results of the SC-XRD analysis, however, its presence is strongly suggested by the results of the TGA and CHN elemental analyses. It can be ascribed to the very weakly bonded water molecules adsorbed in the remaining channels of the supramolecular framework of **2**. This effect was repeatedly detected in the Rh^{III}-containing samples of **2** and their magnetically diluted derivatives of **2@Y** (see below). The obtained compound was stable on the air as depicted by the CHN elemental analysis and a PXRD technique (Fig. S5). Yield:

20 mg, 19% (based on Ho). The IR spectrum for **2** with the interpretation is given in Fig. S1 and Table S1. Elem. anal. Calcd. for $Ho_1Rh_1C_{26}H_{30}N_{10}O_9$ (M_W = 894.4 g·mol^{-1}): C, 34.9%; H, 3.4%; 15.7%. Found: C, 34.8%; H, 3.5%; N, 15.8%.

Synthesis of 3 (Ho–Ir compound)

The synthetic procedure to obtain compound **3** was analogous to those presented above for **1**, however, the highest synthetic yield and the quality of the crystalline product were achieved by starting from smaller portions of the precursors. In the optimized synthesis, two precursor solutions (I and II) were prepared. The solution was prepared by dissolving 45 mg (0.12 mmol) of $HoCl_3·6H_2O$ together with 115 mg (1.2 mmol) of 4-pyridone in 0.5 mL of distilled water. The solution II was prepared by dissolving 56.4 mg (0.12 mmol) of $K_3[Ir(CN)_6]$ in 0.5 mL of distilled water. Then, the solution I was heated up to the boiling point, and added hot to the freshly prepared solution II. After the energetic stirring for several seconds, the resulting mixture was filtrated and left undisturbed for crystallization in the dark. After a few days, yellowish block crystals of **3** were collected, filtrated, washed with water and ethanol, and dried on the air overnight. The formula of **3**, **$\{[Ho(4\text{-pyridone})_4(H_2O)_2][Ir(CN)_6]\}·2H_2O$**, was determined by a SC-XRD method and confirmed by the CHN elemental analysis supported by the TGA experiment (Fig. S2). The obtained material was stable on the air as proven by the CHN elemental analysis and a PXRD technique (Fig. S5). Yield: 81 mg, 70% (based on Ho). The IR spectrum for **3** with the interpretation is given in Fig. S1 and Table S1. Elem. anal. Calcd. for $Ho_1Ir_1C_{26}H_{28}N_{10}O_8$ (M_W = 965.7 g·mol^{-1}): C, 32.3%; H, 2.9%; 14.5%. Found: C, 32.2%; H, 3.0%; N, 14.6%.

Synthesis of 4 (Y–Co compound)

The Y^{III}-containing reference analogue, compound **4**, was prepared in the analogous manner as described for **1** by using 74 mg (0.24 mmol) of $YCl_3·6H_2O$ instead of $HoCl_3·6H_2O$. After a few days of crystallization in the dark, weakly yellow block crystals of **4** were collected, filtrated, washed with water and ethanol, and dried on the air. They were found to be isostructural with compounds **1**–**3** as was proven by the powder X-ray diffraction method (Fig. S5). Therefore, the analogous air-stable composition of **4**, **$\{[Y(4\text{-pyridone})_4(H_2O)_2][Co(CN)_6]\}·2H_2O$**, could be postulated which was additionally confirmed by the CHN elemental analysis. Yield: 108 mg, 60% (based on Y). Elem. anal. Calcd. for $Y_1Co_1C_{26}H_{28}N_{10}O_8$ (M_W = 756.4 g·mol^{-1}): C, 41.3%; H, 3.7%; 18.5%. Found: C, 41.1%; H, 3.8%; N, 18.6%.

Syntheses of magnetically diluted samples, 1@Y, 2@Y, and 3@Y

Three magnetically diluted samples of compounds **1**–**3** prepared with the identical starting molar percentages of Ho^{3+} and Y^{3+} (10% and 90%, respectively, in respect to the 100% amount of Ho^{3+} ions in **1**–**3**) were prepared in the analogous manner as described for their undiluted Ho–$[M^{III}(CN)_6]^{3-}$ relatives (M = Co, **1**; M = Rh, **2**; M = Ir, **3**; see above). It means that all of them were prepared in the analogous way, keeping the identical molar ratios between introduced Ho and Y centres (1:9). Thus, they are named **1@Y**, **2@Y**, and **3@Y**, even that their final metal ratios slightly differed (see below) probably due to the slightly different reactivity of the corresponding hexacyanidometallate precursors with introducing rare earth metal ions. The detailed compositions of the respective precursor solutions were as follows:

1@Y (which can be also named as **1@Y–$Ho_{0.11}Y_{0.89}$Co** according to the nomenclature used for the whole series of trimetallic **Ho_xY_{1-x}Co** compounds described below). Solution I: 9.1 mg (0.024 mmol) of $HoCl_3·6H_2O$, 66.6 mg (0.216 mmol) of $YCl_3·6H_2O$, and 230 mg (2.4 mmol) of 4-pyridone dissolved in 1 mL of distilled water. Solution II: 80 mg (0.24 mmol) of $K_3[Co(CN)_6]$ in 1 mL of distilled water.

2@Y. Solution I: 9.1 mg (0.024 mmol) of $HoCl_3·6H_2O$, 66.6 mg (0.216 mmol) of $YCl_3·6H_2O$, and 230 mg (2.4 mmol) of 4-pyridone dissolved in 0.5 mL of distilled water. Solution II: 92 mg (0.24 mmol) of $K_3[Rh(CN)_6]$ in 0.5 mL of distilled water.

3@Y. Solution I: 9.1 mg (0.024 mmol) of $HoCl_3·6H_2O$, 66.6 mg (0.216 mmol) of $YCl_3·6H_2O$, and 230 mg (2.4 mmol) of 4-pyridone dissolved in 1 mL of distilled water. Solution II: 113 mg (0.24 mmol) of $K_3[Ir(CN)_6]$ in 1 mL of distilled water.

In all these samples, **1@Y**, **2@Y**, and **3@Y**, the molar composition of the (Ho+Y) mixture used in the synthesis includes the 10% of Ho and 90% of Y. The resulting crystalline products of **1@Y**, **2@Y**, and **3@Y**, obtained in the form of yellowish block crystals, were collected after a few days of crystallization in the dark. They were filtrated, washed with water and ethanol, and dried on the air. They were stable on the air, and isostructural with compounds **1**–**3** as proved by the powder X-ray diffraction measurements (Fig. S5). These results, together with the CHN and metals (ICP-MS) elemental analyses, revealed the detailed compositions of **1@Y**, **2@Y**, and **3@Y**:

1@Y. Formula: **{[$Ho_{0.11}Y_{0.89}$(4-pyridone)$_4$(H_2O)$_2$][$Co(CN)_6$]}·2H_2O**. CHN elem. anal. Calcd. for $Ho_{0.11}Y_{0.89}Co_1$ $C_{26}H_{28}N_{10}O_8$ (M_W = 764.8 g·mol^{-1}): C, 40.8%; H, 3.7%; 18.3%. Found: C, 40.9%; H, 3.9%; N, 18.4%. Ho/Y metal ratio. Calcd. 0.124. Found (ICP-MS): 0.125(6). Yield: 113 mg, 62% (based on Co).

2@Y. Formula: **{[$Ho_{0.12}Y_{0.88}$(4-pyridone)$_4$(H_2O)$_2$][$Rh(CN)_6$]}·3H_2O**. CHN elem. anal. Calcd. for $Ho_{0.12}Y_{0.88}Rh_1$ $C_{26}H_{30}N_{10}O_9$ (M_W = 809.5 g·mol^{-1}): C, 37.7%; H, 3.6%; 16.9%. Found: C, 37.3%; H, 3.8%; N, 16.8%. Ho/Y metal ratio. Calcd. 0.136. Found (ICP-MS): 0.141(6). Note that, according to the results of CHN elemental analysis, the amount of non-coordinated water in **2@Y** was found to be higher than in other derivatives (**1@Y** and **3@Y**). The analogous effect was repeatedly detected also in the bimetallic Ho–Rh analogue, **2** (see above). Yield: 37 mg, 19% (based on Rh).

3@Y. Formula: **{[$Ho_{0.10}Y_{0.90}$(4-pyridone)$_4$(H_2O)$_2$][$Co(CN)_6$]}·2H_2O**. CHN elem. anal. Calcd. for $Ho_{0.10}Y_{0.90}Ir_1$ $C_{26}H_{28}N_{10}O_8$ (M_W = 897.3 g·mol^{-1}): C, 34.8%; H, 3.1%; 15.6%. Found: C, 34.6%; H, 3.4%; N, 15.5%. Ho/Y metal ratio. Calcd. 0.111. Found (ICP-MS): 0.112(8). Yield: 140 mg, 65% (based on Ir).

Syntheses of a series of HoYCo magnetically diluted samples, 1@Y–Ho_xY_{1-x}Co

Besides the magnetically diluted samples with the 1:9 metal ratio between Ho and Y, a series of trimetallic **HoYCo** samples (the analogues of **1** and **1@Y**) with the variable Ho-to-Y ratio, named **1@Y–Ho_xY_{1-x}Co**, was prepared. They were synthesized using the analogous procedure described above for **1** and **1@Y**. The detailed compositions of the respective precursor solutions were as follows:

1@Y–$Ho_{0.03}Y_{0.97}$Co. Solution I: 2.3 mg (0.006 mmol) of $HoCl_3·6H_2O$, 71.0 mg (0.234 mmol) of $YCl_3·6H_2O$, and 230 mg (2.4 mmol) of 4-pyridone dissolved in 1 mL of distilled water. Solution II: 80 mg (0.24 mmol) of $K_3[Co(CN)_6]$ in 1 mL of distilled water. The molar composition of the (Ho+Y) mixture used in the synthesis: 2.5% of Ho, 97.5% of Y.

1@Y–$Ho_{0.05}Y_{0.95}$Co. Solution I: 4.5 mg (0.012 mmol) of $HoCl_3·6H_2O$, 69.2 mg (0.228 mmol) of $YCl_3·6H_2O$, and 230 mg (2.4 mmol) of 4-pyridone dissolved in 1 mL of distilled water. Solution II: 80 mg (0.24 mmol) of $K_3[Co(CN)_6]$ in 1 mL of distilled water. The molar composition of the (Ho+Y) mixture used in the synthesis: 5% of Ho, 95% of Y.

1@Y–$Ho_{0.08}Y_{0.92}$Co. Solution I: 6.8 mg (0.018 mmol) of $HoCl_3·6H_2O$, 67.4 mg (0.222 mmol) of $YCl_3·6H_2O$, and 230 mg (2.4 mmol) of 4-pyridone dissolved in 1 mL of distilled water. Solution II: 80 mg (0.24 mmol) of $K_3[Co(CN)_6]$ in 1 mL of distilled water. The molar composition of the (Ho+Y) mixture used in the synthesis: 8% of Ho, 92% of Y.

1@Y–$Ho_{0.11}Y_{0.89}$Co. This sample is identical with **1@Y** which synthetic procedure was described above.

1@Y–$Ho_{0.16}Y_{0.84}$Co. Solution I: 13.7 mg (0.036 mmol) of $HoCl_3·6H_2O$, 61.9 mg (0.204 mmol) of $YCl_3·6H_2O$, and 230 mg (2.4 mmol) of 4-pyridone dissolved in 1 mL of distilled water. Solution II: 80 mg (0.24 mmol) of $K_3[Co(CN)_6]$ in 1 mL of distilled water. The molar composition of the (Ho+Y) mixture used in the synthesis: 15% of Ho, 85% of Y.

1@Y–$Ho_{0.22}Y_{0.78}$Co. Solution I: 18.2 mg (0.048 mmol) of $HoCl_3·6H_2O$, 58.3 mg (0.192 mmol) of $YCl_3·6H_2O$, and 230 mg (2.4 mmol) of 4-pyridone dissolved in 1 mL of distilled water. Solution II: 80 mg (0.24 mmol) of $K_3[Co(CN)_6]$ in 1 mL of distilled water. The molar composition of the (Ho+Y) mixture used in the synthesis: 20% of Ho, 80% of Y.

1@Y–$Ho_{0.33}Y_{0.67}$Co. Solution I: 27.3 mg (0.072 mmol) of $HoCl_3·6H_2O$, 51.0 mg (0.168 mmol) of $YCl_3·6H_2O$, and 230 mg (2.4 mmol) of 4-pyridone dissolved in 1 mL of distilled water. Solution II: 80 mg (0.24 mmol) of $K_3[Co(CN)_6]$ in 1 mL of distilled water. The molar composition of the (Ho+Y) mixture used in the synthesis: 30% of

Ho, 70% of Y.

The resulting crystalline samples of **1@Y–Ho$_x$Y$_{1–x}$Co** were gathered after a few days of crystallization in the dark, then, filtrated, washed with water and ethanol, and dried on the air overnight. They were isostructural with compounds **1**–**3** as indicated by the P-XRD studies (Fig. S6), and, similarly, they are stable on the air. The results of P-XRD measurements, along with the CHN and metals (ICP-MS) elemental analyses, were used to determine the detailed compositions of all samples within the **1@Y–Ho$_x$Y$_{1–x}$Co** family:

1@Y–Ho$_{0.03}$Y$_{0.97}$Co. Formula: **{[Ho$_{0.03}$Y$_{0.97}$(4-pyridone)$_4$(H$_2$O)$_2$][Co(CN)$_6$]}·2H$_2$O**. CHN elem. anal. Calcd. for $Ho_{0.03}Y_{0.97}Co_1C_{26}H_{28}N_{10}O_8$ (M_W = 758.7 g·mol^{-1}): C, 41.2%; H, 3.7%; 18.5%. Found: C, 41.1%; H, 3.9%; N, 18.6%. Ho/Y metal ratio. Calcd. 0.031. Found (ICP-MS): 0.030(2). Yield: 114 mg, 63% (based on Co).

1@Y–Ho$_{0.05}$Y$_{0.95}$Co. Formula: **{[Ho$_{0.05}$Y$_{0.95}$(4-pyridone)$_4$(H$_2$O)$_2$][Co(CN)$_6$]}·2H$_2$O**. CHN elem. anal. Calcd. for $Ho_{0.05}Y_{0.95}Co_1C_{26}H_{28}N_{10}O_8$ (M_W = 760.2 g·mol^{-1}): C, 41.1%; H, 3.7%; 18.4%. Found: C, 41.0%; H, 3.9%; N, 18.6%. Ho/Y metal ratio. Calcd. 0.053. Found (ICP-MS): 0.057(4). Yield: 113 mg, 62% (based on Co).

1@Y–Ho$_{0.08}$Y$_{0.92}$Co. Formula: **{[Ho$_{0.08}$Y$_{0.92}$(4-pyridone)$_4$(H$_2$O)$_2$][Co(CN)$_6$]}·2H$_2$O**. CHN elem. anal. Calcd. for $Ho_{0.08}Y_{0.92}Co_1C_{26}H_{28}N_{10}O_8$ (M_W = 762.5 g·mol^{-1}): C, 41.0%; H, 3.7%; 18.4%. Found: C, 40.9%; H, 3.9%; N, 18.6%. Ho/Y metal ratio. Calcd. 0.087. Found (ICP-MS): 0.090(4). Yield: 102 mg, 56% (based on Co).

1@Y–Ho$_{0.16}$Y$_{0.84}$Co. Formula: **{[Ho$_{0.16}$Y$_{0.84}$(4-pyridone)$_4$(H$_2$O)$_2$][Co(CN)$_6$]}·2H$_2$O**. CHN elem. anal. Calcd. for $Ho_{0.16}Y_{0.84}Co_1C_{26}H_{28}N_{10}O_8$ (M_W = 768.6 g·mol^{-1}): C, 40.6%; H, 3.6%; 18.2%. Found: C, 40.5%; H, 3.8%; N, 18.4%. Ho/Y metal ratio. Calcd. 0.191. Found (ICP-MS): 0.198(9). Yield: 124 mg, 67% (based on Co).

1@Y–Ho$_{0.22}$Y$_{0.78}$Co. Formula: **{[Ho$_{0.22}$Y$_{0.78}$(4-pyridone)$_4$(H$_2$O)$_2$][Co(CN)$_6$]}·2H$_2$O**. CHN elem. anal. Calcd. for $Ho_{0.22}Y_{0.78}Co_1C_{26}H_{28}N_{10}O_8$ (M_W = 773.1 g·mol^{-1}): C, 40.4%; H, 3.6%; 18.1%. Found: C, 40.3%; H, 3.8%; N, 18.4%. Ho/Y metal ratio. Calcd. 0.282. Found (ICP-MS): 0.279(8). Yield: 109 mg, 59% (based on Co).

1@Y–Ho$_{0.33}$Y$_{0.67}$Co. Formula: **{[Ho$_{0.33}$Y$_{0.67}$(4-pyridone)$_4$(H$_2$O)$_2$][Co(CN)$_6$]}·2H$_2$O**. CHN elem. anal. Calcd. for $Ho_{0.33}Y_{0.67}Co_1C_{26}H_{28}N_{10}O_8$ (M_W = 781.5 g·mol^{-1}): C, 40.0%; H, 3.6%; 17.9%. Found: C, 39.9%; H, 3.8%; N, 18.4%. Ho/Y metal ratio. Calcd. 0.492. Found (ICP-MS): 0.482(17). Yield: 112 mg, 60% (based on Co).

Crystallography

Single-crystal X-ray diffraction (SC-XRD) analyses for **1** and **2** were performed on a Rigaku R-AXIS RAPID diffractometer equipped with the imaging plate type detector and graphite monochromated MoKα radiation, while the single crystal of **3** was measured on Bruker D8 Quest Eco Photon50 CMOS diffractometer equipped with graphite monochromated Mo Kα radiation (Table S2). For the SC-XRD studies, the selected single crystals of **1–3** were covered by Apiezon® N grease and mounted onto the Micro Mounts™ holder. The measurements for **1** and **2** were carried out at 90(2) K, and after collecting all the diffraction frames, the crystal structures of **1** and **2** were solved using a direct method within the SHELXS-97 program integrated with the *Crystal Structure* software.[S3–S4] The SC-XRD measurement for **3** was carried out at 100(2) K, the data reduction and cell refinement were performed using SAINT and SADABS programs, and the crystal structure of **3** was solved by an intrinsic phasing method using a SHELXT-2014/5.[S4] All crystal structures were refined following a weighted full-matrix least-squares method on F^2 on SHELX-2018/3 within the *WinGX v2014/1* integrated system.[S5] All non-hydrogen atoms were refined anisotropically. The hydrogen atoms were found from the electron density map and refined using a riding model. A few restraints (ISOR and DELU) were applied for non-hydrogen atoms to ensure the convergence of the refinement procedure and maintain the proper coordination geometry. The crystallographic data were deposited in the CCDC database. Deposition numbers are 1983881, 1983882, and 1983883 for **1**, **2**, and **3**, respectively. The detailed parameters of crystal data and structure refinement are presented in Table S2 while the representative structural parameters of the obtained models are shown in Table S3. The structural figures were prepared by using the *Mercury 3.10.3* software. Powder X-ray diffraction (P-XRD) patterns of all samples were collected on a Rigaku Ultima-IV diffractometer equipped with CuKα radiation (λ = 1.5418 Å).

(S3) G. M. Sheldrick, *SHELXS-97, Program for crystal structure solution*, University of Göttingen, Göttingen, Germany, 1997.

(S4) G. M. Sheldrick, *Acta Cryst*., 2015, **C71**, 3–8.

(S5) L. J. Farrugia, *J. Appl. Cryst*., 2012, **45**, 849–854.

Physical techniques

All measurements of physical properties were performed on the polycrystalline solid state samples of the investigated compounds which phase purity was checked by using the P-XRD method. Infrared (IR) absorption spectra were collected using a JASCO FTIR-4100 spectrometer on the pellet made of the powder sample of the compound mixed with potassium bromide. The thermogravimetric (TG) analyses were performed on a Rigaku Thermo Plus TG8120 apparatus under nitrogen atmosphere, in the 20–375 °C range, with a heating rate of 1 $°C \cdot min^{-1}$. UV-Vis-NIR absorption spectra were measured using a reflectance mode of a JASCO V-670 spectrophotometer on the powder samples mixed with barium sulfate. Photoluminescence studies were performed using a Horiba JobinYvon Fluorolog®-3 (FL3-211) spectrofluorimeter (model TKN-7) with a Xe lamp (450 W) as the excitation source, and the R928P Hamamatsu detector working in a photo-counting mode. The emission and excitation data collection was executed using the FluorEssence® software package. The temperature control in photoluminescence studies was achieved by using a microscopy cryostat (Oxford Instruments) with liquid helium as a cryogen. For the luminescent experiments, the powder samples of **1**–**3** were mixed with paraffin oil and sandwiched between two quartz plates. Magnetic properties were measured using a Quantum Design MPMS XL magnetometer on the powder samples were prepared in a capsule-type holder where the well grinded polycrystalline samples of **1**–**3** and their magnetically diluted analogs were covered with paraffin oil and cotton wool. Magnetic data were corrected for the diamagnetic contributions from the sample and the holder.

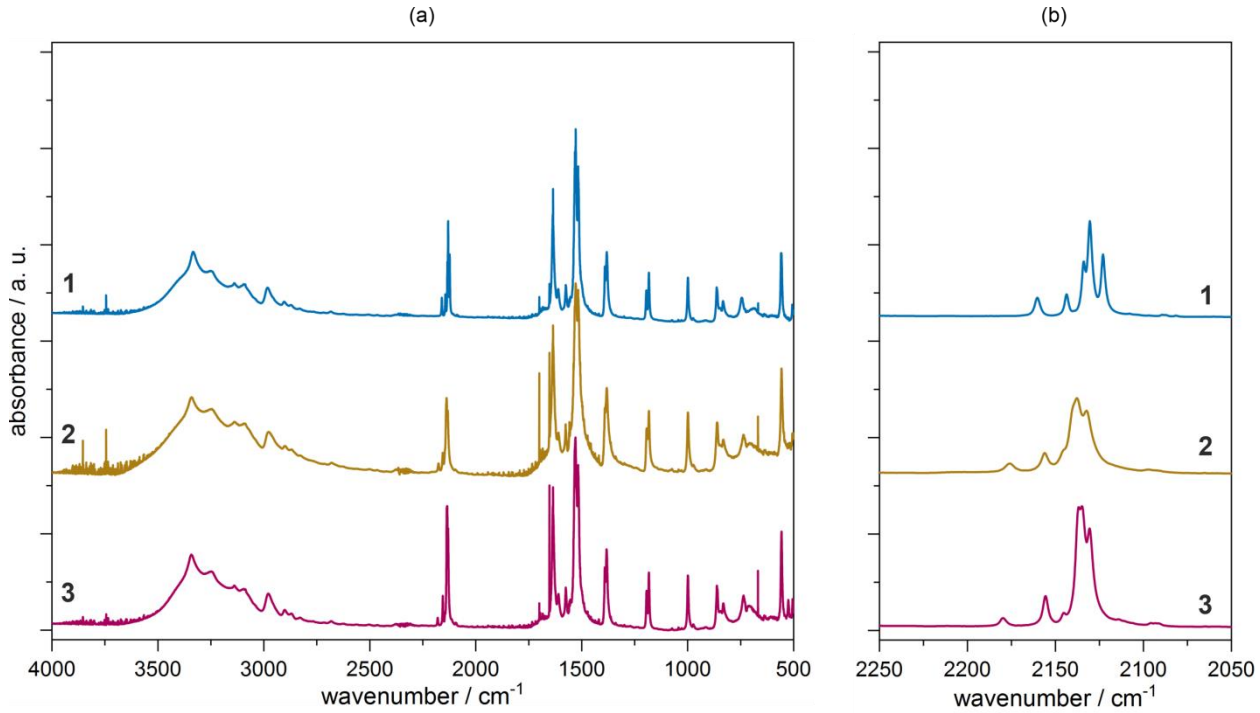

Fig. S1 Infrared (IR) absorption spectra of **1**–**3** measured in the 4000–500 cm^{-1} range (*a*), together with the enlargement of the 2250–2050 cm^{-1} region related to the stretching modes of cyanido ligands (*b*). The exact positions of the main IR absorption peaks together with their assignment are gathered in Table S1.

Table S1 The energy positions and the assignment for the main IR absorption peaks of **1**–**3** (see Fig. S1).[S1,S6]

energy position / cm^{-1} and description of the relative intensity (vs = very strong, s = strong, m = medium, w = weak, vw = very weak)			**assignment**
1	**2**	**3**	
3334s	3341s	3343s	N-H stretching modes, O-H stretching modes, H-bonding modes
3250s	3243s	3247s	
3141s	3142s	3141s	
3089s	3087s	3088s	
2982s	2976s	2980s	
2901w	2903w	2903w	
2874w	2870w	2870w	
2832w	2829w	2830w	
2160vs	2176vs	2180vs	stretching modes of cyanido ligand
2144vs	2156vs	2156vs	
2134vs	2146vs	2145vs	
2130vs	2138vs	2136vs	
2123vs	2133vs	2131vs	
1635vs	1635vs	1635vs	stretching modes of 4-pyridone ring
1610m	1610m	1610m	
1575m	1576m	1576m	C=O stretching modes
1530vs	1529vs	1530vs	stretching modes of 4-pyridone ring
1517vs	1517vs	1517vs	
1391vs	1391vs	1391vs	vibrational modes of 4-pyridone ring
1382vs	1382vs	1383vs	
1196vs	1194vs	1194vs	in-plane C-H deformation
1183vs	1183vs	1183vs	
999vs	999vs	999vs	
863vs	861vs	862vs	out-of-plane C-H deformation
846s	845s	845s	
833s	833s	832s	
744s	736s	736s	

(S6) A. R. Katritzky and A. R. Jones, *J. Chem. Soc.*, 1960, 2947–2953.

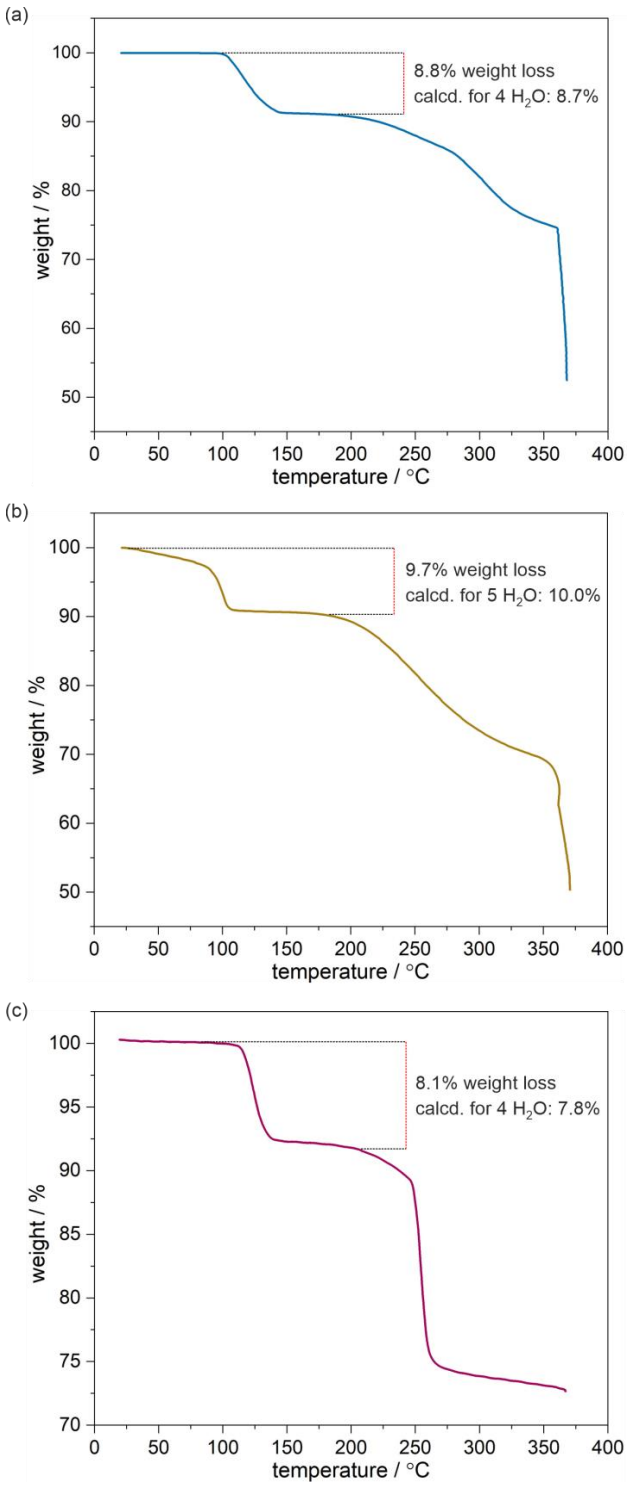

Fig. S2 Thermogravimetric curves of **1** (*a*), **2** (*b*), and **3** (*c*) measured under the nitrogen atmosphere.

Comment to Fig. S2:

Upon heating from room temperature to 100 ºC, the sample weights of **1** and **3** are almost stable while compound **2** exhibits a gradual, however small, decrease of the sample mass. It can be ascribed to the removal of very weakly bonded water molecules which generally exist in **2** in the larger amount than in **1** and **3** (five water molecules per one Ho in **2** while only four water molecules per one Ho in **1** and **3**, according to the results of CHN elemental analysis). Further heating results in an abrupt weight loss attributable to the release of water of crystallization as well as the water coordinated to Ho^{3+} ions. Up to 150 ºC, the TG curves of **1**–**3** reach the plateau stages which correspond to the dehydrated states. The related weight losses are in good agreement with the calculated ones (Fig. S2). Heating to temperatures above ca. 200 ºC leads to the dramatic decrease of the sample masses which is presumably connected with the removal of the part of cyanido as well as organic ligands, and the resulting decomposition of the compounds.

Table S2 Details of crystal data and structure refinement for **1**–**3**.

compound	**1**	**2**	**3**
CCDC number	1983881	1983882	1983883
formula	832.44	876.42	965.71
formula weight / $g \cdot mol^{-1}$	$Ho_1Co_1C_{26}H_{28}N_{10}O_8$	$Ho_1Rh_1C_{26}H_{28}N_{10}O_8$	$Ho_1Ir_1C_{26}H_{28}N_{10}O_8$
T / K	90(2)	90(2)	100(2)
λ / Å	0.71075(Mo Kα)	0.71075(Mo Kα)	0.71073(Mo Kα)
crystal system	orthorhombic	orthorhombic	orthorhombic
space group	*Cmcm*	*Cmcm*	*Cmcm*
a / Å	14.7754(11)	14.8236(6)	14.8720(3)
b / Å	14.9336(11)	15.1198(8)	15.2339(3)
c / Å	14.0276(8)	14.0660(7)	14.1487(3)
α, β, γ / deg	90	90	90
V / $Å^3$	3095.2(4)	3152.6(3)	3205.51(11)
Z	4	4	4
ρ_{calc} / $g \cdot cm^{-3}$	1.786	1.847	2.001
μ / cm^{-1}	3.138	3.078	6.66
F(000)	1648	1720	1848
crystal type	light yellow block	light yellow block	light yellow block
crystal size / mm × mm × mm	0.42× 0.09 × 0.07	0.21× 0.11 × 0.09	0.13× 0.11 × 0.06
θ range /deg	3.091–27.479	3.059–27.461	2.395–27.095
limiting indices	-19 < h < 19 -19 < k < 19 -18 < l < 18	-17 < h < 19 -19 < k < 19 -18 < l < 18	-16 < h < 19 -19 < k < 19 -18 < l < 18
collected reflections	14806	14551	11862
unique reflections	1920	1947	1918
R_{int}	0.031	0.078	0.026
completeness / %	99.7	99.7	99.9
data/parameters/restraints	1920/195/26	1947/195/15	1918/195/7
GOF on F^2	1.217	1.175	1.094
final R indices [$I \geq 2\sigma(I)$]	R_1 = 0.0288, wR_2 = 0.0578	R_1 = 0.0574, wR_2 = 0.0935	R_1 = 0.0187, wR_2 = 0.0448
final R indices (all data)	R_1 = 0.0295, wR_2 = 0.058	R_1 = 0.0682, wR_2 = 0.0969	R_1 = 0.0225, wR_2 = 0.0462
largest diff. (peak/hole) / $e \cdot Å^{-3}$	1.971/-2.103	2.513/-3.974	1.813/-1.585

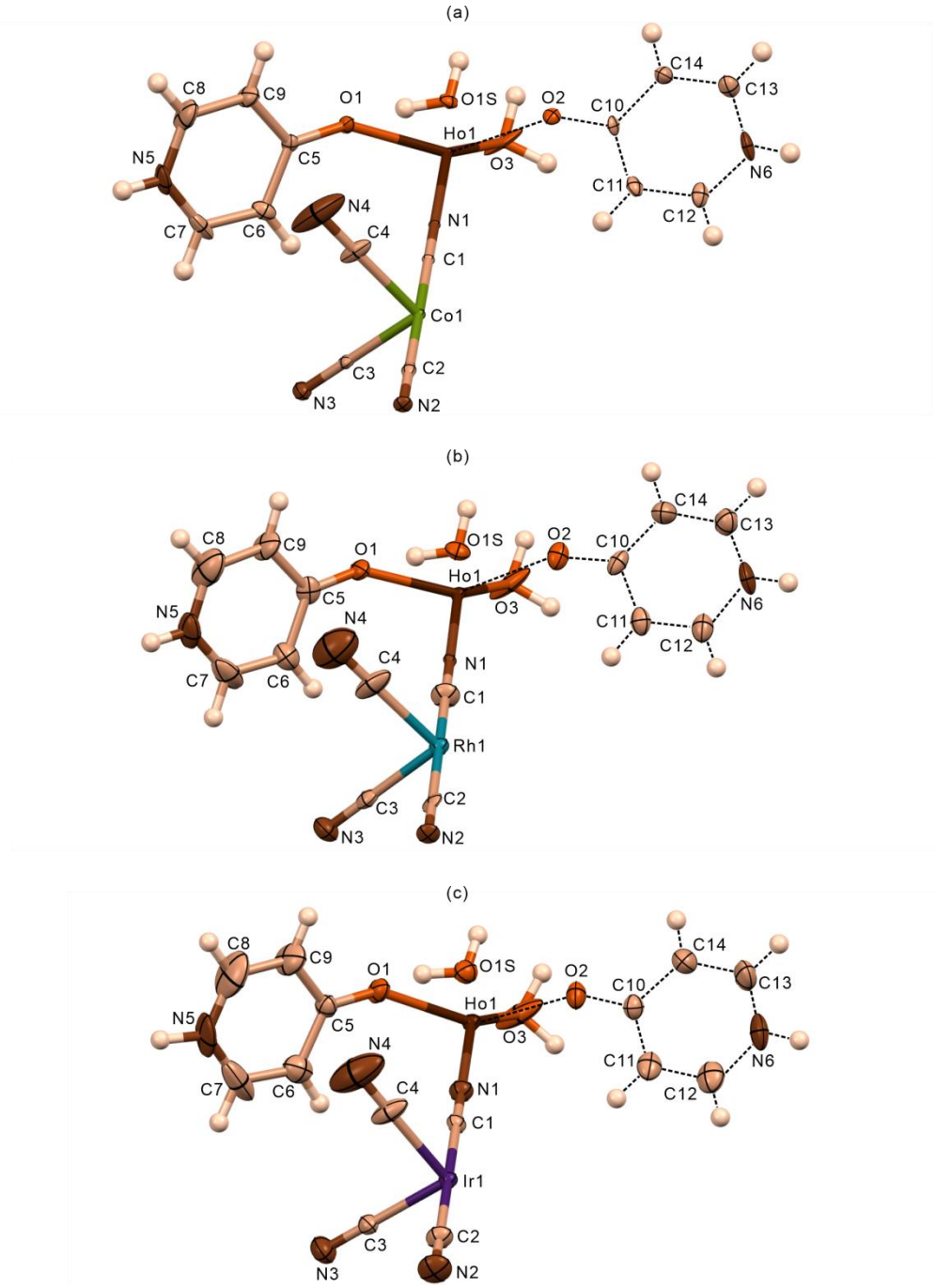

Fig. S3 Asymmetric units of **1** (*a*), **2** (*b*), and **3** (*c*). Thermal ellipsoids of non-hydrogen atoms are presented at the 50% probability level. Hydrogen atoms were presented as fixed-sized spheres with the 0.2 Å radius. The dashed lines represent bonds between the atoms refined using the PART command. The related bond lengths and angles are collected in Table S3**.**

Table S3 Detailed structure parameters of **1**–**3**.

bond / angle	**1** (M1 = Co)	**2** (M1 = Rh)	**3** (M1 = Ir)
Ho1–O2	**2.231(4) Å**	**2.233(9) Å**	**2.235(4) Å**
Ho1–O1	**2.272(4) Å**	**2.276(9) Å**	**2.278(4) Å**
Ho1–O3	**2.388(4) Å**	**2.372(7) Å**	**2.385(3) Å**
Ho1–N1	**2.460(5) Å**	**2.434(10) Å**	**2.452(5) Å**
weighted average Ho1–O/N	**2.320 Å**	**2.314 Å**	**2.321 Å**
weighted average Ho1–O1/O3/N1 (equatorial plane of PBY-7 polyhedron)	**2.356 Å**	**2.346 Å**	**2.356 Å**
M1–C1	1.867(6) Å	1.877(15) Å	2.011(6) Å
M1–C2	1.902(7) Å	2.057(15) Å	2.045(6) Å
M1–C3	1.902(5) Å	2.003(10) Å	2.030(4) Å
M1–C4	1.899(5) Å	1.992(11) Å	2.029(5) Å
C1–N1	1.182(8) Å	1.290(18) Å	1.163(8) Å
C2–N2	1.152(9) Å	1.134(18) Å	1.121(8) Å
C3–N3	1.148(6) Å	1.147(13) Å	1.141(6) Å
C4–N4	1.134(8) Å	1.142(16) Å	1.126(8) Å
O1–C5	1.276(7) Å	1.271(16) Å	1.265(8) Å
O2–C10	1.291(8) Å	1.301(16) Å	1.284(8) Å
Ho1–M1 (intramolecular)	5.509 Å	5.602 Å	5.626 Å
Ho1–Ho1 (closest distance)	7.185 Å	7.239 Å	7.272 Å
O1–Ho1–O3	73.57°	73.78°	73.98°
O3–Ho1–O3	71.34°	70.46°	70.72°
O1–Ho1–N1	73.02°	73.35°	73.08°
O2–Ho1–O1	**89.13°/94.56°** (average deviation from 90° is **2.72°**)	**88.78°/94.17°** (average deviation from 90° is **2.69°**)	**89.31°/94.06°** (average deviation from 90° is **2.37°**)
O2–Ho1–O3	74.26°/95.30°	74.96°/96.47°	74.08°/96.32°
O2–Ho1–N1	96.32°	95.15°	95.78°
O2–Ho1–O2 (axial)	167.36°	169.70°	168.44°
Ho1–N1–C1	180°	180°	180°
M1–C1–N1	180°	180°	180°
C1–M1–C3	90.30(13)°	90.4(3)°	90.61(12)°
C1–M1–C4	89.55(15)°	89.4(3)°	89.48(13)°
C2–M1–C3	89.70(13)°	89.6(3)°	89.39(12)°
C2–M1–C4	90.45(15)°	90.6(3)°	90.52(13)°
C3–M1–C4	90.002(2)°	90.004(5)°	90.005(2)°

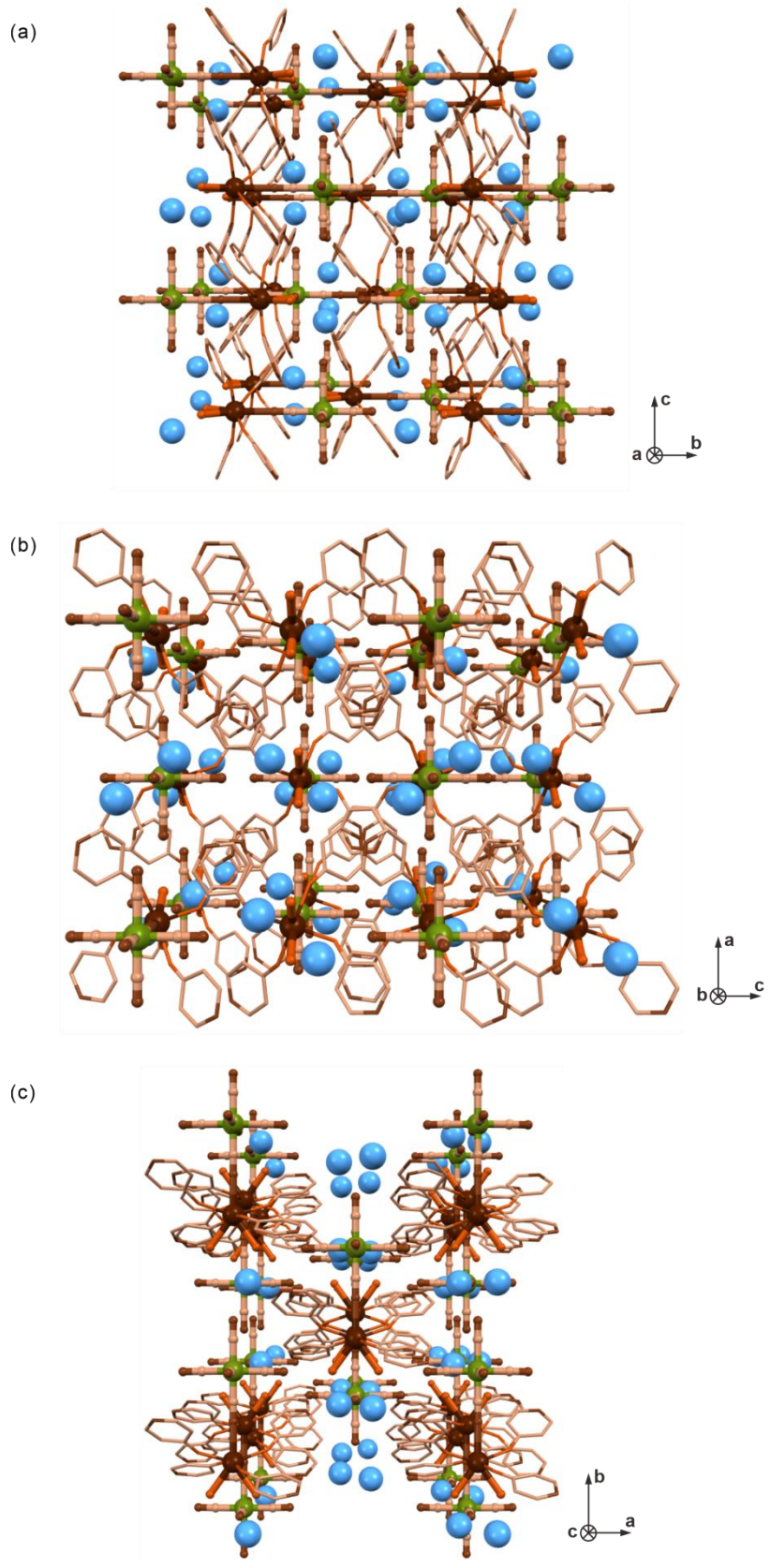

Fig. S4 Representative views of the supramolecular network of **1** along the crystallographic *a* axis (*a*), *b* axis (*b*), and *c* axis (*c*). The supramolecular network is assembled from cyanido-bridged dinuclear {$Ho^{III}Co^{III}$} molecules (green balls for 3d metal centres, brown balls and sticks for other atoms) and water of crystallization (blue enlarged balls). The hydrogen atoms are omitted for clarity. Colour settings of the atoms within the dinuclear molecules are identical to those presented for the view of the asymmetric unit (Figure S3a). The identical supramolecular frameworks are present in the isostructural compounds **2** and **3**.

Table S4 Results of Continuous Shape Measure (CSM) analysis for seven-coordinated $[Ho^{III}(4\text{-pyridone})_4(H_2O)_2(NC)]^{2+}$ complexes in the crystal structures of **1–3**.[S7–S8]

Compound	CSM parameters*							Determined geometry
	HP-7	HPY-7	PBPY-7	COC-7	CTPR-7	JPBPY-7	JETPY-7	
1	32.871	24.744	**1.380**	6.151	4.588	4.054	21.352	PBPY-7
2	33.077	24.749	**1.314**	5.746	4.152	4.110	21.264	PBPY-7
3	32.667	24.600	**1.415**	5.893	4.286	4.135	21.129	PBPY-7

*CSM parameters:

CSM HP-7 – the parameter related to the heptagon geometry (D_{7h} symmetry)

CSM HPY-7 – the parameter related to the hexagonal pyramid geometry (C_{6v} symmetry)

CSM PBPY-7 – the parameter related to the pentagonal bipyramid D5h geometry (D_{5h} symmetry)

CSM COC-7 – the parameter related to the capped octahedron geometry (C_{3v} symmetry)

CSM CTPR-7 – the parameter related to the capped trigonal prism geometry (C_{2v} symmetry)

CSM JPBPY-7 – the parameter related to the Johnson pentagonal bipyramid (J13) geometry (D_{5h} symmetry)

CSM JETPY-7 – the parameter related to the Johnson elongated triangular pyramid (J7) geometry (C_{3v} symmetry)

The value of CSM = 0 is ascribed to the ideal geometry. The increase of the CSM parameter above 0 represents the increasing distortion from the ideal polyhedron.

(S7) M. Llunell, D. Casanova, J. Cirera, J. Bofill, P. Alemany, S. Alvarez, M. Pinsky and D. Avnir, *SHAPE v. 2.1. Program for the Calculation of Continuous Shape Measures of Polygonal and Polyhedral Molecular Fragments*, University of Barcelona: Barcelona, Spain, 2013.

(S8) D. Casanova, J. Cirera, M. Llunell, P. Alemany, D. Avnir and S. Alvarez, *J. Am. Chem. Soc*., 2004, **126**, 1755–1763.

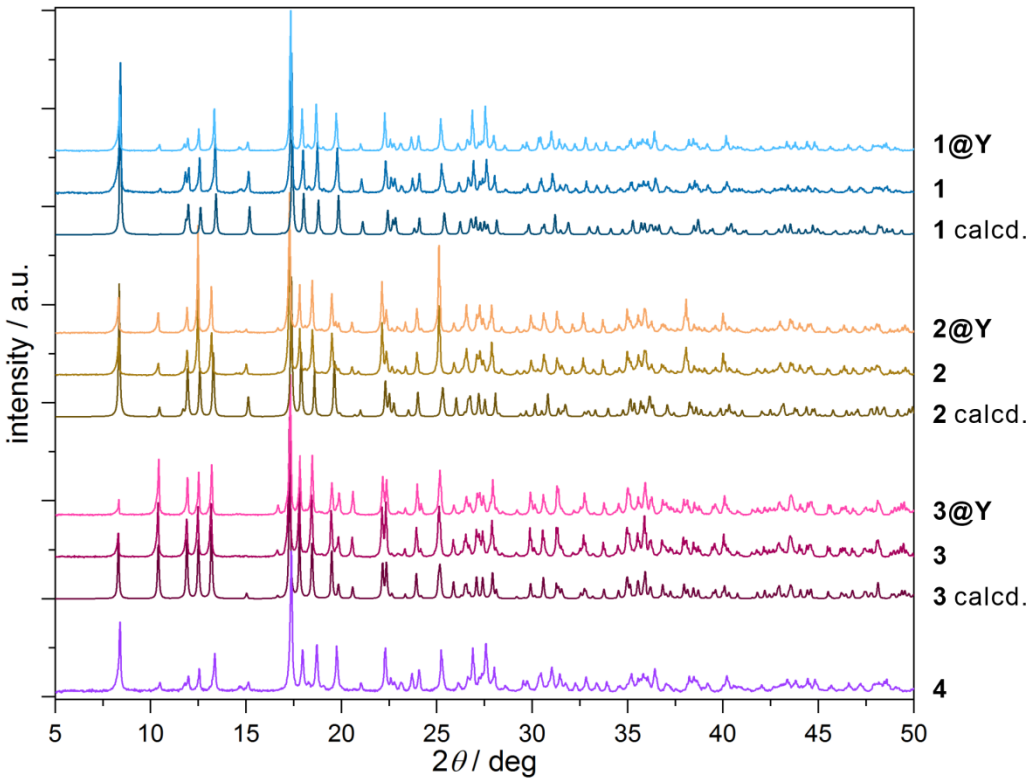

Fig. S5 The experimental P-XRD patterns of **1**–**3**, their magnetically diluted samples of **1@Y**–**3@Y**, and **4**, compared with the P-XRD patterns of **1**–**3** calculated from the structural models obtained by the SC-XRD method.

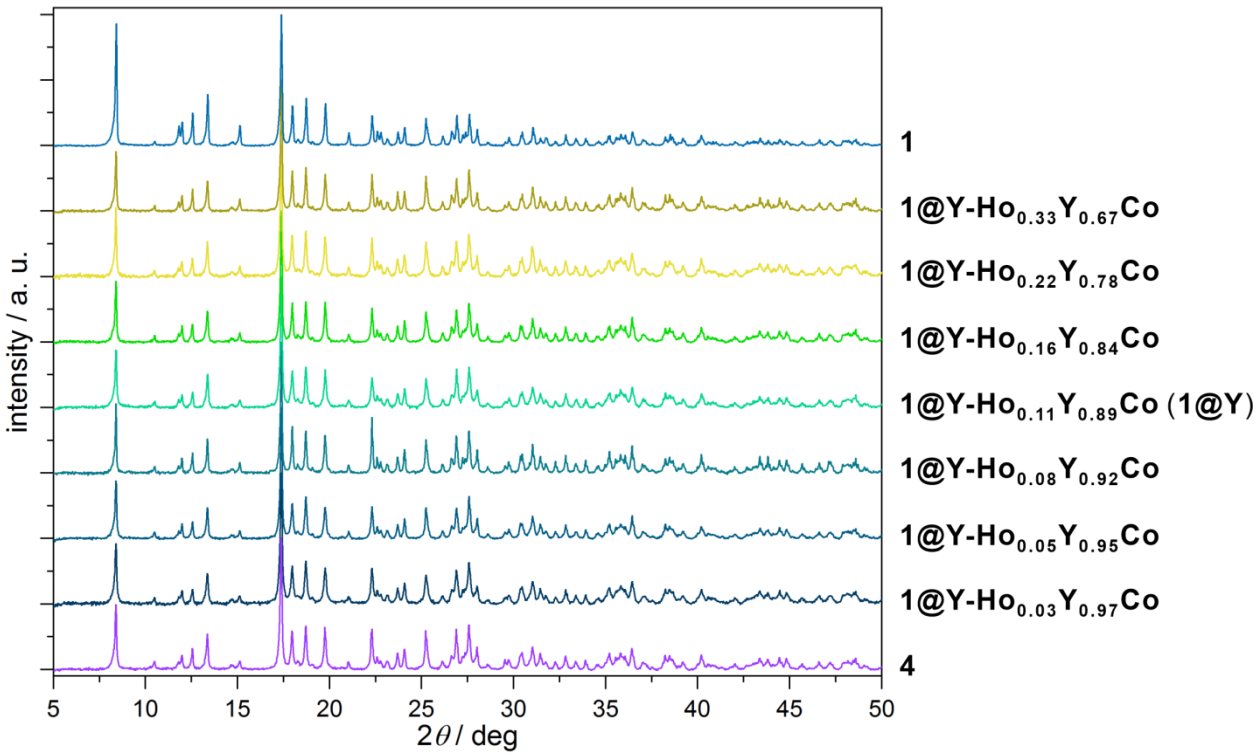

Fig. S6 The experimental P-XRD patterns of the series of HoYCo magnetically diluted samples, **1@Y–$Ho_xY_{1-x}Co$** with the variable Ho/Y molar ratio, compared with the P-XRD patterns of **1** (bimetallic Ho–Co analogue) and **4** (bimetallic Y–Co analogue, see Experimental details).

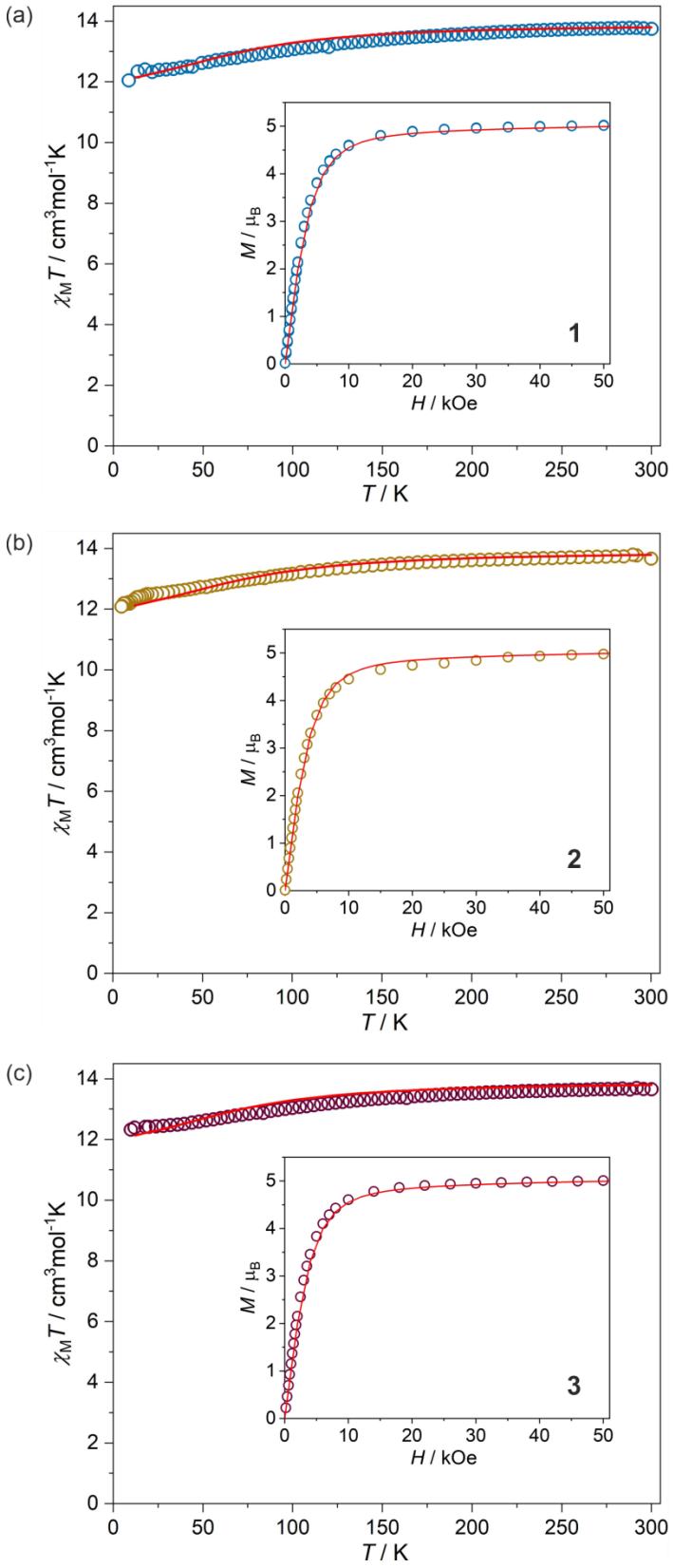

Fig. S7 Direct–current (*dc*) magnetic characteristics of **1** (*a*), **2** (*b*), and **3** (*c*): temperature dependences of the $\chi_M T$ product measured in the 2–300 K range under $H_{dc} = 1000$ Oe, and field dependences of the molar magnetization, $M(H)$, at $T = 2$ K (the insets). Coloured circles represent the experimental points while solid red lines show the curves for powder samples simulated from the results of the *ab initio* calculations (using the models employing the large basis sets and taking into account water of crystallization –**1L-W**, **2L-W** and **3L-W** models for **1**, **2**, and **3**, respectively; Table S8).

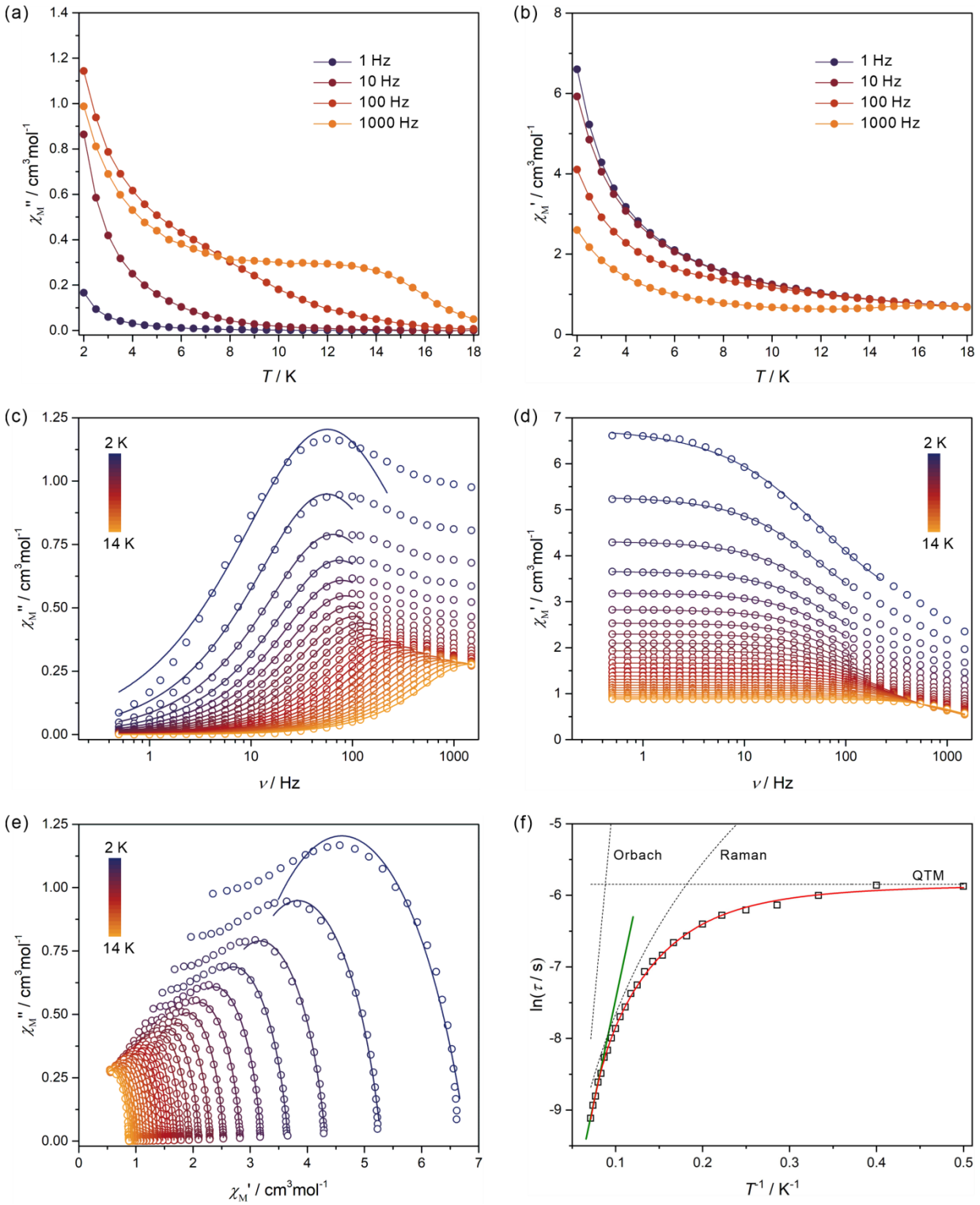

Fig. S8 Complete temperature-variable alternate-current (*ac*) magnetic susceptibility characteristics of **1** under H_{ac} = 3 Oe, H_{dc} = 0 Oe: the temperature dependence of the out-of-phase molar susceptibility, χ_M", at indicated frequencies from the 1–1000 Hz range (*a*), the temperature dependence of the in-phase molar susceptibility, χ_M', at indicated frequencies from the 1–1000 Hz range (*b*), the frequency dependence of χ_M" at indicated temperatures from the 2–14 K range (*c*), the frequency dependence of the χ_M' at indicated temperatures from the 2–14 K range (*d*), the related Argand plots (*e*), and the temperature dependence of the relaxation time, τ (*f*). Solid lines in (*a*) and (*b*) serve as a guide for the eye. Experimental points in (*c*), (*d*), and (*e*) are shown as empty circles while solid curves represent the best fits using the generalized Debye model for a single relaxation. The solid red line in (*f*) shows the best fit of the *T*-dependence of the relaxation times taking into account the quantum tunnelling of magnetization (QTM), Raman, and Orbach processes, in the 2–14 K range (each contribution is additionally depicted by the dashed lines). The green solid line in (*f*) indicates the linear fitting of the high-temperature data points in the 12.5–14 K range (see Table 1).

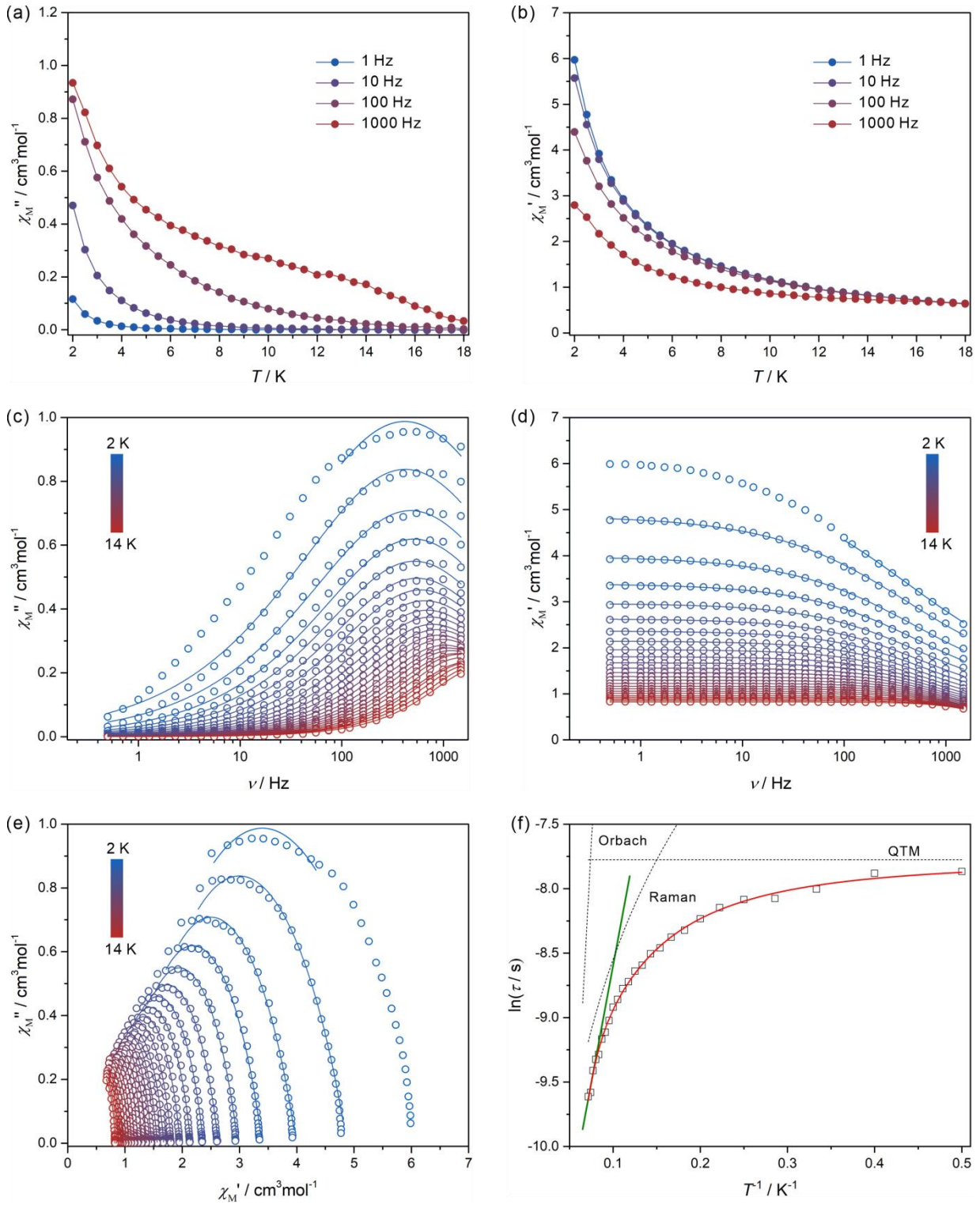

Fig. S9 Complete temperature-variable alternate-current (*ac*) magnetic susceptibility characteristics of **2** under H_{ac} = 3 Oe, H_{dc} = 0 Oe: the temperature dependence of the out-of-phase molar susceptibility, χ_M", at indicated frequencies from the 1–1000 Hz range (*a*), the temperature dependence of the in-phase molar susceptibility, χ_M', at indicated frequencies from the 1–1000 Hz range (*b*), the frequency dependence of χ_M" at indicated temperatures from the 2–14 K range (*c*), the frequency dependence of the χ_M' at indicated temperatures from the 2–14 K range (*d*), the related Argand plots (*e*), and the temperature dependence of the relaxation time, τ (*f*). Solid lines in (*a*) and (*b*) serve as a guide for the eye. Experimental points in (*c*), (*d*), and (*e*) are shown as empty circles while solid curves represent the best fits using the generalized Debye model for a single relaxation. The solid red line in (*f*) shows the best fit of the *T*-dependence of the relaxation times taking into account the quantum tunnelling of magnetization (QTM), Raman, and Orbach processes, in the 2–14 K range (each contribution is additionally depicted by the dashed lines). The green solid line in (*f*) indicates the linear fitting of the high-temperature data points in the 12.5–14 K range (see Table 1).

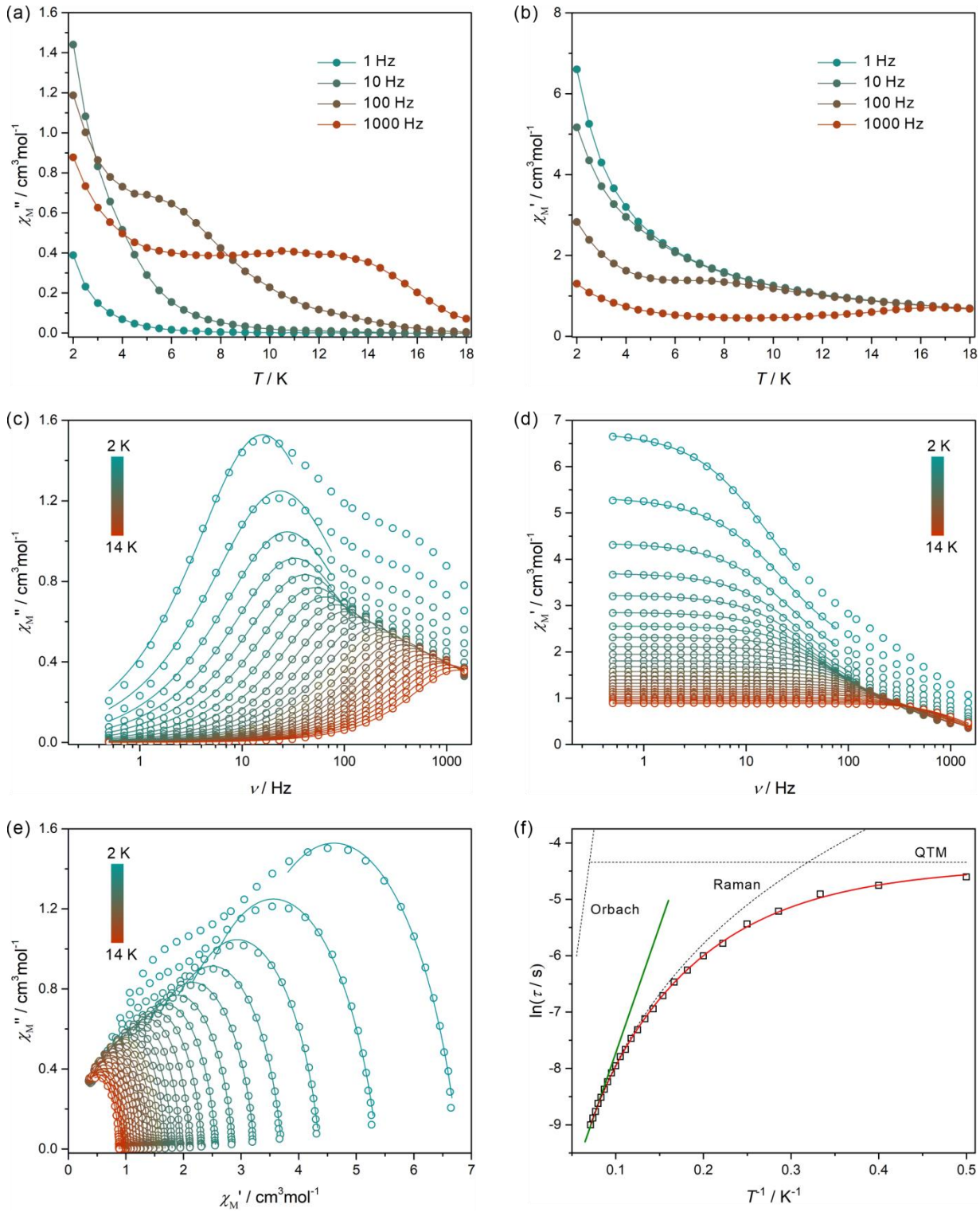

Fig. S10 Complete temperature-variable alternate-current (*ac*) magnetic susceptibility characteristics of **3** under H_{ac} = 3 Oe, H_{dc} = 0 Oe: the temperature dependence of the out-of-phase molar susceptibility, χ_M", at indicated frequencies from the 1–1000 Hz range (*a*), the temperature dependence of the in-phase molar susceptibility, χ_M', at indicated frequencies from the 1–1000 Hz range (*b*), the frequency dependence of χ_M" at indicated temperatures from the 2–14 K range (*c*), the frequency dependence of the χ_M' at indicated temperatures from the 2–14 K range (*d*), the related Argand plots (*e*), and the temperature dependence of the relaxation time, τ (*f*). Solid lines in (*a*) and (*b*) serve as a guide for the eye. Experimental points in (*c*), (*d*), and (*e*) are shown as empty circles while solid curves represent the best fits using the generalized Debye model for a single relaxation. The solid red line in (*f*) shows the best fit of the *T*-dependence of the relaxation times taking into account the quantum tunnelling of magnetization (QTM), Raman, and Orbach processes, in the 2–14 K range (each contribution is additionally depicted by the dashed lines). The green solid line in (*f*) indicates the linear fitting of the high-temperature data points in the 12.5–14 K range (see Table 1).

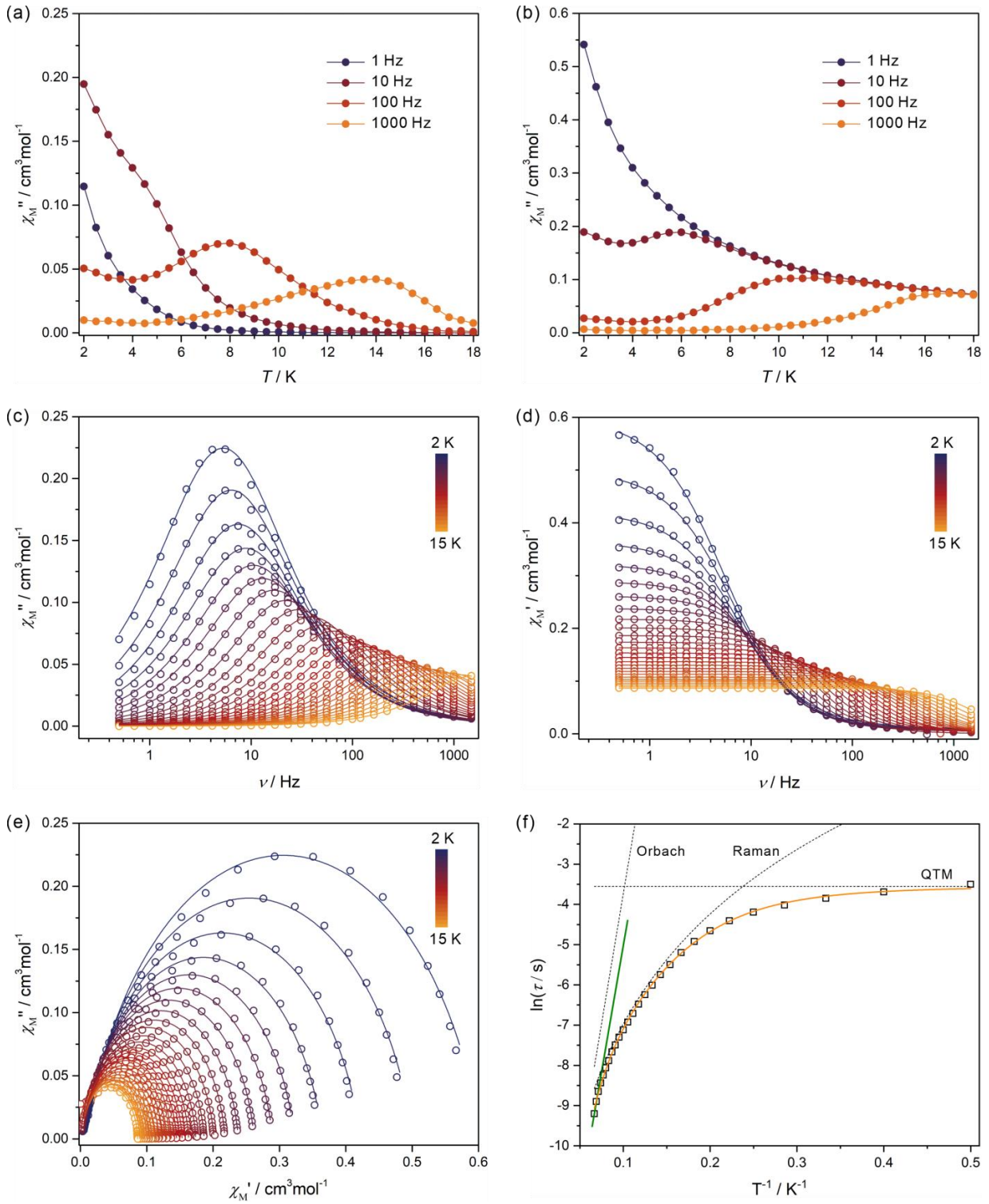

Fig. S11 Complete *T*-variable alternate-current (*ac*) magnetic susceptibility characteristics of **1@Y** under H_{ac} = 3 Oe, H_{dc} = 0 Oe: the *T*-dependence of the out-of-phase molar susceptibility, χ_M", at indicated frequencies from the 1–1000 Hz range (*a*), the *T*-dependence of the in-phase molar susceptibility, χ_M', at indicated frequencies from the 1–1000 Hz range (*b*), the frequency dependence of χ_M" at indicated temperatures from the 2–15 K range (*c*), the analogous frequency dependence of the χ_M' (*d*), the related Argand plots (*e*), and the *T*-dependence of the relaxation time, τ (*f*). Solid lines in (*a*) and (*b*) serve as a guide for the eye. Experimental points in (*c*), (*d*), and (*e*) are shown as empty circles while solid curves represent the best fits using the generalized Debye model. The solid red line in (*f*) shows the best fit of the *T*-dependence of the relaxation times taking into account quantum tunnelling of magnetization (QTM), Raman, and Orbach processes, in the 2–15 K range. This best-fit was obtained by the simultaneous fit of $\ln(\tau) = f(T^{-1})$ curves for H_{dc} = 0 Oe and the optimal *dc* field of 150 Oe, with the fixed ΔE barrier of Orbach process (see Fig. S14, S15, S20, and Table S5). Each contribution to the overall relaxation is depicted by a dashed line. The green solid line in (*f*) indicates the linear fitting of the high-temperature data points in the 14–15 K range (see Table 1).

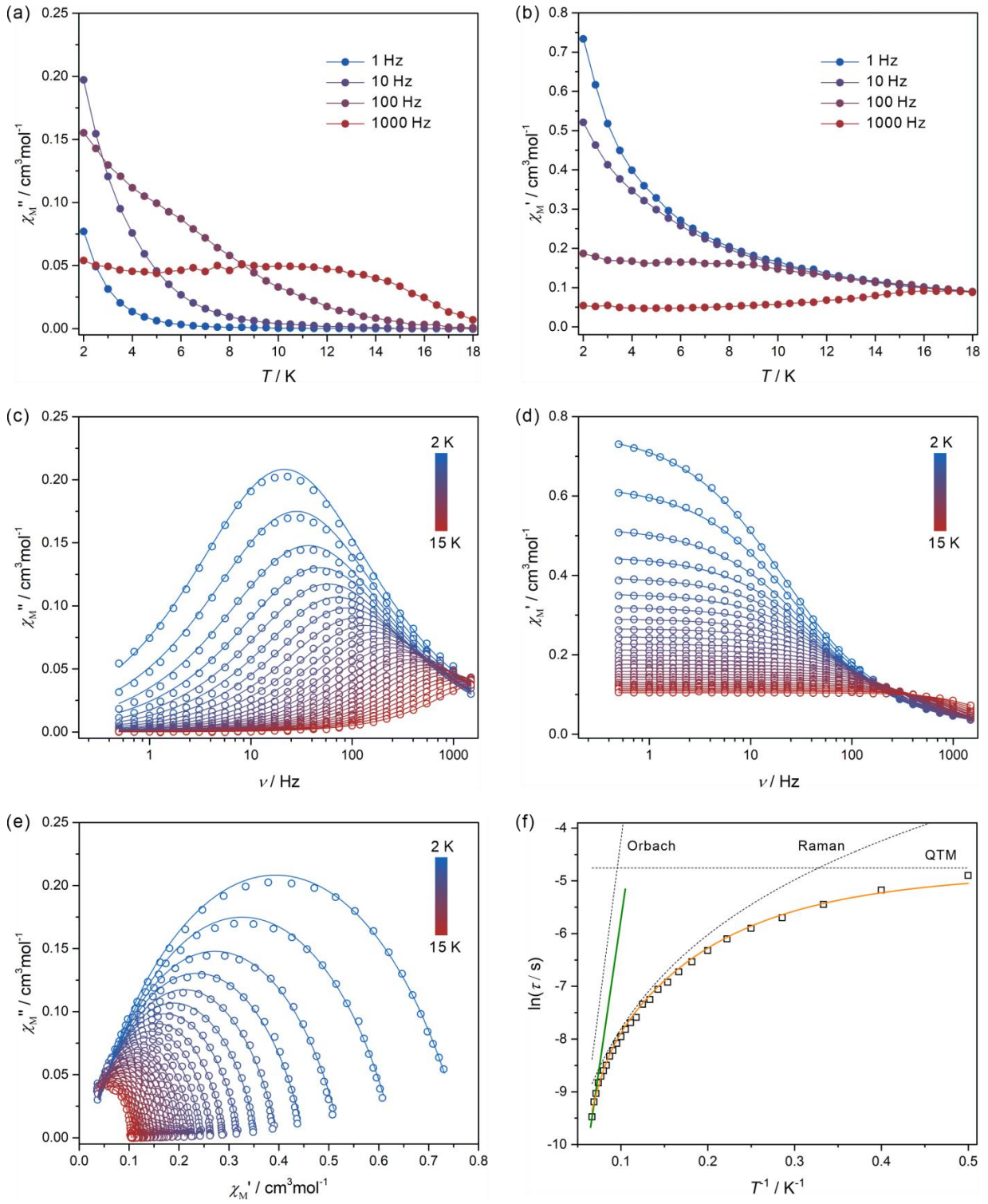

Fig. S12 Complete *T*-variable alternate-current (*ac*) magnetic susceptibility characteristics of **2@Y** under H_{ac} = 3 Oe, H_{dc} = 0 Oe: the *T*-dependence of the out-of-phase molar susceptibility, χ_M", at indicated frequencies from the 1–1000 Hz range (*a*), the *T*-dependence of the in-phase molar susceptibility, χ_M', at indicated frequencies from the 1–1000 Hz range (*b*), the frequency dependence of χ_M" at indicated temperatures from the 2–15 K range (*c*), the analogous frequency dependence of the χ_M' (*d*), the related Argand plots (*e*), and the *T*-dependence of the relaxation time, τ (*f*). Solid lines in (*a*) and (*b*) serve as a guide for the eye. Experimental points in (*c*), (*d*), and (*e*) are shown as empty circles while solid curves represent the best fits using the generalized Debye model. The solid red line in (*f*) shows the best fit of the *T*-dependence of the relaxation times taking into account quantum tunnelling of magnetization (QTM), Raman, and Orbach processes, in the 2–15 K range. This best-fit was obtained by the simultaneous fit of $\ln(\tau) = f(T^{-1})$ curves for H_{dc} = 0 Oe and the optimal *dc* field of 100 Oe, with the fixed ΔE barrier of Orbach process (see Fig. S16, S17, S20, and Table S5). Each contribution to the overall relaxation is depicted by a dashed line. The green solid line in (*f*) indicates the linear fitting of the high-temperature data points in the 14–15 K range (see Table 1).

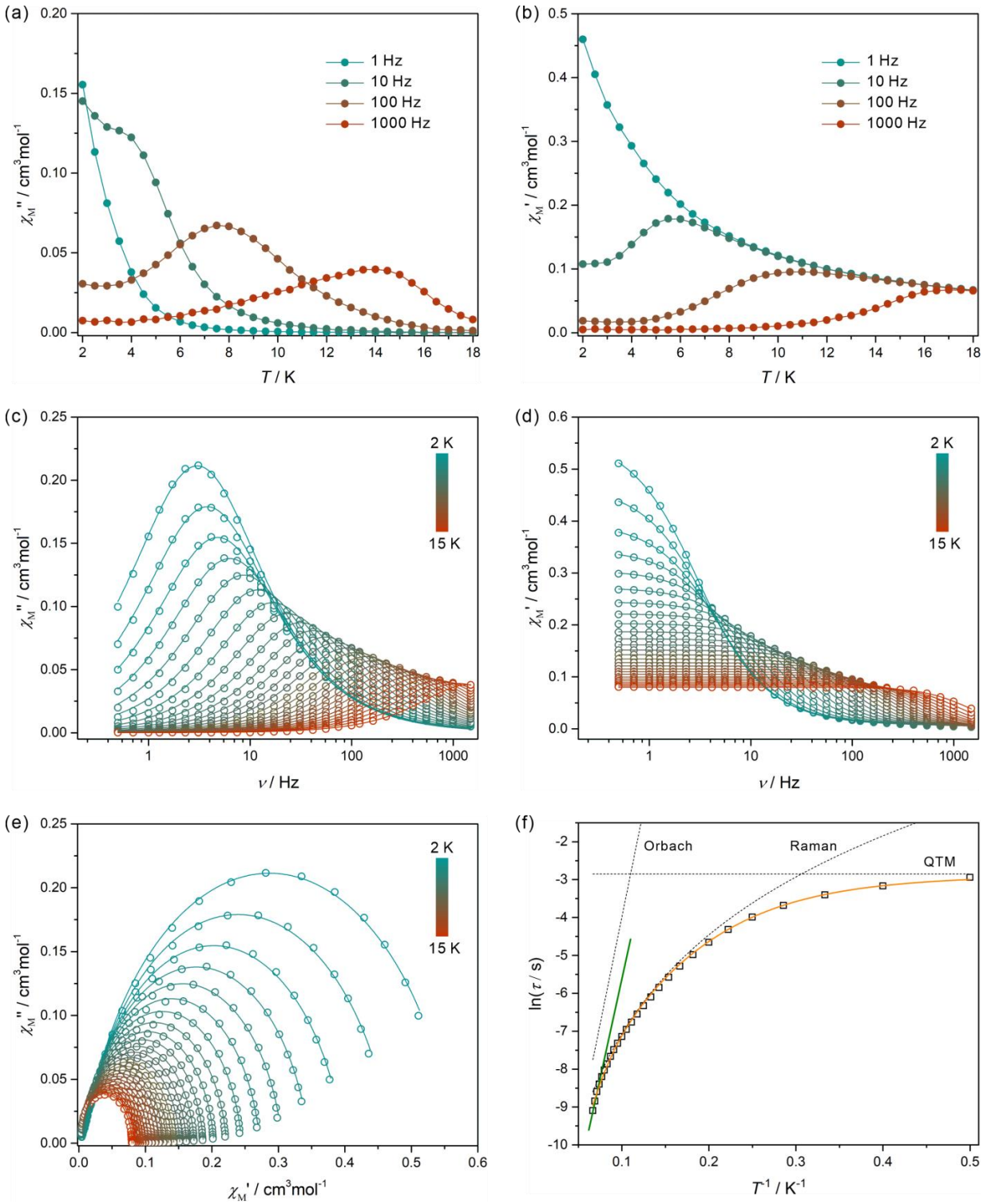

Fig. S13 Complete *T*-variable alternate-current (*ac*) magnetic susceptibility characteristics of **3@Y** under H_{ac} = 3 Oe, H_{dc} = 0 Oe: the *T*-dependence of the out-of-phase molar susceptibility, χ_M", at indicated frequencies from the 1–1000 Hz range (*a*), the *T*-dependence of the in-phase molar susceptibility, χ_M', at indicated frequencies from the 1–1000 Hz range (*b*), the frequency dependence of χ_M" at indicated temperatures from the 2–15 K range (*c*), the analogous frequency dependence of the χ_M' (*d*), the related Argand plots (*e*), and the *T*-dependence of the relaxation time, τ (*f*). Solid lines in (*a*) and (*b*) serve as a guide for the eye. Experimental points in (*c*), (*d*), and (*e*) are shown as empty circles while solid curves represent the best fits using the generalized Debye model. The solid red line in (*f*) shows the best fit of the *T*-dependence of the relaxation times taking into account quantum tunnelling of magnetization (QTM), Raman, and Orbach processes, in the 2–15 K range. This best-fit was obtained by the simultaneous fit of $\ln(\tau) = f(T^{-1})$ curves for H_{dc} = 0 Oe and the optimal *dc* field of 100 Oe, with the fixed ΔE barrier of Orbach process (see Fig. S18–S20, and Table S5). Each contribution to the overall relaxation is depicted by a dashed line. The green solid line in (*f*) indicates the linear fitting of the high-temperature data points in the 14–15 K range (see Table 1).

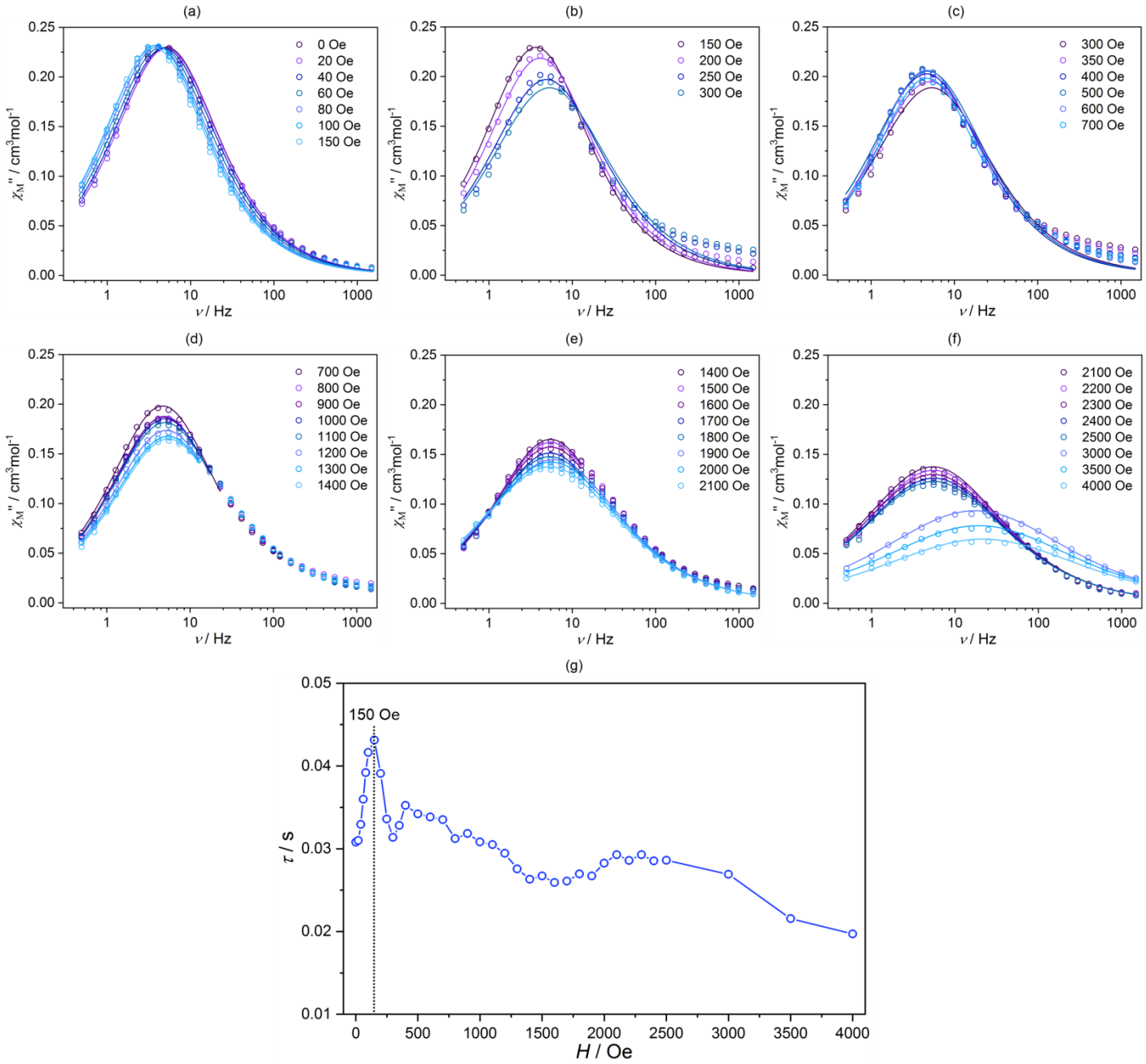

Fig. S14 Frequency dependences of the out-of-phase molar magnetic susceptibility, χ_M'', of **1@Y** collected at 2 K under various indicated *dc* magnetic fields, divided into 6 ranges of 0–150 Oe (*a*), 150–300 Oe (*b*), 300–700 Oe (*c*), 700–1400 Oe (*d*), 1400–2100 Oe (*e*), and 2100–4000 Oe (*f*), together with the resulting field dependence of relaxation times with the indicated optimal *dc* field of 150 Oe (*g*). Solid lines represent the fitting results obtained by using a generalized Debye model. The oscillation effect observed in the field dependence of relaxation times (*g*) is related to the role of hyperfine interactions (see Fig. S28 and further discussion on pages S46–S47).

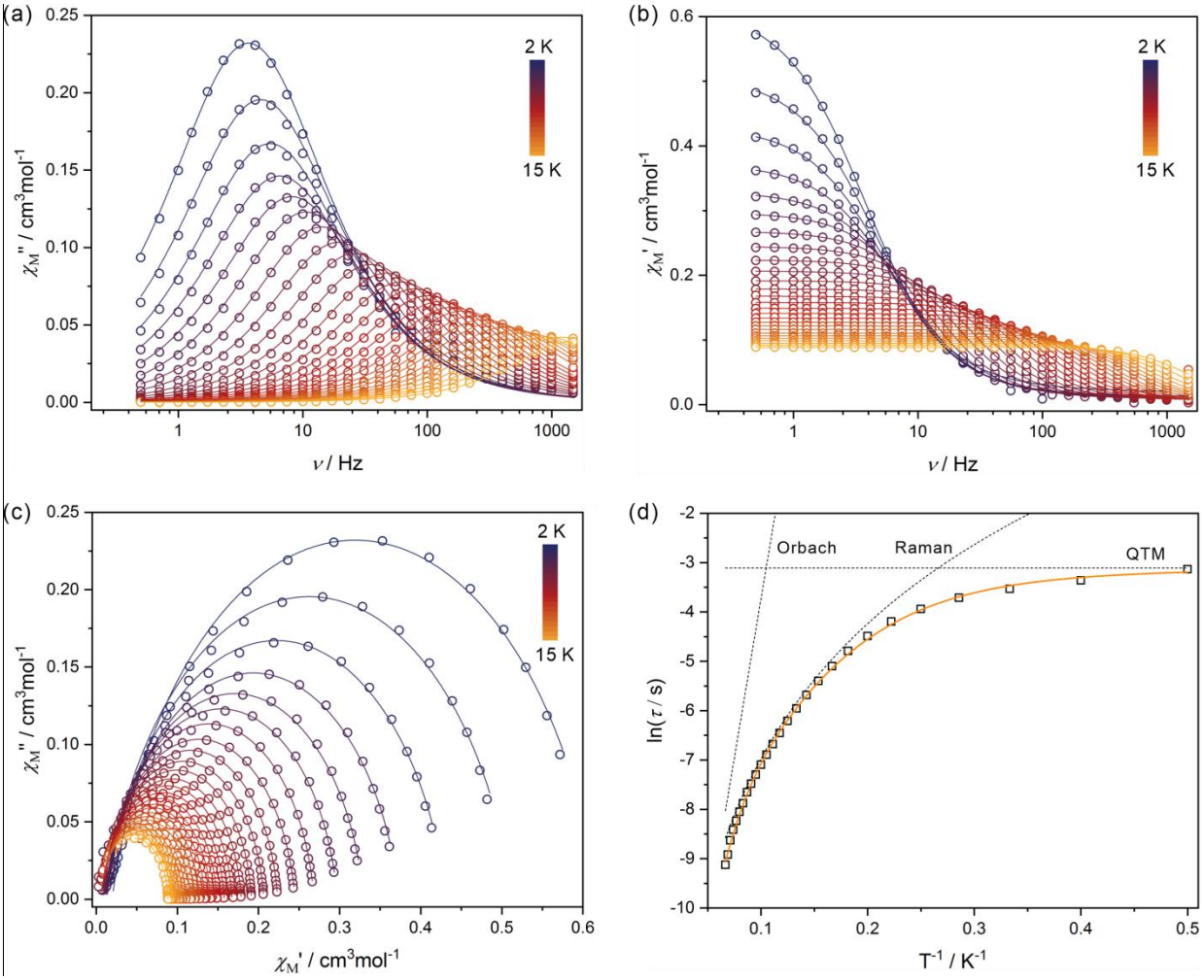

Fig. S15 Complete *T*-variable alternate-current (*ac*) magnetic susceptibility characteristics of **1@Y** under H_{ac} = 3 Oe, H_{dc} = 150 Oe: the frequency dependence of χ_M" at indicated temperatures from the 2–15 K range (*a*), the analogous frequency dependence of the χ_M' susceptibility (*b*), the related Argand plots (*c*), and the *T*-dependence of the relaxation time, τ (*f*). Experimental points in (*a*), (*b*), and (*c*) are shown as empty circles while solid curves represent the best fits using the generalized Debye model. The solid red line in (*d*) shows the best fit of the *T*-dependence of the relaxation times taking into account quantum tunnelling of magnetization (QTM), Raman, and Orbach processes, in the 2–15 K range. This best-fit was obtained by the simultaneous fit of $\ln(\tau) = f(T^{-1})$ curves for H_{dc} = 0 Oe and the optimal *dc* field of 150 Oe, with the fixed ΔE barrier of Orbach process (see Fig. S14, S20, and Table S5). Each contribution to the overall relaxation is depicted by a dashed line.

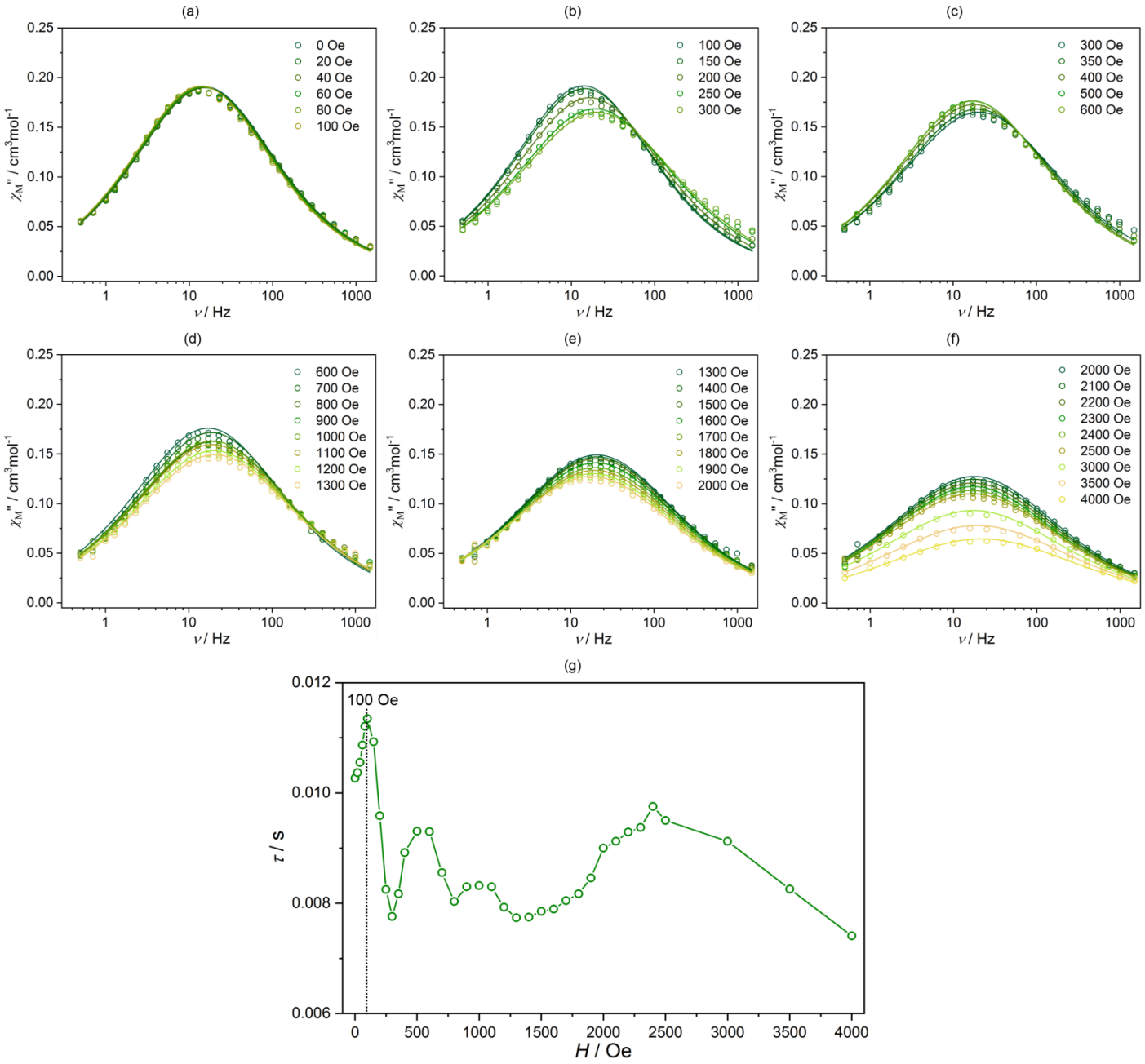

Fig. S16 Frequency dependences of the out-of-phase molar magnetic susceptibility, χ_M'', of **2@Y** collected at 2 K under various indicated *dc* magnetic fields, divided into 6 ranges of 0–100 Oe (*a*), 100–300 Oe (*b*), 300–600 Oe (*c*), 600–1300 Oe (*d*), 1300–2000 Oe (*e*), and 2000–4000 Oe (*f*), together with the resulting field dependence of relaxation times with the indicated optimal *dc* field of 100 Oe (*g*). Solid lines represent the fitting results obtained by using a generalized Debye model. The oscillation effect observed in the field dependence of relaxation times (*g*) is related to the role of hyperfine interactions (see Fig. S28 and further discussion on pages S46–S47).

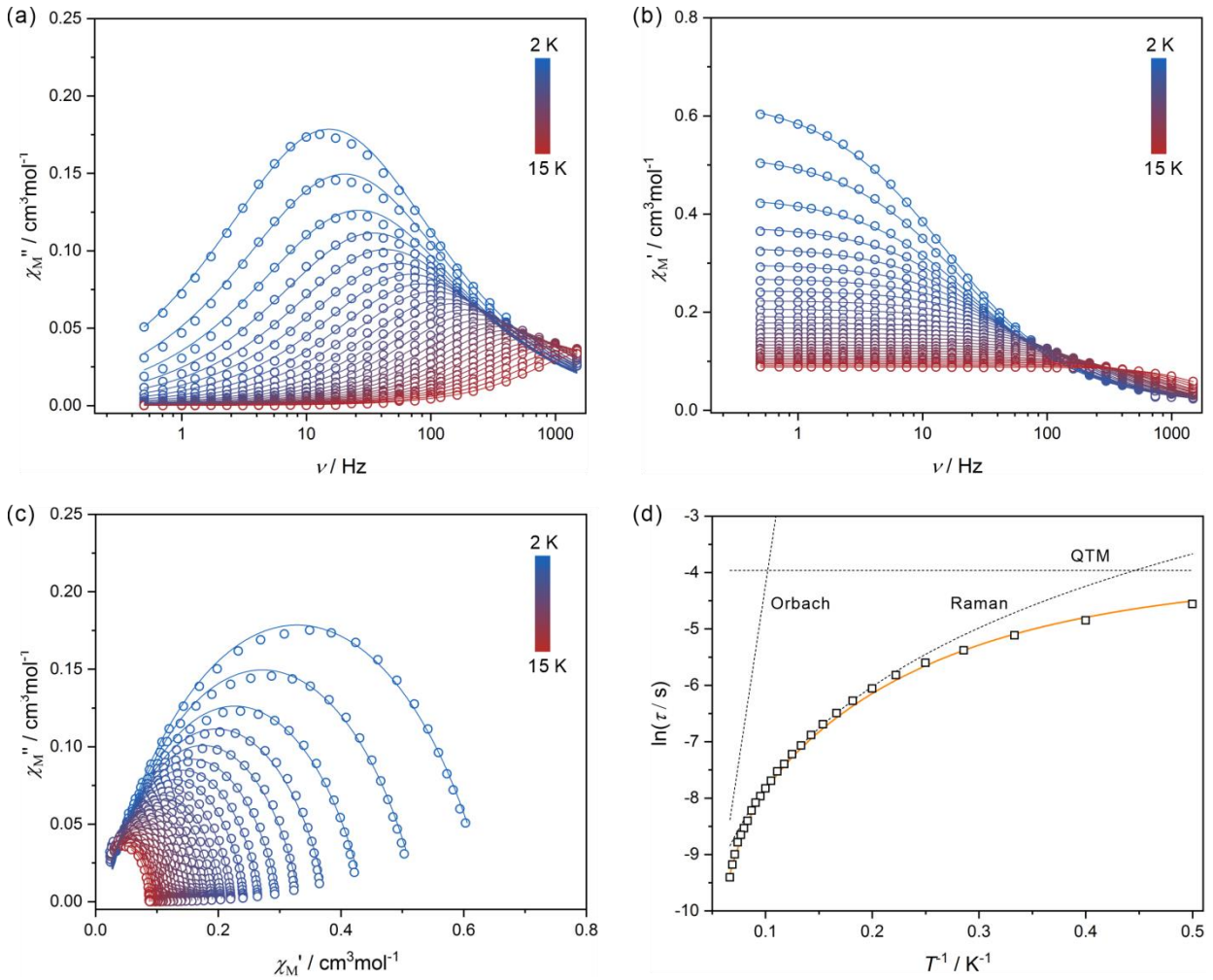

Fig. S17 Complete *T*-variable alternate-current (*ac*) magnetic susceptibility characteristics of **2@Y** under H_{ac} = 3 Oe, H_{dc} = 100 Oe: the frequency dependence of χ_M" at indicated temperatures from the 2–15 K range (*a*), the analogous frequency dependence of the χ_M' susceptibility (*b*), the related Argand plots (*c*), and the *T*-dependence of the relaxation time, τ (*f*). Experimental points in (*a*), (*b*), and (*c*) are shown as empty circles while solid curves represent the best fits using the generalized Debye model. The solid red line in (*d*) shows the best fit of the *T*-dependence of the relaxation times taking into account quantum tunnelling of magnetization (QTM), Raman, and Orbach processes, in the 2–15 K range. This best-fit was obtained by the simultaneous fit of $\ln(\tau) = f(T^{-1})$ curves for H_{dc} = 0 Oe and the optimal *dc* field of 100 Oe, with the fixed ΔE barrier of Orbach process (see Fig. S16, S20, and Table S5). Each contribution to the overall relaxation is depicted by a dashed line.

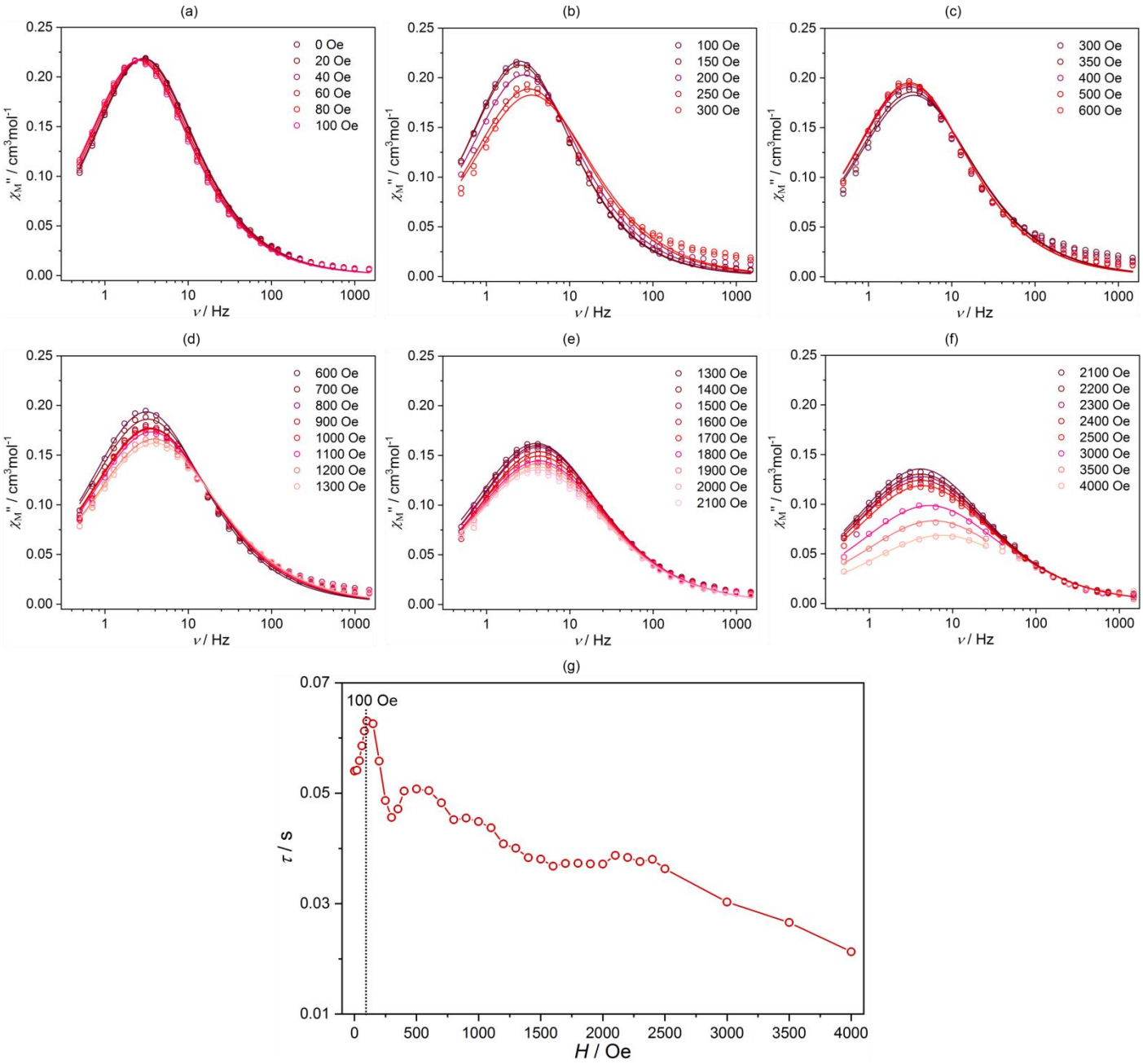

Fig. S18 Frequency dependences of the out-of-phase molar magnetic susceptibility, χ_M'', of **3@Y** collected at 2 K under various indicated *dc* magnetic fields, divided into 6 ranges of 0–100 Oe (*a*), 100–300 Oe (*b*), 300–600 Oe (*c*), 600–1300 Oe (*d*), 1300–2100 Oe (*e*), and 2100–4000 Oe (*f*), together with the resulting field dependence of relaxation times with the indicated optimal *dc* field of 100 Oe (*g*). Solid lines represent the fitting results obtained by using a generalized Debye model. The oscillation effect observed in the field dependence of relaxation times (*g*) is related to the role of hyperfine interactions (see Fig. S28 and further discussion on pages S46–S47).

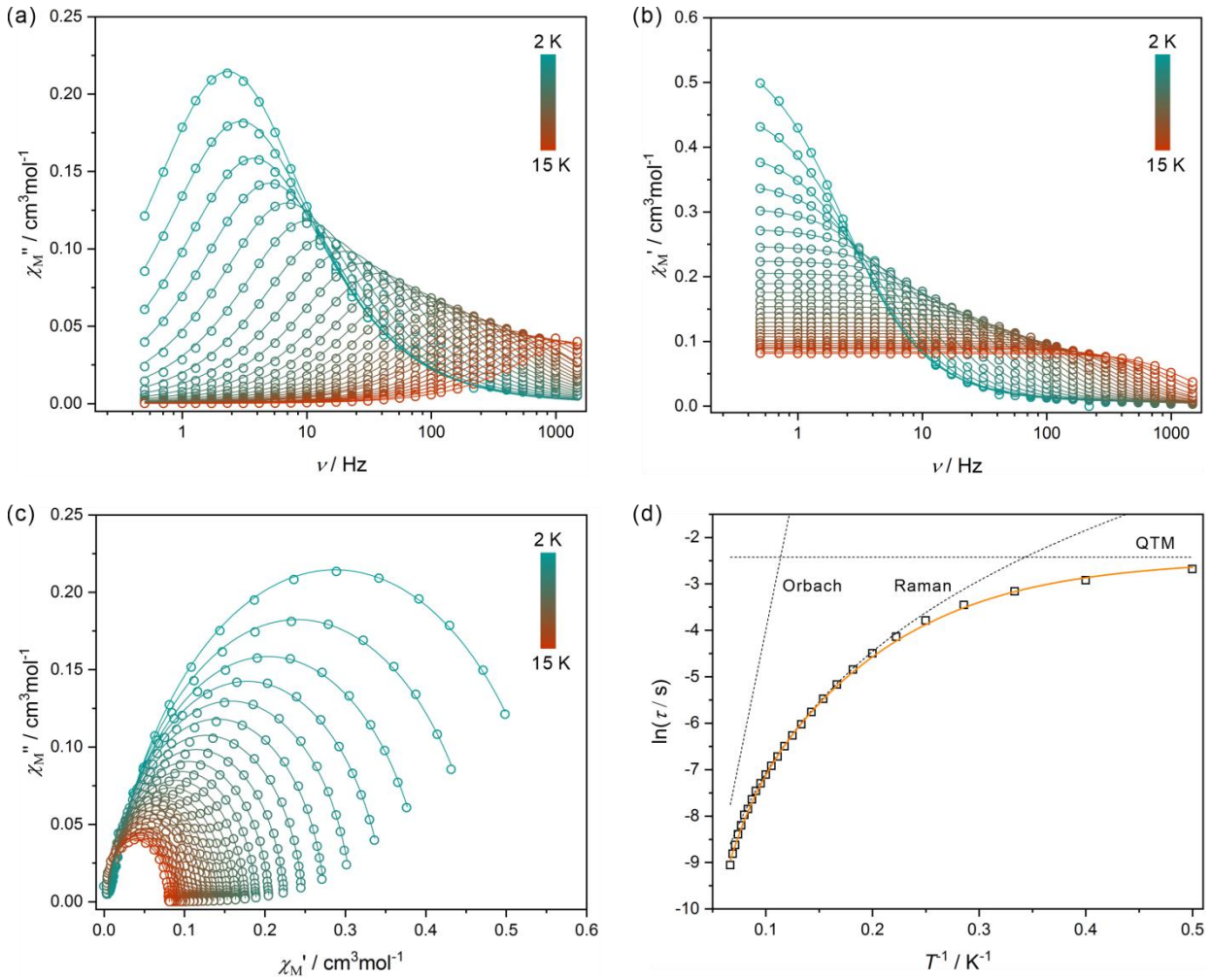

Fig. S19 Complete *T*-variable alternate-current (*ac*) magnetic susceptibility characteristics of **3@Y** under H_{ac} = 3 Oe, H_{dc} = 100 Oe: the frequency dependence of χ_M" at indicated temperatures from the 2–15 K range (*a*), the analogous frequency dependence of the χ_M' susceptibility (*b*), the related Argand plots (*c*), and the *T*-dependence of the relaxation time, τ (*f*). Experimental points in (*a*), (*b*), and (*c*) are shown as empty circles while solid curves represent the best fits using the generalized Debye model. The solid red line in (*d*) shows the best fit of the *T*-dependence of the relaxation times taking into account quantum tunnelling of magnetization (QTM), Raman, and Orbach processes, in the 2–15 K range. This best-fit was obtained by the simultaneous fit of $\ln(\tau) = f(T^{-1})$ curves for H_{dc} = 0 Oe and the optimal *dc* field of 100 Oe, with the fixed ΔE barrier of Orbach process (see Fig. S18, S20, and Table S5). Each contribution to the overall relaxation is depicted by a dashed line.

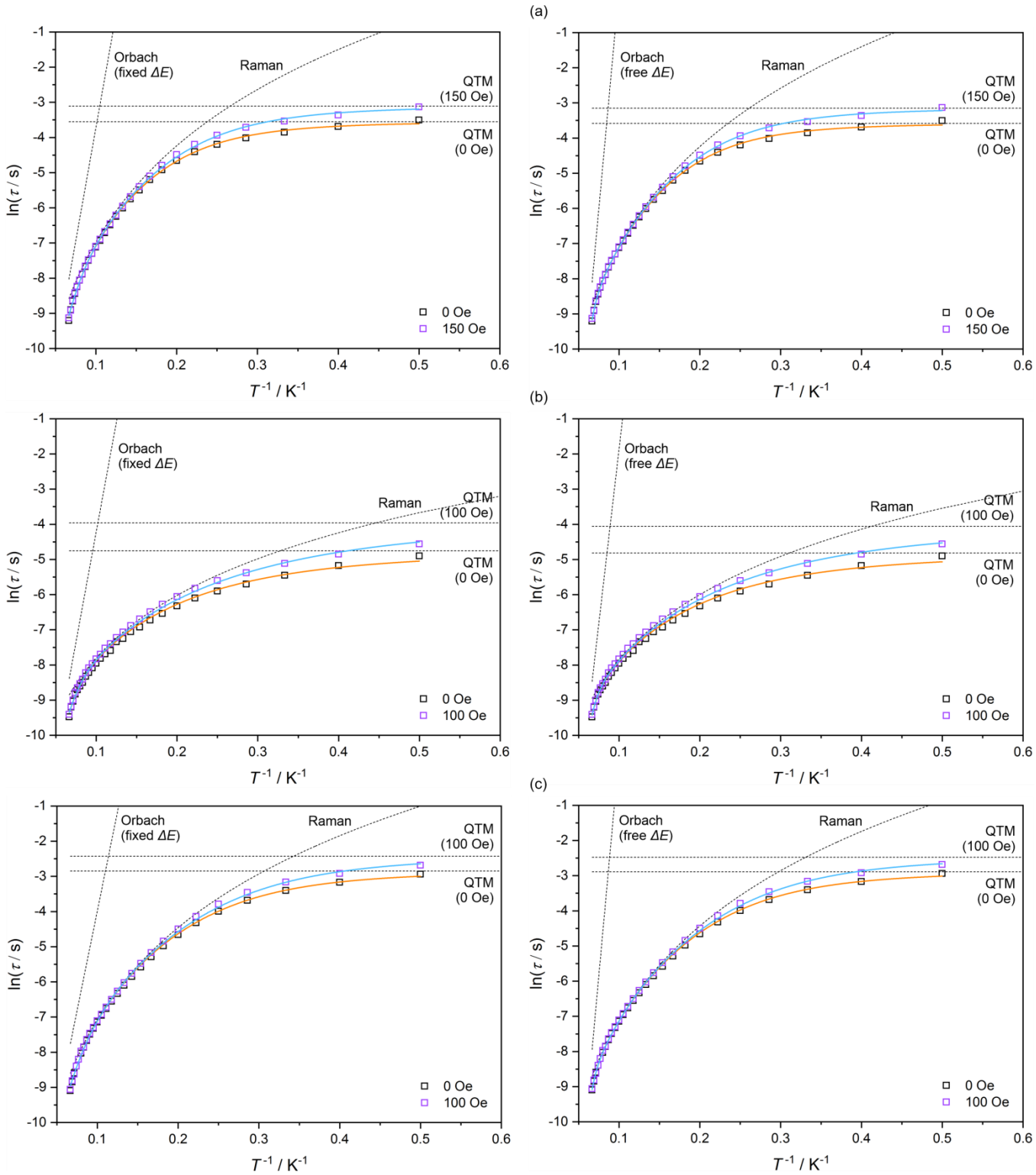

Fig. S20 Comparison of the results of the simultaneous fits of the *T*-dependences of magnetic relaxation times, ln(τ) = f(T^{-1}), for the zero and optimal *dc* fields for **1@Y** (*a*), **2@Y** (*b*), and **3@Y** (*c*). The related frequency dependences of χ_M" are shown in Fig. S11–S13, S15, S17, and S19. The optimal *dc* fields, of 150 Oe for **1@Y** or 100 Oe for **2@Y** and **3@Y,** were selected using the *dc*-field-dependent *ac* magnetic data (Fig. S14, S16, and S18). The fittings were performed following the equation (1) (the main text), taking into account contributions from Orbach relaxation (ΔE and τ_0 parameters), Raman relaxation (C_{Raman} and *n* parameters), and a QTM effect (τ_{QTM} parameter). The parameters of Orbach and Raman relaxation were fitted with the identical values for both *dc* fields as these processes are independent on the *dc* magnetic field while the τ_{QTM} parameter was separate for two fields, thus, two QTM-related parameters, $\tau_{QTM,0}$ and $\tau_{QTM,optimal\ field}$ were fitted. The left panel represents the fitting with the fixed energy barrier (ΔE) of Orbach relaxation (taken from *ab initio* calculations) while the right panel shows the fitting with the free value of ΔE. The contributions from all relaxation processes were depicted. The best-fit parameters are listed in Table S5.

Table S5 Best-fit parameters for the simultaneous fits of the temperature dependences of magnetic relaxation times for the zero and optimal *dc* fields for **1@Y** (optimal *dc* field of 150 Oe, Fig. S14), **2@Y** (optimal *dc* field of 100 Oe, Fig. S16), and **3@Y** (optimal *dc* field of 100 Oe, Fig. S18). The best-fit parameters are shown for two alternative fitting procedures: the first performed with the fixed energy barrier (ΔE) of Orbach relaxation pathway (taken from *ab initio* calculations), and the second performed with the free value of ΔE. The related best-fit curves are shown in Fig. S20. The selected part of these results (best-fit parameters corresponding to the zero-*dc*-field magnetic relaxation, obtained using the fixed energy barrier of Orbach relaxation) is also presented in Table 1 (the main text).

compound	**1@Y**		**2@Y**		**3@Y**	
type of fitting (Fig. S20)	fitting with fixed ΔE (from *ab initio*, Table S8)	fitting with free ΔE	fitting with fixed ΔE (from *ab initio*, Table S8)	fitting with free ΔE	fitting with fixed ΔE (from *ab initio*, Table S8)	fitting with free ΔE
ΔE in cm^{-1} [$\Delta E/k_B$ in K]	89.8 cm^{-1} [129.2 K]	174(11) cm^{-1} [250(15) K]	86.7 cm^{-1} [124.8 K]	138(13) cm^{-1} [198(19) K]	78.7 cm^{-1} [113.2 K]	175(11) cm^{-1} [252(16) K]
τ_0 / s	$6.0(6)\cdot10^{-8}$	$1.7(9)\cdot10^{-11}$	$5.5(6)\cdot10^{-8}$	$4(2)\cdot10^{-10}$	$2.3(3)\cdot10^{-7}$	$1.8(9)\cdot10^{-11}$
C_{Raman} / $s^{-1}K^{-n}$	0.12(2)	0.095(6)	6.6(8)	5.4(6)	0.20(2)	0.163(8)
n	3.95(5)	4.10(3)	2.57(5)	2.68(5)	3.77(4)	3.88(2)
τ_{QTM} for H_{dc} = 0 Oe / s	0.0286(9)	0.0278(6)	0.0086(6)	0.0081(5)	0.058(3)	0.0556(15)
τ_{QTM} for optimal *dc* field / s	0.0446(15)	0.043(2)	0.019(2)	0.017(2)	0.088(5)	0.084(3)

Comment to Fig. S8–S19

To fit the frequency dependences *ac* magnetic susceptibilities, χ_M' and χ_M" of **1**, **2**, **3**, **1@Y**, **2@Y**, and **3@Y** at the indicated temperatures and *dc* magnetic fields (Fig. S8–S19), the generalized Debye model for a single relaxation process were used with the following equations (e1) and (e2):

$$\chi'(\omega) = \chi_S + (\chi_T - \chi_S)\frac{1+(\omega\tau)^{1-\alpha}\sin(\pi\alpha/2)}{1+2(\omega\tau)^{1-\alpha}\sin(\pi\alpha/2)+(\omega\tau)^{2(1-\alpha)}} \quad \text{(e1)}$$

$$\chi''(\omega) = (\chi_T - \chi_S)\frac{(\omega\tau)^{1-\alpha}\cos(\pi\alpha/2)}{1+2(\omega\tau)^{1-\alpha}\sin(\pi\alpha/2)+(\omega\tau)^{2(1-\alpha)}} \quad \text{(e2)}$$

where

χ_S = the adiabatic susceptibility (at the infinitely high frequency of *ac* field),

χ_T = the isothermal susceptibility (at the infinitely low frequency of *ac* field),

τ = the relaxation time,

α = the distribution (Cole-Cole) parameter,

and ω is an angular frequency, that is $\omega = 2\pi\nu$, with ν being for the linear frequency in [Hz] units.[S9–S10]

(S9) Y.-N. Guo, G.-F. Xu, Y. Guo and J. Tang, *Dalton Trans.*, 2011, **40**, 9953–9963.

(S10) M. Ramos Silva, P. Martin-Ramos, J. T. Coutinho, L. C. J. Pereira and J. Martin-Gil, *Dalton Trans.*, 2014, **43**, 6752–6761.

Details of the *ab initio* calculations of the Ho^{III} crystal field effect in 1–3

The *ab initio* calculations were carried out using *OpenMolcas* quantum chemistry software package and were performed on the experimental geometries of **1, 2** and **3** taken from the single-crystal X-ray diffraction analysis (Figure S21).[S11] Three models with the different basis sets were used (Table S6): (*a*) the small basis sets with the VDZP basis function quality for Ho^{3+} central ion and the VDZ for other atoms, named **1S**, **2S**, and **3S** models for **1**, **2**, and **3**, respectively, (*b*) the large basis sets with the VTZP basis for Ho^{III} and the VDZP for atom in its first coordination sphere, named **1L**, **2L**, and **3L** models for **1**, **2**, and **3**, respectively, (*c*) the very large basis sets with the VQZP basis for Ho^{III} centres, the VTZP for atom in their first coordination sphere, and the VDZP for all other atoms, named **1V**, **2V**, and **3V** models for **1**, **2**, and **3**, respectively. Table S6 contains the descriptions of the employed basis sets for all atoms. Moreover, for each basis set two different fragments of the crystal structures of **1**–**3** were used for calculations. They are visualized on Figure S21. The first cluster contains the whole molecular unit with all atoms connected by covalent bonds, while the second cluster, denoted with the additional **W** (standing for water), for example, **1S-W**, **2V-W** etc., takes into account also two molecules of crystallization water connected by hydrogen bonds to the water belonging to the first coordination sphere.

The performed *ab initio* calculations were of a CASSCF/RASSI/SINGLE_ANISO type.[S12–S13] Scalar relativistic effects were taken into account by employing the second-order DKH (Douglas-Kroll-Hess) Hamiltonian and the relativistic basis sets of an ANO-RCC type. To save disk space, the Cholesky decomposition of ERI-s (electron repulsion integrals) was used with the $1.0 \cdot 10^{-8}$ threshold. In the first step, the state average multi-configurational self-consistent field (SA-CASSCF) calculation for 35 quintets, 210 triplets and 196 singlets rising from different configurations of Ho^{III} was carried out. The active space was composed of seven 4f-orbitals of Ho^{III} with 10 active electrons – CAS(10in7). In the next step, 35 quintets (all), 128 triplets, and 130 singlets optimized as spin-free states in SA-CASSCF were mixed by the spin-orbit coupling within RASSI (Restricted Active Space State Interaction Program), resulting in the 689 spin-orbit states. In the final step, the SINGLE_ANISO module was used to decompose spin-orbit states into states with the definite projection of the total momentum on the located quantization axis, then, to adjust tunnelling gaps of nearly degenerated ground states, and to simulate *dc* magnetic curves, including *M(H)* and $\chi_M T(T)$ dependences. For the selected SMM molecule of **3** (showing the purest ground m_J quasi-doublet state with the lowest tunnelling gap), the additional calculation was performed for the fragment containing two molecules of water of crystallization within the **L** basis set with the enlarged active space using the RASSCF scheme consisting of three 5p orbitals with 6 electrons in RAS1, seven 4f orbitals with 10 electrons in RAS2, and five 5d orbitals in RAS3, wherein the RAS1 two holes were allowed, within the RAS2 complete active space calculation is performed, and in the RAS3 two excitation were considered. We called this model **3L-W-(active space)**, and the related active space was labelled as CAS(16in15). The obtained energy splitting (with tunnelling splitting) for every model, together with the g_z component of pseudo-g-tensors, and the composition of ground nearly degenerated doublets in the $|J = 8, m_J\rangle$ basis on quantization axis of each state are presented in Table S7 (**1S**, **1S-W**, **2S**, **2S-W**, **3S**, and **3S-W** models), Table S8 (**1L**, **1L-W**, **2L**, **2L-W**, **3L**, and **3L-W** models), Table S9 (**1V**, **1V-W**, **2V**, **2V-W**, **3V**, and **3V-W** models), and Table S10 (**3L-W-(active-space)** model compared with the results of **3L-W** model).

The comparison of the simulated *M*(*H*) and $\chi_M T(T)$ dependences, obtained by using the large basis sets of **1L-W**, **2L-W**, and **3L-W** models, with the experimental *dc* magnetic characteristics was shown in Fig. S7. These basis sets well suited to the experimental data but the very similar simulated *M*(*H*) and $\chi_M T(T)$ curves were also obtained by using the other models (Fig. S22). It means that the comparison with the experimental *dc* magnetic curves could not serve to judge which of the models is the most reliable. However, the observation of zero-*dc*-field slow magnetic relaxation in **1**, **2**, and **3** indicate that the tunnelling gaps should be very small. Therefore, as the most reliable, we selected the results obtained by using the large basis sets employing both the bimetallic molecule and water of crystallization (**1L-W**, **2L-W**, and **3L-W** models, for **1**, **2**, and **3**, respectively), which gave the lowest values of tunnelling gaps (Table S8). The related results of the energy splitting of the ground multiplet of Ho^{III} were visualized

in Fig. 3, which was done in an approximate way using the average energies for the pairs of lowest-lying m_J levels. Besides, in Fig. 1 (for compound **1**) and Fig. S21 (for compounds **1**–**3**), we visualized the quantization axes of the ground quasi non-Kramers doublet (easy magnetic axes) computed by using **1L-W**, **2L-W**, and **3L-W** models (Table S8). The values of tunnelling gaps, obtained within these models, were also used to obtain the tunnelling splitting which was found to correlate well with the experimental values of relaxation times related to the quantum tunnelling of magnetization effect (QTM, Fig. S23). The **1L-W**, **2L-W**, and **3L-W** models were also employed in the discussion on the impact of hyperfine interactions on the electronic structure of Ho^{III} centres in **1**–**3** (see below).

(S11) I. F. Galvam, M. Vacher, A. Alavi, C. Angeli, F. Aquilante, J. Autschbach, J. J. Bao, S. I. Bokarev, N. A. Bogdanov, R. K. Carlson, L. F. Chibotaru, J. Creutzberg, N. Dattani, M. G. Delcey, S. S. Dong, A. Dreuw, L. Freitag, L. M. Frutos, L. Gagliardi, F. Gendron, A. Giussani, L. Gonzalez, G. Grell, M. Guo, C. E. Hoyer, M. Johansson, S. Keller, S. Knecht, G. Kovacevic, E. Kallman, G. L. Manni, M. Lundberg, Y. Ma, S. Mai, J. P. Malhado, P. A. Malmqvist, P. Marquetand, S. A. Mewes, J. Norell, M. Olivucci M., Oppel, Q. M. Phung, K. Perloot, F. Plasser, M. Reiher, A. M. Sand, I. Schapiro, P. Sharma, C. J. Stein, L. K. Sorensen, D. G. Truhlar, M. Ugandi, L. Ungur, A. Valentini, S. Vancoillie, V. Veryazov, O. Weser, T. A. Wesołowski, P.-O. Widmark, S. Wouters, A. Zech, J. P. Zobel, and R. Lindh, *J. Chem. Theory Comput*., 2019, **15**, 5925–5964.

(S12) L. F. Chibotaru and L. Ungur, *J. Chem. Phys*., 2012, **137**, 064112.

(S13) L. Ungur and L. F. Chibotaru, *Chem. Eur. J*., 2017, **23**, 3708–3718.

Table S6 Description of the basis sets of three different models: small **S**, large **L**, and very large **V**, employed in the *ab initio* calculations of the Ho^{III} crystal field effect in **1–3**.

model S	**model L**	**model V**
Ho.ANO-RCC…7S6P4D2F1G	Ho.ANO-RCC…8S7P5D3F2G1H	Ho.ANO-RCC...9S8P6D4F3G2H
Co.ANO-RCC…5S4P2D	Co.ANO-RCC...5S4P2D	Co.ANO-RCC...5S4P2D1F
Rh.ANO-RCC…6S5P3D	Rh.ANO-RCC...6S5P3D	Rh.ANO-RCC...6S5P3D1F
Ir.ANO-RCC…7S6P4D1F	Ir.ANO-RCC 7S6P4D1F	Ir.ANO-RCC...7S6P4D2F
C.ANO-RCC…3S2P	C.ANO-RCC...3S2P	C.ANO-RCC...3S2P1D
O.ANO-RCC…3S2P	O.ANO-RCC...3S2P1D (first coordination sphere)	O.ANO-RCC...4S3P2D1F (first coordination sphere)
H.ANO-RCC…2S	O.ANO-RCC...3S2P (others)	O.ANO-RCC...3S2P1D (others)
N.ANO-RCC…3S2P	H.ANO-RCC...2S	H.ANO-RCC...2S1P
-	N.ANO-RCC...3S2P1D (first coordination sphere)	N.ANO-RCC...4S3P2D1F (first coordination sphere)
-	N.ANO-RCC...3S2P (others)	N.ANO-RCC...3S2P1D (others)

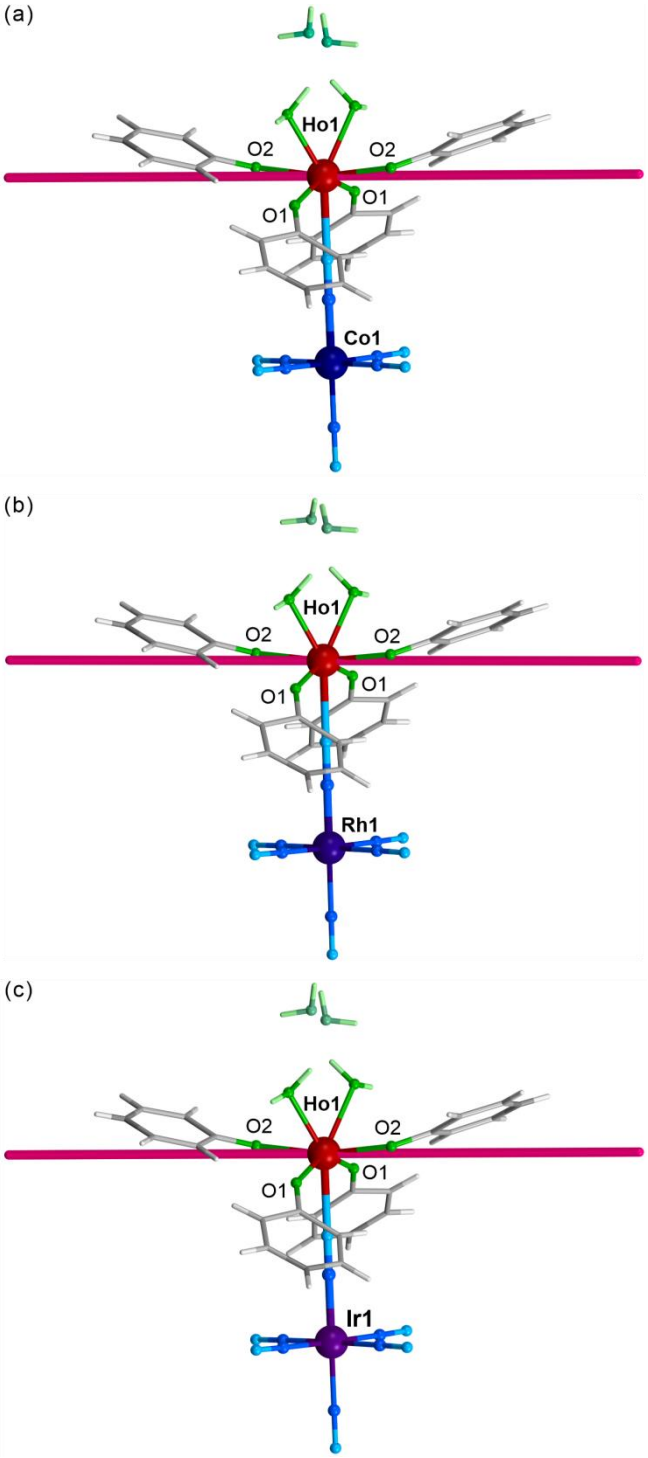

Fig. S21 Visualization of the representative fragments of the crystal structures of **1** (*a*), **2** (*b*), and **3** (*c*) used for the *ab initio* calculations with the labelling of metal centers (Ho1 and Co1/Rh1/Ir1) and critical coordinated oxygen atoms of 4-pyridone ligands (O1 and O2), together with the indicated directions of the main magnetic axis (violet sticks) of the ground quasi non-Kramers doublets. Within three different basis sets (small, large, and very large, presented in Table S6), the calculations were performed for two structural fragments: the first involving only the atoms of dinuclear molecules, while the second involving also two molecules of water of crystallization, shown in this figure, which are hydrogen bonded with water molecules coordinated to Ho1 centres.

Table S7 The energy splitting (in cm^{-1}) of the $^5I_8$ ground multiplet of Ho^{III} centres in **1**–**3** obtained by using the small basis sets (Table S6) with two different models employing only the dinuclear molecule (**1S**, **2S**, **3S**, for **1**, **2**, and **3**, respectively) or the dinuclear molecule along with water of crystallization (**1S-W**, **2S-W**, **3S-W**, for **1**, **2**, and **3**, respectively). Together with the energy splitting, also the g_z components of pseudo-*g*-tensors of each ground quasi non-Kramers doublets and their composition in the $|J = 8, m_J\rangle$ basis were presented.

1S (small basis set, compound **1**)		**2S** (small basis set, compound **2**)		**3S** (small basis set, compound **3**)	
1S	**1S-W**	**2S**	**2S-W**	**3S**	**3S-W**
0.000	0	0.000	0	0.000	0
0.256	**0.186**	**0.346**	**0.284**	**0.229**	**0.149**
95.852	78.689	93.956	74.464	93.384	69.512
96.671	80.451	95.185	78.883	95.493	71.733
121.781	88.258	109.487	78.949	103.894	78.613
129.048	99.776	116.589	93.446	113.708	93.617
139.053	108.323	128.916	100.862	127.543	98.520
153.915	125.454	142.660	117.979	145.070	120.049
203.461	183.731	201.211	183.521	196.505	177.944
215.601	191.748	217.214	195.464	207.664	184.584
233.431	210.035	230.812	208.874	224.662	201.283
251.485	232.706	249.254	232.108	242.865	225.543
254.245	235.253	249.413	232.774	243.998	225.727
257.248	251.279	261.085	255.601	254.226	249.441
268.188	253.395	268.699	257.850	259.649	250.639
293.598	276.898	296.471	280.857	290.387	274.618
295.594	277.733	297.524	281.339	290.676	274.726
Pseudo-*g*-tensor g_z components within basis of two lowest energy states: ($g_x = g_y = 0$ according to Griffiths Theorem)					
19.588	19.559	19.568	19.536	19.582	19.553
Composition of two lowest energy states (I and II) in $\|m_J\rangle$ basis on the quantization axis within $J = 8$ manifold (only components with contribution above 0.09%)					

I	II	I	II	I	II	I	II	I	II	I	II
48.2% $\|\pm 8\rangle$	48.4% $\|\pm 8\rangle$	48.0% $\|\pm 8\rangle$	48.2% $\|\pm 8\rangle$	48.1% $\|\pm 8\rangle$	48.4% $\|\pm 8\rangle$	47.9% $\|\pm 8\rangle$	48.2% $\|\pm 8\rangle$	48.2% $\|\pm 8\rangle$	48.3% $\|\pm 8\rangle$	48.0% $\|\pm 8\rangle$	48.1% $\|\pm 8\rangle$
1.4% $\|\pm 5\rangle$	1.3% $\|\pm 5\rangle$	1.5% $\|\pm 5\rangle$	1.5% $\|\pm 5\rangle$	1.5% $\|\pm 5\rangle$	1.4% $\|\pm 5\rangle$	1.6% $\|\pm 5\rangle$	1.6% $\|\pm 5\rangle$	1.4% $\|\pm 5\rangle$	1.4% $\|\pm 5\rangle$	1.6% $\|\pm 5\rangle$	1.6% $\|\pm 5\rangle$
0.1% $\|\pm 3\rangle$	0.1% $\|\pm 3\rangle$	0.1% $\|\pm 3\rangle$	0.1% $\|\pm 3\rangle$	0.2% $\|\pm 3\rangle$	0.1% $\|\pm 3\rangle$	0.1% $\|\pm 3\rangle$	0.1% $\|\pm 3\rangle$	0.1% $\|\pm 3\rangle$	0.1% $\|\pm 3\rangle$	0.1% $\|\pm 3\rangle$	0.1% $\|\pm 3\rangle$

Table S8 The energy splitting (in cm^{-1}) of the $^5I_8$ ground multiplet of Ho^{III} centres in **1**–**3** obtained by using the large basis sets (Table S6) with two different models employing only the dinuclear molecule (**1L**, **2L**, **3L**, for **1**, **2**, and **3**, respectively) or the dinuclear molecule along with water of crystallization (**1L-W**, **2L-W**, **3L-W**, for **1**, **2**, and **3**, respectively). Together with the energy splitting, also the g_z components of pseudo-*g*-tensors of each ground quasi non-Kramers doublets and their composition in the $|J = 8, m_J\rangle$ basis were presented.

1L (large basis set, compound **1**)		**2L** (large basis set, compound **2**)		**3L** (large basis set, compound **3**)	
1L	**1L-W**	**2L**	**2L-W**	**3L**	**3L-W**
0	0	0	0	0	0
0.182	**0.119**	**0.257**	**0.195**	**0.165**	**0.092**
106.177	88.705	105.653	85.674	103.263	78.349
106.689	90.902	106.380	87.618	104.778	79.146
129.685	95.307	119.177	90.449	112.669	87.842
135.994	106.052	125.516	102.253	121.988	101.597
148.148	116.557	138.721	109.755	135.995	105.737
162.060	132.401	151.843	126.181	153.914	127.548
208.629	188.796	207.363	189.661	202.277	183.233
220.933	196.629	223.718	201.898	212.734	189.143
238.392	213.565	237.756	214.990	231.404	207.076
258.407	238.551	257.414	239.814	250.525	232.092
261.544	241.202	258.558	240.338	253.563	233.421
265.166	259.976	270.220	265.423	262.701	258.603
273.645	261.258	276.663	266.885	267.258	259.375
300.106	282.950	303.116	287.023	295.402	279.045
301.954	283.711	304.490	287.725	296.077	279.158
Pseudo-*g*-tensor g_z components within basis of two lowest energy states: ($g_x = g_y = 0$ according to Griffiths Theorem)					
19.604	19.579	19.591	19.565	19.597	19.570
Composition of two lowest energy states (I and II) in $\|m_J\rangle$ basis on the quantization axis within $J = 8$ manifold (only components with contribution above 0.09%)					

I	II	I	II	I	II	I	II	I	II	I	II
48.3% $\|\pm 8\rangle$	48.4% $\|\pm 8\rangle$	48.1% $\|\pm 8\rangle$	48.2% $\|\pm 8\rangle$	48.2% $\|\pm 8\rangle$	48.4% $\|\pm 8\rangle$	48.1% $\|\pm 8\rangle$	48.2% $\|\pm 8\rangle$	48.2% $\|\pm 8\rangle$	48.4% $\|\pm 8\rangle$	48.1% $\|\pm 8\rangle$	48.2% $\|\pm 8\rangle$
1.3% $\|\pm 5\rangle$	1.3% $\|\pm 5\rangle$	1.5% $\|\pm 5\rangle$	1.5% $\|\pm 5\rangle$	1.4% $\|\pm 5\rangle$	1.4% $\|\pm 5\rangle$	1.6% $\|\pm 5\rangle$	1.6% $\|\pm 5\rangle$	1.4% $\|\pm 5\rangle$	1.4% $\|\pm 5\rangle$	1.5% $\|\pm 5\rangle$	1.5% $\|\pm 5\rangle$
0.1 % $\|\pm 6\rangle$	0.2% $\|\pm 6\rangle$	0.1% $\|\pm 6\rangle$	0.1% $\|\pm 6\rangle$	0.1% $\|\pm 6\rangle$	0.1% $\|\pm 6\rangle$	0.1% $\|\pm 6\rangle$	0.1% $\|\pm 6\rangle$	0.1% $\|\pm 6\rangle$	0.1% $\|\pm 6\rangle$	0.1% $\|\pm 6\rangle$	0.1% $\|\pm 6\rangle$

Table S9 The energy splitting (in cm^{-1}) of the $^5I_8$ ground multiplet of Ho^{III} centres in **1**–**3** obtained by using the very large basis sets (Table S6) with two different models employing only the dinuclear molecule (**1V**, **2V**, **3V**, for **1**, **2**, and **3**, respectively) or the dinuclear molecule along with water of crystallization (**1V-W**, **2V-W**, **3V-W**, for **1**, **2**, and **3**, respectively). Together with the energy splitting, also the g_z components of pseudo-*g*-tensors of each ground quasi non-Kramers doublets and their composition in the $|J = 8, m_J\rangle$ basis were presented.

1V (very large basis set, compound **1**)		**2V** (very large basis set, compound **2**)		**3V** (very large basis set, compound **3**)	
1V	**1V-W**	**2V**	**2V-W**	**3V**	**3V-W**
0.000	0.000	0.000	0.000	0.000	0.000
0.193	**0.137**	**0.276**	**0.219**	**0.183**	**0.121**
103.632	88.196	103.288	85.973	100.648	80.089
104.385	90.190	104.353	89.945	102.453	83.981
131.471	99.362	121.902	91.537	114.778	87.443
138.618	110.399	128.922	105.210	124.841	3.837
150.645	121.424	142.174	114.465	138.832	11.175
165.109	137.629	155.359	130.579	157.067	32.578
210.876	192.529	210.081	193.202	204.939	87.471
221.565	198.710	225.055	203.820	213.731	191.894
239.976	217.099	239.885	218.151	233.514	211.390
262.660	244.374	262.382	245.163	255.433	238.498
264.962	246.289	262.829	245.390	257.754	239.415
267.968	263.348	273.387	269.123	266.005	262.396
275.712	264.684	279.421	270.499	270.237	263.245
303.736	288.406	306.810	292.001	299.133	284.672
305.318	289.086	308.142	292.735	299.724	284.791
Pseudo-*g*-tensor g_z components within basis of two lowest energy states: ($g_x = g_y = 0$ according to Griffiths Theorem)					
19.631	19.610	19.618	19.597	19.623	19.601
Composition of two lowest energy states (I and II) in $\|m_J\rangle$ basis on the quantization axis within $J = 8$ manifold (only components with contribution above 0.09%)					

I	II	I	II	I	II	I	II	I	II	I	II
48.5% $\|\pm 8\rangle$	48.6% $\|\pm 8\rangle$	48.4% $\|\pm 8\rangle$	48.5% $\|\pm 8\rangle$	48.4% $\|\pm 8\rangle$	48.6% $\|\pm 8\rangle$	48.3% $\|\pm 8\rangle$	48.5% $\|\pm 8\rangle$	48.4% $\|\pm 8\rangle$	48.6% $\|\pm 8\rangle$	48.3% $\|\pm 8\rangle$	48.4% $\|\pm 8\rangle$
1.2% $\|\pm 5\rangle$	1.2% $\|\pm 5\rangle$	1.3% $\|\pm 5\rangle$	1.3% $\|\pm 5\rangle$	1.3% $\|\pm 5\rangle$	1.2% $\|\pm 5\rangle$	1.4% $\|\pm 5\rangle$	1.4% $\|\pm 5\rangle$	1.3% $\|\pm 5\rangle$	1.2% $\|\pm 5\rangle$	1.4% $\|\pm 5\rangle$	1.4% $\|\pm 5\rangle$
0.1% $\|\pm 3\rangle$	0.1% $\|\pm 3\rangle$	0.1% $\|\pm 3\rangle$	0.1% $\|\pm 3\rangle$	0.1% $\|\pm 3\rangle$	0.1% $\|\pm 3\rangle$	0.1% $\|\pm 3\rangle$	0.1% $\|\pm 3\rangle$	0.1% $\|\pm 3\rangle$	0.1% $\|\pm 3\rangle$	0.1% $\|\pm 3\rangle$	0.1% $\|\pm 3\rangle$

Table S10 The energy splitting (in cm^{-1}) of the $^5I_8$ ground multiplet of Ho^{III} centres in **3** obtained by using the large basis set (Table S6) with the enlarged active space using the RASSCF scheme consisting of three 5p orbitals with 6 electrons in RAS1, seven 4f orbitals with 10 electrons in RAS2, and five 5d orbitals in RAS3 for the dinuclear molecule along with water of crystallization (**3L-W-(active space)** model), compared with the related large basis set without the enlarged active space (**3L-W** model). Together with the energy splitting, also the g_z components of pseudo-*g*-tensors of each ground quasi non-Kramers doublets and their composition in the $|J = 8, m_J\rangle$ basis were presented.

3L-W-(active space) (large basis set with the enlarged active space (5p,4f,5d), compound **3**)		**3L-W** (large basis set, compound **3**)	
0.000		0	
0.100		**0.092**	
82.645		78.349	
84.563		79.146	
93.226		87.842	
108.649		101.597	
114.401		105.737	
137.050		127.548	
197.272		183.233	
201.738		189.143	
221.283		207.076	
250.645		232.092	
251.501		233.421	
275.920		258.603	
276.692		259.375	
299.692		279.045	
299.781		279.158	
Pseudo-*g*-tensor g_z components within basis of two lowest energy states: ($g_x = g_y = 0$ according to Griffiths Theorem)			
19.587		19.570	
Composition of two lowest energy states (I and II) in $\|m_J\rangle$ basis on the quantization axis within $J = 8$ manifold (only components with contribution above 0.09%)			
I	II	I	II
48.2% $\|\pm 8\rangle$ 1.4% $\|\pm 5\rangle$ 0.1% $\|\pm 6\rangle$	48.3% $\|\pm 8\rangle$ 1.5% $\|\pm 5\rangle$ 0.1% $\|\pm 6\rangle$	48.1% $\|\pm 8\rangle$ 1.5% $\|\pm 5\rangle$ 0.1% $\|\pm 6\rangle$	48.2% $\|\pm 8\rangle$ 1.5% $\|\pm 5\rangle$ 0.1% $\|\pm 6\rangle$

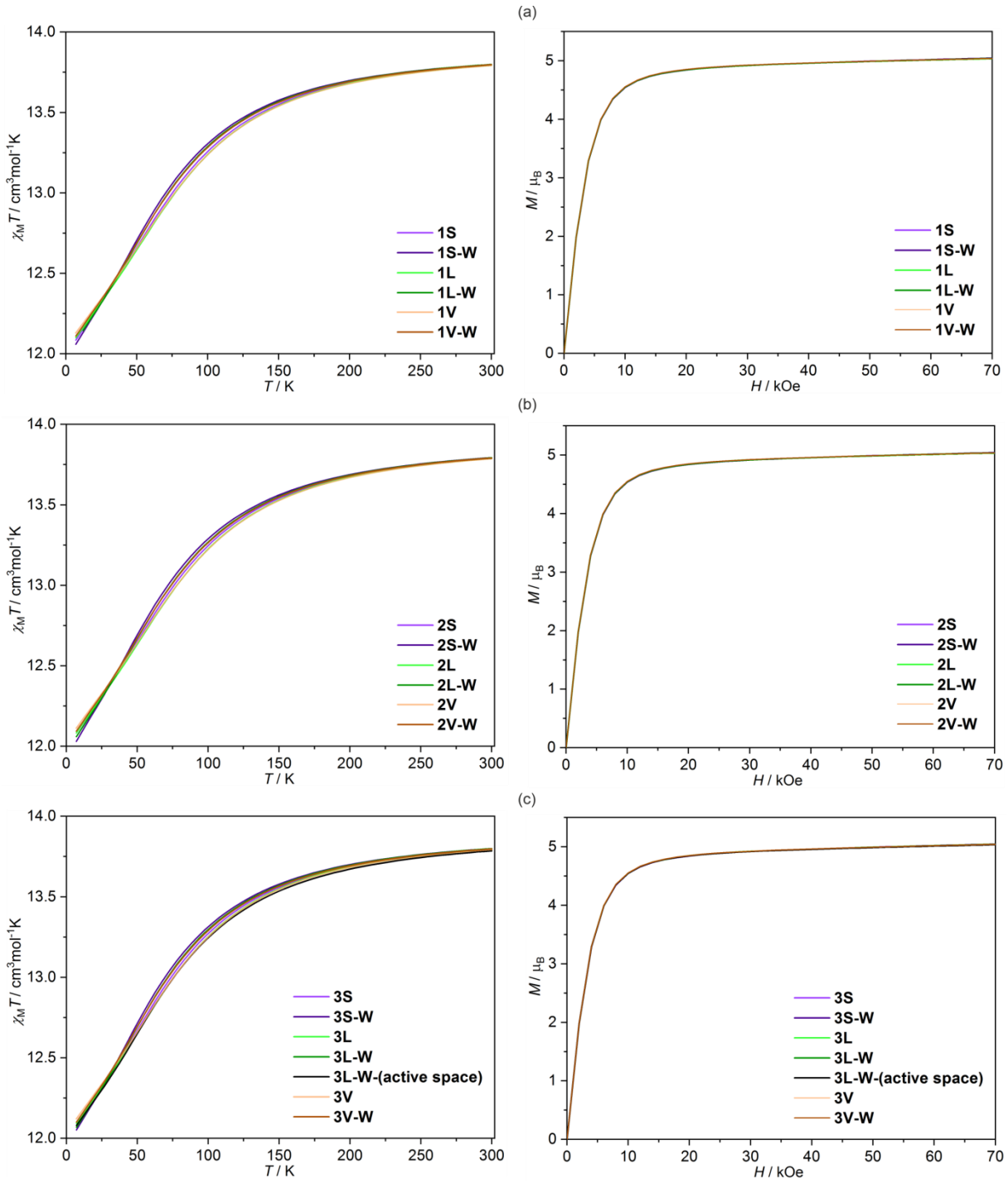

Fig. S22 The direct-current (*dc*) magnetic characteristics, including temperature dependences of the $\chi_M T$ product for H_{dc} = 1000 Oe (left panel) and field dependences of the molar magnetization for T = 1.8 K (right panel), simulated from the *ab initio* calculations of the Ho^{III} crystal field effect in **1** (*a*), **2** (*b*), and **3** (*c*), using various indicated basis sets (depicted in Table S6 and in Details of the *ab initio* calculations, see above). The comparison of the representative simulated magnetic curves obtained by using **1L-W**, **2L-W**, and **3L-W** models, for **1**, **2**, and **3**, respectively, with the experimental data was presented in Fig. S7.

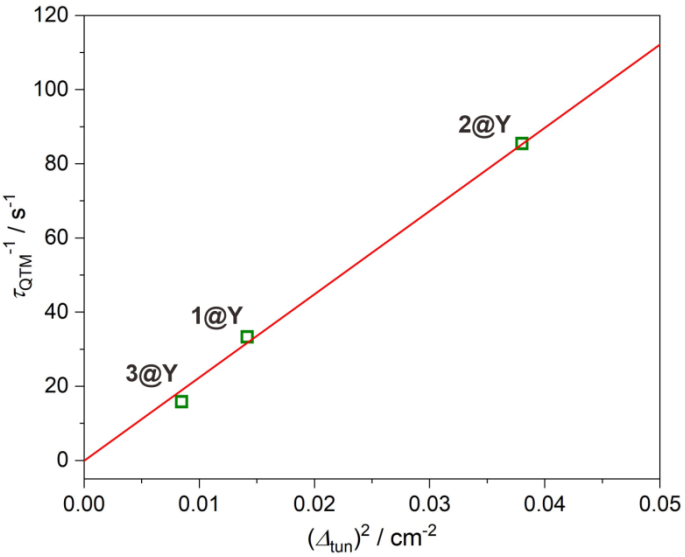

Fig. S23 The relationship between the experimental fitted rate of the quantum tunnelling of magnetization (QTM) effect, τ_{QTM}^{-1}, of **1@Y**, **2@Y**, and **3@Y** (obtained from the fitting of the temperature dependence of relaxation times, Figure 2 and Table 1), and the square of the tunnelling gaps, $(\Delta_{tun})^2$, obtained from the *ab initio* calculations of the Ho^{III} crystal field effect in **1**, **2**, and **3**. The experimental results were taken for the magnetically diluted samples of **1**–**3** (**1@Y**–**3@Y**, respectively) as the related determined rates of QTM effect represent better the isolated Ho^{III} complexes which were considered within the *ab initio* calculations. The tunnelling gaps were determined as the differences between two lowest lying m_J levels of the energy splitting of the $^5I_8$ ground multiplet of Ho^{III} centres obtained by using **1L-W**, **2L-W**, and **3L-W** models for **1**, **2**, and **3**, respectively (Table S8). The indicated relation between τ_{QTM}^{-1} and $(\Delta_{tun})^2$ was found to be linear as represented by the fitting following the equation: $\tau_{QTM}^{-1} = 2.24(6)\cdot10^{-4}\cdot(\Delta_{tun})^2$ ($R^2 = 0.9986$). The best-fit curve is presented as a red line extrapolated towards both lower and higher values of the tunnelling gap.

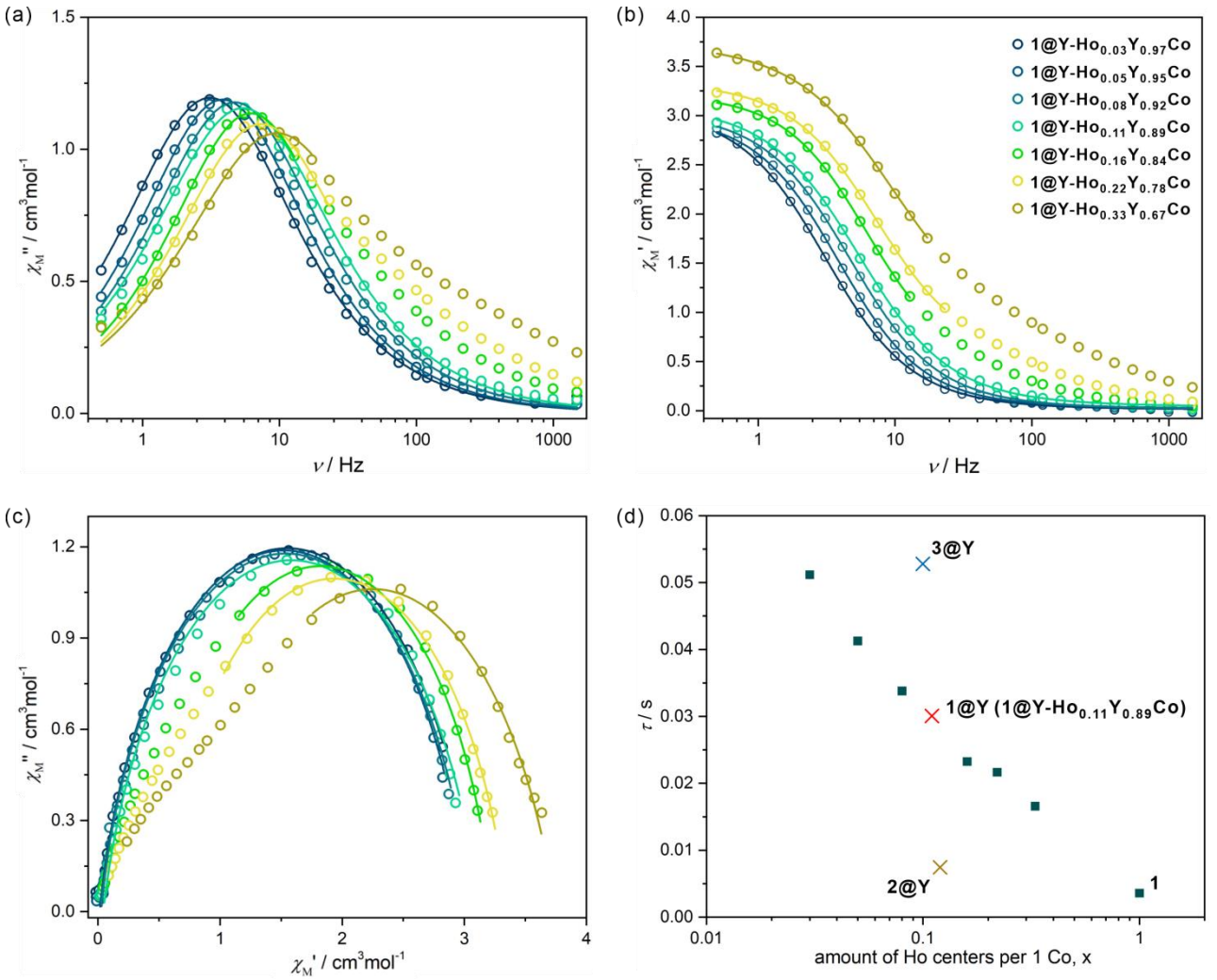

Fig. S24 Alternate-current (*ac*) magnetic characteristics of the series of magnetically diluted samples with variable Ho:Y ratio, **1@Y–Ho_xY_{1-x}Co** (x = 0.03, 0.05, 0.08, 0.11, 0.16, 0.22, 0.33), all gathered at T = 2 K and zero *dc* field. These characteristics include the frequency dependences of χ_M'' (*a*), χ_M' (*b*), the related Argand plots (*c*), and the dependence of the resulting magnetic relaxation times on the amount of Ho centres per one Co atom in the indicated series of **1@Y–Ho_xY_{1-x}Co** compounds (*d*). The *ac* magnetic curves in (*a*), (*b*), and (*c*) were fitted using the generalized Debye model for a single relaxation (the equations (e1) and (e2), see above). The best-fit curves are shown as solid lines. For comparison, in (*d*), the relaxation times determined at the identical conditions for **1@Y**, **2@Y**, and **3@Y** were also presented.

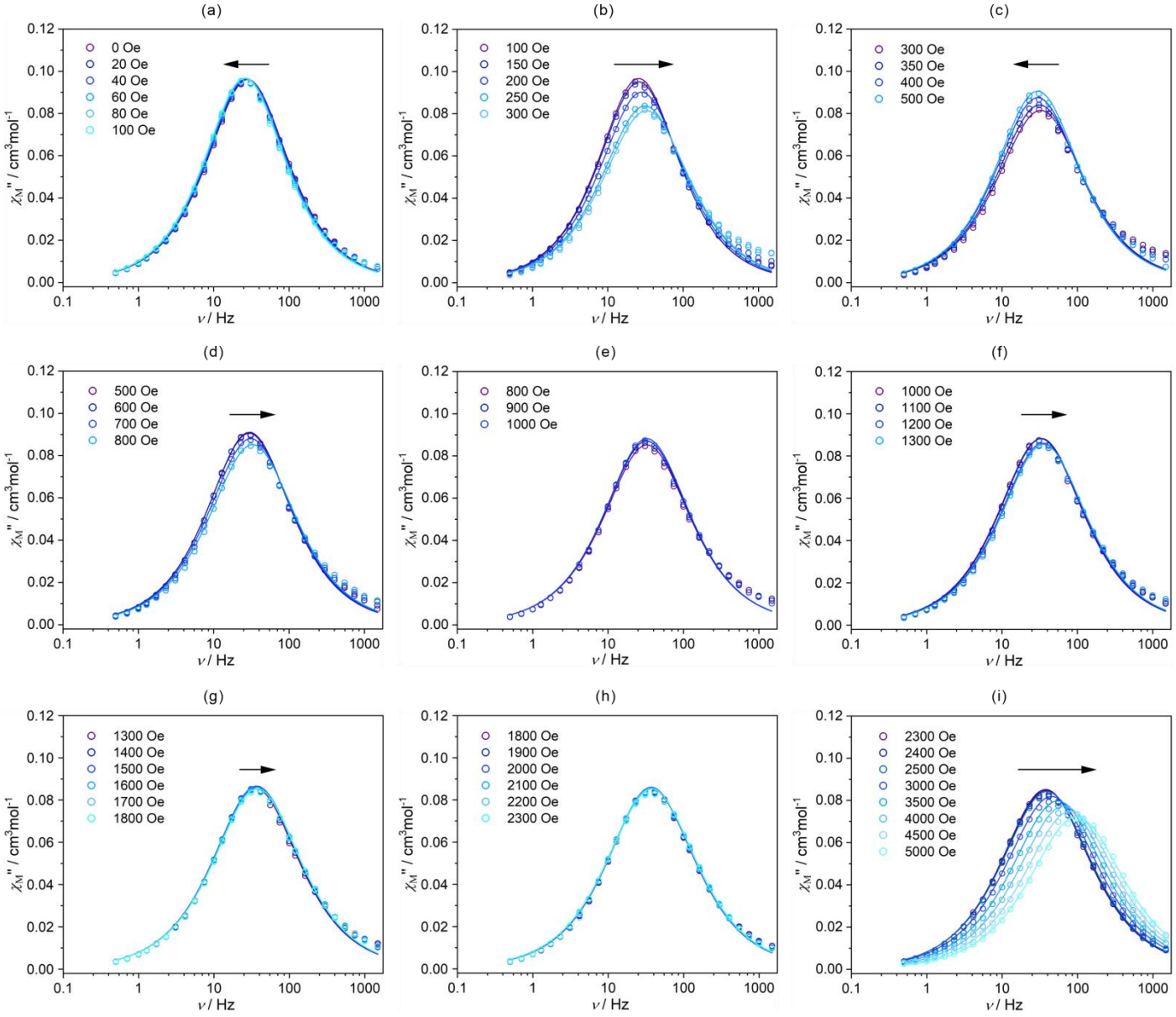

Fig. S25 Frequency dependences of the out-of-phase molar magnetic susceptibility, χ_M", of **1@Y** collected at 6 K under various indicated *dc* magnetic fields, divided into 9 ranges of 0–100 Oe (*a*), 100–300 Oe (*b*), 300–500 Oe (*c*), 500–800 Oe (*d*), 800–1000 Oe (*e*), 1000–1300 Oe (*f*), 1300–1800 Oe (*g*), 1800–2300 Oe (*h*), and 2300–5000 Oe (*i*). Black arrows indicate the shifts of the χ_M" maxima with increasing *dc* magnetic field. Solid lines represent the fitting results obtained by using a generalized Debye model (the equations (e1) and (e2), see above). The resulting field dependence of relaxation times is plotted in Fig. S28a.

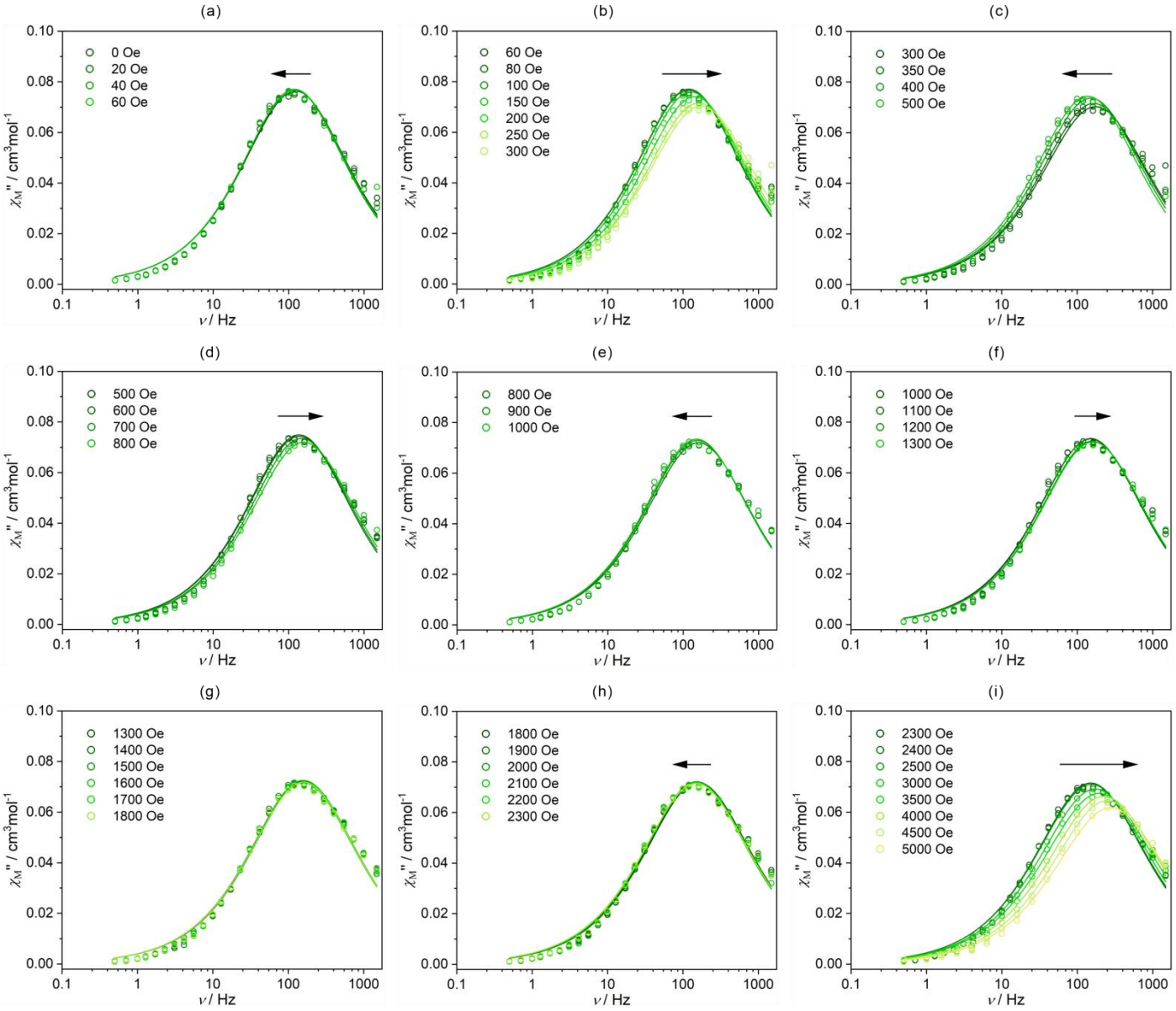

Fig. S26 Frequency dependences of the out-of-phase molar magnetic susceptibility, χ_M", of **2@Y** collected at 6 K under various indicated *dc* magnetic fields, divided into 9 ranges of 0–60 Oe (*a*), 60–300 Oe (*b*), 300–500 Oe (*c*), 500–800 Oe (*d*), 800–1000 Oe (*e*), 1000–1300 Oe (*f*), 1300–1800 Oe (*g*), 1800–2300 Oe (*h*), and 2300–5000 Oe (*i*). Black arrows indicate the shifts of the χ_M" maxima with increasing *dc* magnetic field. Solid lines represent the fitting results obtained by using a generalized Debye model (the equations (e1) and (e2), see above). The resulting field dependence of relaxation times is plotted in Fig. S28b.

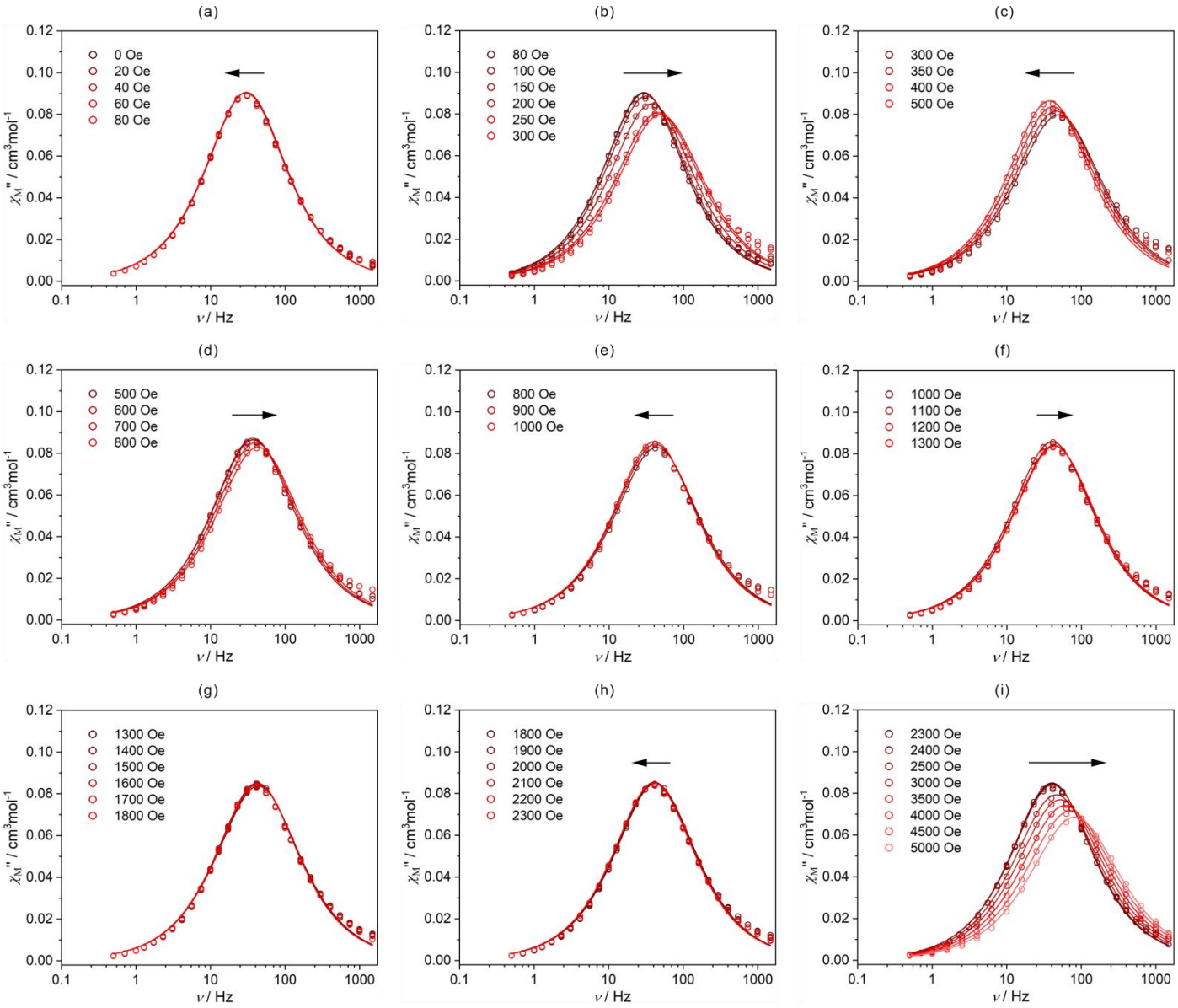

Fig. S27 Frequency dependences of the out-of-phase molar magnetic susceptibility, χ_M", of **3@Y** collected at 6 K under various indicated *dc* magnetic fields, divided into 9 ranges of 0–80 Oe (*a*), 80–300 Oe (*b*), 300–500 Oe (*c*), 500–800 Oe (*d*), 800–1000 Oe (*e*), 1000–1300 Oe (*f*), 1300–1800 Oe (*g*), 1800–2300 Oe (*h*), and 2300–5000 Oe (*i*). Black arrows indicate the shifts of the χ_M" maxima with increasing *dc* magnetic field. Solid lines represent the fitting results obtained by using a generalized Debye model (the equations (e1) and (e2), see above). The resulting field dependence of relaxation times is plotted in Fig. S28c.

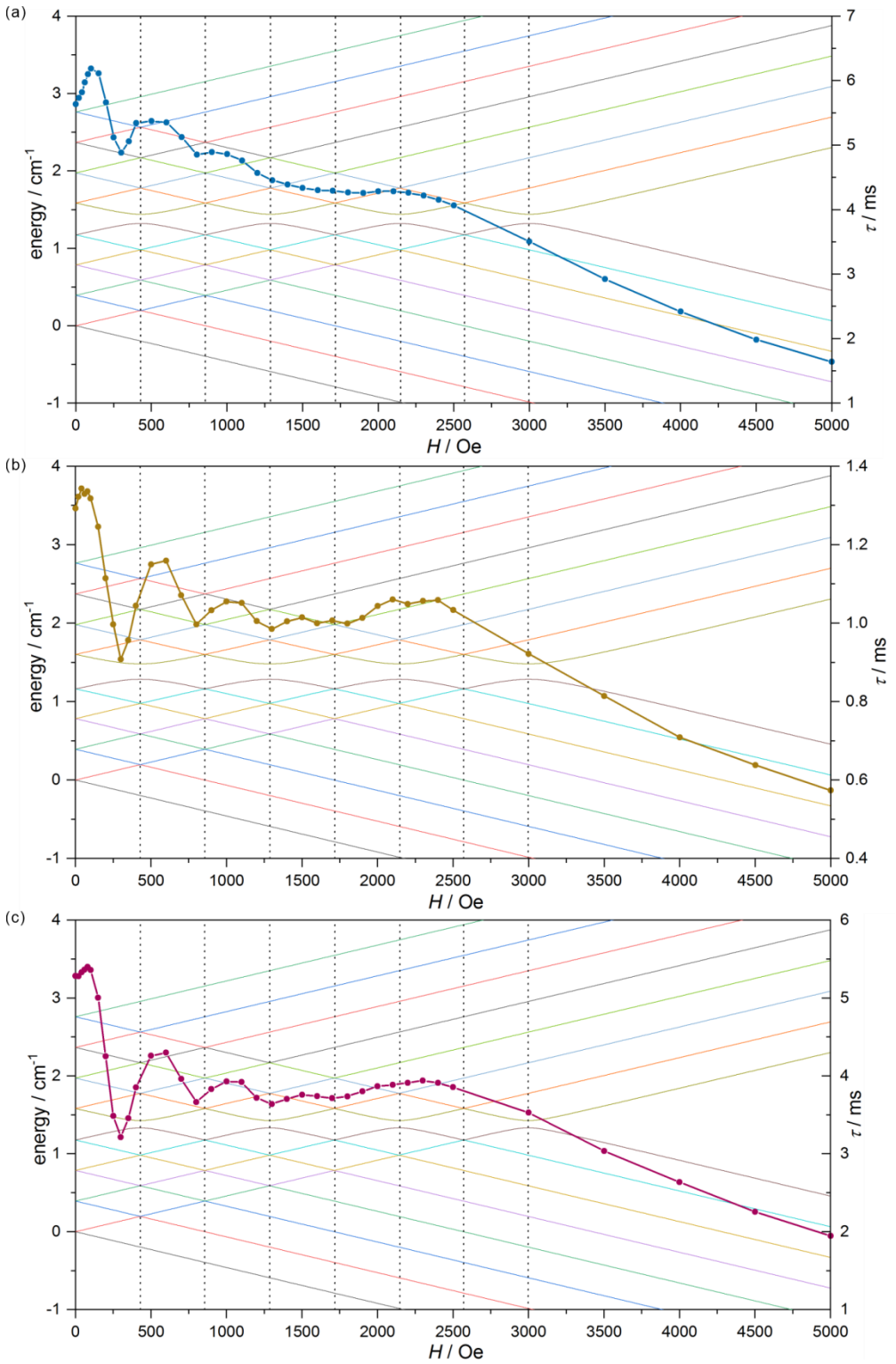

Fig. S28 Field dependences of relaxation times for **1@Y** (*a*), **2@Y** (*b*), and **3@Y** (*c*) obtained from the frequency dependences of χ_M" at T = 6 K under variable *dc* fields (Figures S25–S27) confronted with the calculated Zeeman splitting of the ground 8 hyperfine doublets (16 hyperfine states) with the hyperfine-interaction parameter, A_{hf} = 0.025 cm^{-1} (see Discussion on the hyperfine interactions below, Tables S11–S15). The experimental points are presented as coloured circles with solid lines used to guide the eye (right scale). The calculated H-dependent energies are shown as coloured lines (left scale). The vertical dashed lines represent the expected minima on the $\tau(H)$ dependences which corresponds to the points of the avoided level crossing of the presented H-dependent 16 hyperfine states. The identical oscillation effect of relaxation times under variable *dc* fields is observed for the *ac* data for T = 2 K (Fig. S14, S16, and S18). The detailed analysis is presented for T of 6 K as the full χ_M" maxima in the easily accessible 1–1000 Hz range are better detectable at this slightly elevated temperature which allows to precisely determine the relaxation times (compared with 2 K where the tails of the χ_M" peaks are lying in the very low-frequency region).

Discussion on the impact of hyperfine interactions on the electronic structure of Ho^{III} centers in 1–3

The *ab initio* calculations of the crystal field of Ho^{III} centres in **1**–**3** (presented above, Tables S6–S10) do not take into account the role of hyperfine interactions which was presented in the literature to be of great importance in the suppression of the QTM effect in Ho^{III}-based Single-Molecule Magnets.[S14] The nucleus of ^{165}Ho isotope reveals the 100% abundance and it is characterized by the nuclear spin number of $I = 7/2$. This nuclear spin is coupled through hyperfine interactions with magnetic moment of electrons related to the ground term of $J = 8$. As a result, it is expected to observe the energy splitting into 136 states (coming from the calculation of $(2J + 1)\times(2I + 1)$) where 16 states ($2\times(2I + 1)$) should originate from the ground quasi doublet. Thanks to the inclusion of the half-integer nuclear spin number, the total angular momentum of the system, F becomes a half-integer, as $F = I + J$. This allows us to treat the investigated Ho^{III} complexes as Kramers systems which obey the Kramers degeneracy theorem. Thus, the following Hamiltonian (equation (e3)) can be used for the treatment of the ground electronic $J = 8$ manifold of Ho^{III} centres with the nuclear spin of $I = 7/2$:

$$\widehat{H} = \sum_k \sum_{q=-k}^{k} B_k^q O_k^q(J) + A_{hf} J \cdot I - g_J \frac{\mu_B}{\hbar} H_z J - g_{eff} \frac{\mu_B}{\hbar} H_z I \qquad \text{(e3)}$$

where the first term represents the crystal field effect with the operator equivalents, $O_k^q(J)$ and the crystal field parameters (CFPs), B_k^q,[S15] the second term represents the hyperfine interactions with the hyperfine-interaction parameter, A_{hf}, while the last two terms represent the first order Zeeman interaction of the electronic magnetic moment (third term) and the nuclear spin (the fourth term) with the magnetic field component, H_z arbitrarily applied along the quantization axis of the ground manifold. Within this Hamiltonian equation, operator equivalents, $O_k^q(J)$ are the functions of J_z, J_x, and J_z, the effective g-factor for the ^{165}Ho nucleus, g_{eff} is equal to $-9.08421139832151\cdot10^{-4}$, all taken from the related PHI software,[S16] while the g_J Lande factor was calculated for the ground $^5I_8$ term of Ho^{III}. The crystal field parameters, B_k^q, limited to the 6th order, were calculated for Ho^{III} complexes in **1**–**3** from the respective results of the *ab initio* calculations performed within the large basis sets (**1L-W**, **2L-W**, and **3L-W** models for **1**, **2**, **3**, respectively, Table S8). The resulting B_k^q parameters were collected in Table S11.

To determine the value of the hyperfine-interaction parameter, A_{hf}, the field-dependent *ac* magnetic characteristics of the magnetically diluted samples of **1**–**3**, named **1@Y**–**3@Y**, respectively, were collected (Fig. S25–S27). They were used for the determination of the field-dependent magnetic relaxation times (Fig. S28). Then, the Hamiltionian equation (e3) was diagonalized for various values of A_{hf} (starting from the typical values of hyperfine-interaction parameters from ref. S14) under the magnetic field range of 0–0.25 T (0–2500 Oe) which gave the hyperfine splitting and the Zeeman splitting of resulting states. After that, the A_{hf} parameter was adjusted in the way that the minima on the experimental field dependences of relaxation time coincide with the points related to the avoided level crossing of 16 ground hyperfine states coming from the former ground doublet of Ho^{III}. The optimal A_{hf} of 0.025 cm^{-1} was found to be identical in the whole series of **1**–**3**, and it resulted in the very good matching between the points of avoided level crossing and the real minima on the $\tau(H)$ curves (Fig. S28). Such an approach is related to the variable strength of the QTM effect. It is expected to be the strongest at magnetic fields where the avoiding level crossing between hyperfine states occurs which originates from the strong mixing of components in the ground F manifold.

The obtained optimal value of A_{hf} was, then, used for the determination of the compositions of 16 lowest lying ground Kramers doublets of Ho^{III} complexes related to the splitting of the ground electronic doublet (8 states) and the first excited one (8 states). They are presented in the uncoupled $|J = 8, I = {}^7/_2, m_J, m_I\rangle$ basis in Tables S12, S13, and S14, for **1**, **2**, and **3**, respectively. From these results, it is seen that the first multiplet comprising of 8 doublets is characterized by almost pure states which is in contrast to higher-lying strongly mixed states. This observation was further rationalized by the computing of the pseudo-g-tensor components for each doublet which are gathered in Table S15. Very axial states, revealing negligibly small values of transversal g_x and g_y components of pseudo-g-tensors, are

obtained within all 8 lowest lying doublets in all compounds, **1**–**3**, which is the reason of the efficient suppression of the QTM effect, and the observation of zero *dc* field SMM behaviour in the whole series of molecular systems. Moreover, the smallest transversal components of pseudo-*g*-tensors within the ground manifold are detected in **3** when the biggest in **2** which stays in a perfect agreement with the experimental rates of QTM effects, the fastest in **2**, and the slowest (i.e. the most efficiently suppressed) in **3** (Fig. 1 and Table 1). The doublets of the excited multiplet were found to be strongly mixed in **1**–**3** confirming the occurrence of Orbach relaxation process through these states (Fig. 3). The related energy barriers, determined within this approximation, are ca. 89.7, 86.8, and 79.2 cm^{-1} for **1**, **2**, and **3**, which is also in a perfect agreement with the experimental observations (Table 1).

(S14) Y.-C. Chen, J.-L. Liu, W. Wernsdorfer, D. Liu, L. F. Chibotaru, X.-M. Chen and M.-L. Tong, *Angew. Chem. Int. Ed*., 2017, **56**, 4996–5000.

(S15) C. Rudowicz, *J. Phys. C Solid State Phys*., 1985, **18**, 1415–1430.

(S16) N. F. Chilton, R. P. Anderson, L. D. Turner, A. Soncini and K. S. Murray, *J. Comput. Chem*., 2013, **34**, 1164–1175.

Table S11 The crystal-field parameters, B_k^q, limited to the 6th order, of Ho^{III} complexes in **1**–**3** obtained from the *ab initio* calculations by using the large basis sets (Table S8).

B_k^q		value of B_q^k for compound **1** (model **1L-W**, Table S8) / cm^{-1}	value of B_q^k for compound **2** (model **3L-W**, Table S8) / cm^{-1}	value of B_q^k for compound **3** (model **3L-W**, Table S8) / cm^{-1}
k	***q***			
2	-2	1.847386E-01	6.614071E-02	9.188446E-02
2	-1	-8.621350E-02	-1.350117E-01	2.062324E-01
2	0	-5.908859E-02	-3.480408E-02	-1.243659E-02
2	1	5.121223E-02	5.246622E-02	-1.220251E-01
2	2	1.001020E-01	7.222161E-02	5.045676E-02
4	-4	-1.600996E-03	-2.582248E-03	-2.105705E-03
4	-3	8.044071E-04	-9.286957E-03	-6.613456E-04
4	-2	-2.628605E-03	-1.910919E-03	-2.399511E-03
4	-1	1.429683E-03	2.442755E-03	-2.686954E-03
4	0	-4.972253E-03	-4.989899E-03	-4.923449E-03
4	1	-8.517028E-04	-9.502886E-04	1.590913E-03
4	2	-1.421527E-03	-2.083919E-03	-1.315255E-03
4	3	2.010261E-02	1.883344E-02	-2.039145E-02
4	4	1.044315E-03	-2.260529E-04	1.340517E-03
6	-6	-8.089331E-06	9.994947E-05	-5.144281E-06
6	-5	1.300026E-04	5.840801E-05	-1.780886E-04
6	-4	2.769279E-05	3.418496E-05	3.344565E-05
6	-3	-1.562594E-05	1.737224E-04	1.264224E-05
6	-2	-1.897421E-05	-2.342484E-06	-6.367764E-06
6	-1	-6.304817E-05	-7.075040E-05	6.885628E-05
6	0	-2.880400E-05	-3.044119E-05	-2.956827E-05
6	1	3.756964E-05	2.752664E-05	-4.077334E-05
6	2	-1.025730E-05	-2.544116E-06	-3.481038E-06
6	3	-3.773135E-04	-3.527383E-04	3.808476E-04
6	4	-1.809412E-05	2.974743E-06	-2.132768E-05
6	5	6.360314E-05	1.997990E-04	-9.011584E-05
6	6	-9.845079E-05	-7.676362E-05	-7.827504E-05

Table S12 The energy splitting of ground 16 hyperfine Kramers doublets of **1** obtained from the diagonalization of the Hamiltonian equation (e3) using the hyperfine-interaction parameter, A_{hf} of 0.025 cm^{-1}, and their percentage composition given in the uncoupled $|J = 8, I = {}^{7}/_{2}, m_J, m_I\rangle$ basis.

compound **1**	
energy / cm^{-1}	percentage composition of three main components in the $\|m_J, m_I\rangle$ uncoupled basis / %
0.000	96.34 |-8.0,-3.5> + 2.91 |-5.0,-3.5> + 0.27 |-6.0,-3.5>
0.000	96.34 |8.0,3.5> + 2.91 |5.0,3.5> + 0.27 |6.0,3.5>
0.393	96.29 |-8.0,-2.5> + 2.91 |-5.0,-2.5> + 0.27 |-6.0,-2.5>
0.393	96.29 |8.0,2.5> + 2.91 |5.0,2.5> + 0.27 |6.0,2.5>
0.786	96.12 |-8.0,-1.5> + 2.91 |-5.0,-1.5> + 0.27 |-6.0,-1.5>
0.786	96.12 |8.0,1.5> + 2.91 |5.0,1.5> + 0.27 |6.0,1.5>
1.175	94.08 |-8.0,-0.5> + 2.85 |-5.0,-0.5> + 2.05 |8.0,-0.5>
1.175	94.08 |8.0,0.5> + 2.85 |5.0,0.5> + 2.05 |-8.0,0.5>
1.587	67.82 |-8.0,0.5> + 26.48 |8.0,-0.5> + 2.06 |-5.0,0.5>
1.587	67.82 |8.0,-0.5> + 26.48 |-8.0,0.5> + 2.06 |5.0,-0.5>
1.975	96.11 |-8.0,1.5> + 2.92 |-5.0,1.5> + 0.27 |-6.0,1.5>
1.975	96.11 |8.0,-1.5> + 2.92 |5.0,-1.5> + 0.27 |6.0,-1.5>
2.368	96.26 |8.0,-2.5> + 2.93 |5.0,-2.5> + 0.27 |6.0,-2.5>
2.368	96.26 |-8.0,2.5> + 2.93 |-5.0,2.5> + 0.27 |-6.0,2.5>
2.762	96.29 |8.0,-3.5> + 2.94 |5.0,-3.5> + 0.27 |6.0,-3.5>
2.762	96.29 |-8.0,3.5> + 2.94 |-5.0,3.5> + 0.27 |-6.0,3.5>
89.734	11.04 |0.0,0.5> + 7.00 |0.0,-1.5> + 5.80 |0.0,-0.5>
89.734	11.04 |0.0,-0.5> + 7.00 |0.0,1.5> + 5.80 |0.0,0.5>
89.943	10.98 |0.0,-1.5> + 7.96 |0.0,2.5> + 5.23 |2.0,-1.5>
89.943	10.98 |0.0,1.5> + 7.96 |0.0,-2.5> + 5.23 |-2.0,1.5>
90.100	13.20 |0.0,2.5> + 6.76 |2.0,2.5> + 6.40 |-2.0,2.5>
90.100	13.20 |0.0,-2.5> + 6.76 |-2.0,-2.5> + 6.40 |2.0,-2.5>
90.200	26.37 |0.0,-3.5> + 13.49 |-2.0,-3.5> + 13.08 |2.0,-3.5>
90.200	26.37 |0.0,3.5> + 13.49 |2.0,3.5> + 13.08 |-2.0,3.5>
92.463	18.07 |1.0,3.5> + 16.23 |-1.0,3.5> + 6.80 |3.0,3.5>
92.463	18.07 |-1.0,-3.5> + 16.23 |1.0,-3.5> + 6.80 |-3.0,-3.5>
92.556	12.41 |1.0,2.5> + 11.33 |-1.0,2.5> + 8.50 |-1.0,-3.5>
92.556	12.41 |-1.0,-2.5> + 11.33 |1.0,-2.5> + 8.50 |1.0,3.5>
92.723	11.63 |-1.0,1.5> + 11.49 |-1.0,-2.5> + 9.97 |1.0,1.5>
92.723	11.63 |1.0,-1.5> + 11.49 |1.0,2.5> + 9.97 |-1.0,-1.5>
92.946	14.56 |-1.0,-0.5> + 10.96 |1.0,-0.5> + 7.57 |-1.0,1.5>
92.946	14.56 |1.0,0.5> + 10.96 |-1.0,0.5> + 7.57 |1.0,-1.5>

Table S13 The energy splitting of ground 16 hyperfine Kramers doublets of **2** obtained from the diagonalization of the Hamiltonian equation (e3) using the hyperfine-interaction parameter, A_{hf} of 0.025 cm^{-1}, and their percentage composition given in the uncoupled $|J = 8, I = {}^{7}/_{2}, m_J, m_I\rangle$ basis.

compound **2**	
energy / cm^{-1}	percentage composition of three main components in the $\|m_J, m_I\rangle$ uncoupled basis / %
0.000	96.20 |8.0,3.5> + 3.12 |5.0,3.5> + 0.14 |3.0,3.5>
0.000	96.20 |-8.0,-3.5> + 3.12 |-5.0,-3.5> + 0.14 |-3.0,-3.5>
0.392	96.08 |8.0,2.5> + 3.12 |5.0,2.5> + 0.23 |-8.0,2.5>
0.392	96.08 |-8.0,-2.5> + 3.12 |-5.0,-2.5> + 0.23 |8.0,-2.5>
0.783	95.65 |-8.0,-1.5> + 3.11 |-5.0,-1.5> + 0.64 |8.0,-1.5>
0.783	95.65 |8.0,1.5> + 3.11 |5.0,1.5> + 0.64 |-8.0,1.5>
1.162	82.81 |-8.0,-0.5> + 8.41 |8.0,0.5> + 4.57 |8.0,-0.5>
1.162	82.81 |8.0,0.5> + 8.41 |-8.0,-0.5> + 4.57 |-8.0,0.5>
1.602	90.87 |8.0,-0.5> + 5.05 |-8.0,-0.5> + 2.96 |5.0,-0.5>
1.602	90.87 |-8.0,0.5> + 5.05 |8.0,0.5> + 2.96 |-5.0,0.5>
1.981	95.65 |-8.0,1.5> + 3.13 |-5.0,1.5> + 0.66 |8.0,1.5>
1.981	95.65 |8.0,-1.5> + 3.13 |5.0,-1.5> + 0.66 |-8.0,-1.5>
2.372	94.30 |-8.0,2.5> + 3.09 |-5.0,2.5> + 1.76 |8.0,-2.5>
2.372	94.30 |8.0,-2.5> + 3.09 |5.0,-2.5> + 1.76 |-8.0,2.5>
2.765	96.15 |8.0,-3.5> + 3.15 |5.0,-3.5> + 0.14 |3.0,-3.5>
2.765	96.15 |-8.0,3.5> + 3.15 |-5.0,3.5> + 0.14 |-3.0,3.5>
86.854	15.08 |-2.0,-0.5> + 14.94 |2.0,-0.5> + 8.08 |1.0,-0.5>
86.854	15.08 |2.0,0.5> + 14.94 |-2.0,0.5> + 8.08 |-1.0,0.5>
86.976	15.51 |-2.0,-1.5> + 15.02 |2.0,-1.5> + 8.71 |-1.0,-1.5>
86.976	15.51 |2.0,1.5> + 15.02 |-2.0,1.5> + 8.71 |1.0,1.5>
87.067	18.27 |2.0,2.5> + 17.44 |-2.0,2.5> + 10.48 |1.0,2.5>
87.067	18.27 |-2.0,-2.5> + 17.44 |2.0,-2.5> + 10.48 |-1.0,-2.5>
87.193	24.73 |-2.0,-3.5> + 23.51 |2.0,-3.5> + 13.85 |-1.0,-3.5>
87.193	24.73 |2.0,3.5> + 23.51 |-2.0,3.5> + 13.85 |1.0,3.5>
89.199	16.12 |0.0,-3.5> + 11.03 |-3.0,-3.5> + 8.64 |3.0,-3.5>
89.199	16.12 |0.0,3.5> + 11.03 |3.0,3.5> + 8.64 |-3.0,3.5>
89.266	12.08 |0.0,-2.5> + 7.60 |0.0,-0.5> + 7.59 |0.0,3.5>
89.266	12.08 |0.0,2.5> + 7.60 |0.0,0.5> + 7.59 |0.0,-3.5>
89.391	12.97 |0.0,-1.5> + 12.36 |0.0,2.5> + 8.40 |3.0,2.5>
89.391	12.97 |0.0,1.5> + 12.36 |0.0,-2.5> + 8.40 |-3.0,-2.5>
89.568	13.84 |0.0,0.5> + 9.28 |3.0,0.5> + 8.60 |0.0,-1.5>
89.568	13.84 |0.0,-0.5> + 9.28 |-3.0,-0.5> + 8.60 |0.0,1.5>

Table S14 The energy splitting of ground 16 hyperfine Kramers doublets of **3** obtained from the diagonalization of the Hamiltonian equation (e3) using the hyperfine-interaction parameter, A_{hf} of 0.025 cm^{-1}, and their percentage composition given in the uncoupled $|J = 8, I = {}^{7}/_{2}, m_J, m_I\rangle$ basis.

compound **3**	
energy / cm^{-1}	percentage composition of three main components in the $\|m_J, m_I\rangle$ uncoupled basis / %
0.000	96.29 |-8.0,-3.5> + 3.10 |-5.0,-3.5> + 0.15 |-6.0,-3.5>
0.000	96.29 |8.0,3.5> + 3.10 |5.0,3.5> + 0.15 |6.0,3.5>
0.393	96.26 |-8.0,-2.5> + 3.10 |-5.0,-2.5> + 0.15 |-6.0,-2.5>
0.393	96.26 |8.0,2.5> + 3.10 |5.0,2.5> + 0.15 |6.0,2.5>
0.787	96.15 |-8.0,-1.5> + 3.10 |-5.0,-1.5> + 0.15 |-6.0,-1.5>
0.787	96.15 |8.0,1.5> + 3.10 |5.0,1.5> + 0.15 |6.0,1.5>
1.177	95.00 |8.0,0.5> + 3.07 |5.0,0.5> + 1.27 |-8.0,0.5>
1.177	95.00 |-8.0,-0.5> + 3.07 |-5.0,-0.5> + 1.27 |8.0,-0.5>
1.582	73.89 |-8.0,0.5> + 21.14 |8.0,-0.5> + 2.39 |-5.0,0.5>
1.582	73.89 |8.0,-0.5> + 21.14 |-8.0,0.5> + 2.39 |5.0,-0.5>
1.972	96.12 |8.0,-1.5> + 3.12 |5.0,-1.5> + 0.15 |6.0,-1.5>
1.972	96.12 |-8.0,1.5> + 3.12 |-5.0,1.5> + 0.15 |-6.0,1.5>
2.366	96.08 |-8.0,2.5> + 3.12 |-5.0,2.5> + 0.15 |-6.0,2.5>
2.366	96.08 |8.0,-2.5> + 3.12 |5.0,-2.5> + 0.15 |6.0,-2.5>
2.760	79.03 |8.0,-3.5> + 17.21 |-8.0,3.5> + 2.57 |5.0,-3.5>
2.760	79.03 |-8.0,3.5> + 17.21 |8.0,-3.5> + 2.57 |-5.0,3.5>
79.219	8.19 |-2.0,-0.5> + 8.15 |0.0,0.5> + 8.11 |2.0,-0.5>
79.219	8.19 |2.0,0.5> + 8.15 |0.0,-0.5> + 8.11 |-2.0,0.5>
79.471	6.69 |-2.0,-1.5> + 6.59 |2.0,-1.5> + 6.03 |-1.0,-1.5>
79.471	6.69 |2.0,1.5> + 6.59 |-2.0,1.5> + 6.03 |1.0,1.5>
79.694	7.42 |-2.0,-2.5> + 7.24 |-1.0,-2.5> + 7.21 |2.0,-2.5>
79.694	7.42 |2.0,2.5> + 7.24 |1.0,2.5> + 7.21 |-2.0,2.5>
79.852	11.53 |-1.0,-3.5> + 10.88 |1.0,-3.5> + 10.49 |-2.0,-3.5>
79.852	11.53 |1.0,3.5> + 10.88 |-1.0,3.5> + 10.49 |2.0,3.5>
80.822	11.35 |0.0,3.5> + 9.89 |3.0,3.5> + 8.72 |-3.0,3.5>
80.822	11.35 |0.0,-3.5> + 9.89 |-3.0,-3.5> + 8.72 |3.0,-3.5>
80.982	7.28 |0.0,-2.5> + 5.88 |2.0,2.5> + 5.58 |-2.0,2.5>
80.982	7.28 |0.0,2.5> + 5.88 |-2.0,-2.5> + 5.58 |2.0,-2.5>
81.221	8.96 |0.0,1.5> + 8.35 |0.0,-2.5> + 5.64 |-2.0,-1.5>
81.221	8.96 |0.0,-1.5> + 8.35 |0.0,2.5> + 5.64 |2.0,1.5>
81.495	11.65 |0.0,-0.5> + 7.80 |2.0,0.5> + 7.76 |-2.0,0.5>
81.495	11.65 |0.0,0.5> + 7.80 |-2.0,-0.5> + 7.76 |2.0,-0.5>

Table S15 The pseudo-*g*-tensor components (g_x, g_y, g_z) for 16 lowest-lying Kramers doublets arising from the hyperfine splitting of the ground and the first excited states of **1**–**3** obtained using crystal-field parameters within the J = 8 manifold from the *ab initio* calculations (**1L-W**, **2L-W**, and **3L-W** models for **1**, **2**, and **3**, respectively, Table S8) and hyperfine interactions depicted by the A_{hf} parameter of 0.025 cm^{-1}.

energy / cm^{-1}	compound **1**			energy / cm^{-1}	compound **2**			energy / cm^{-1}	compound **3**		
	g_x	g_y	g_z		g_x	g_y	g_z		g_x	g_y	g_z
0.000	0.0000	0.0000	19.6924	0.000	0.0000	0.0000	19.6471	0.000	0.0000	0.0000	19.6903
0.393	0.0000	0.0000	19.6758	0.392	0.0000	0.0000	19.6008	0.393	0.0000	0.0000	19.6808
0.786	0.0000	0.0000	19.6132	0.783	0.0000	0.0000	19.4329	0.787	0.0000	0.0000	19.6436
1.175	0.0021	0.0027	18.8670	1.162	0.0031	0.0044	17.6348	1.177	0.0016	0.0022	19.1844
1.587	0.0012	0.0028	18.8681	1.602	0.0020	0.0042	17.6357	1.582	0.0009	0.0024	19.1855
1.975	0.0000	0.0000	19.6165	1.981	0.0000	0.0000	19.4358	1.972	0.0000	0.0000	19.6467
2.368	0.0000	0.0000	19.6812	2.372	0.0000	0.0000	19.6057	2.366	0.0000	0.0000	19.6860
2.762	0.0000	0.0000	19.7000	2.765	0.0000	0.0000	19.6540	2.760	0.0000	0.0000	19.6977
89.734	0.0000	0.0003	12.4068	86.854	0.0012	0.0636	9.7196	79.219	0.0000	0.0001	13.9341
89.943	0.0014	0.0289	10.1340	86.976	0.0216	1.1370	6.8429	79.471	0.0006	0.0126	12.8630
90.100	0.0243	0.5535	6.3936	87.067	0.0710	1.7142	2.7522	79.694	0.0158	0.3392	10.1900
90.200	0.0769	0.7047	2.0159	87.193	0.1191	0.1863	0.2755	79.852	0.0729	0.9837	4.3271
92.463	0.0845	0.1953	2.3526	89.199	0.1017	0.4731	1.5845	80.822	0.0005	0.4778	4.5050
92.556	0.0112	0.0164	6.5547	89.266	0.0027	0.1075	4.5705	80.982	0.0030	0.0643	10.2732
92.723	0.0001	0.0003	9.6468	89.391	0.0011	0.0135	7.0098	81.221	0.0000	0.0025	12.6034
92.946	0.0000	0.0000	11.6870	89.568	0.0001	0.0007	8.8119	81.495	0.0000	0.0000	13.5492

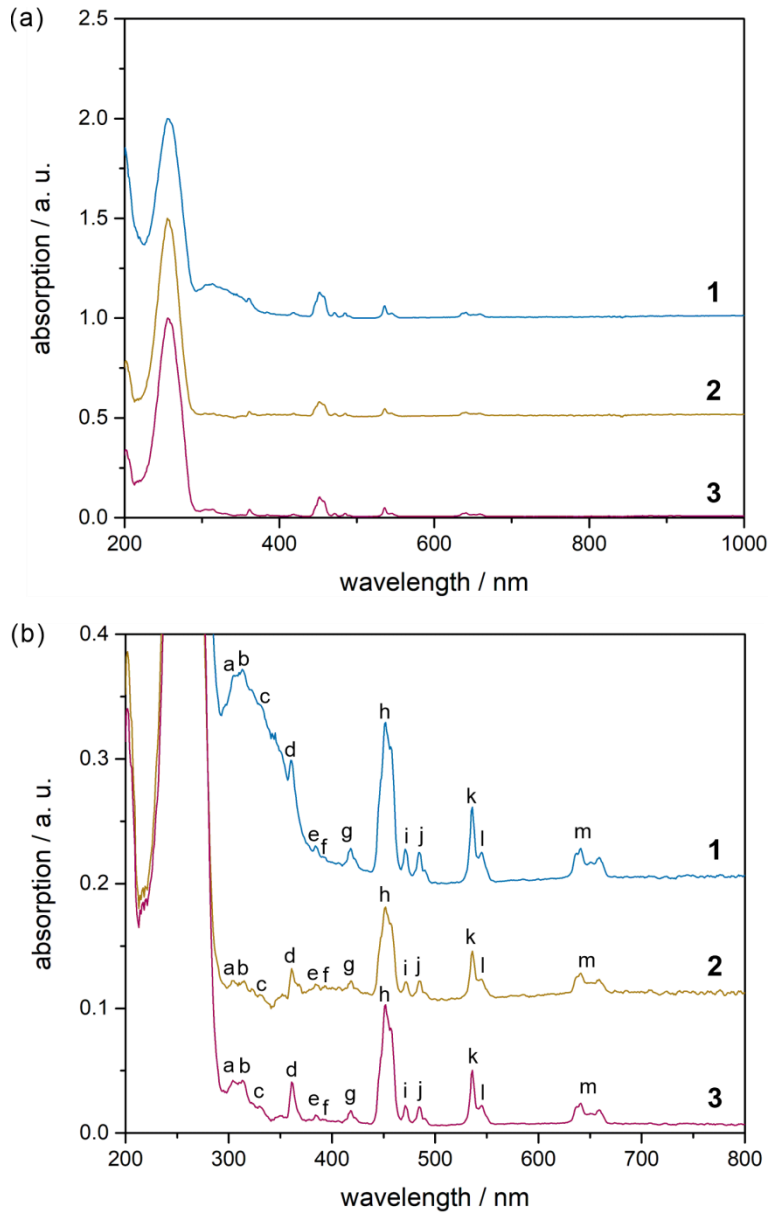

Fig. S29 Solid-state UV-vis-NIR absorption spectra of **1**–**3** collected in the 200–1000 nm wavelength range (*a*), and the enlargement of weak absorption peaks (labelled from ***a*** to ***m***) in the 200–800 nm region involving f-f electronic transitions of Ho^{III} centres (*b*). The detailed assignment of the ***a***-to-***m*** absorption peaks to f-f electronic transitions is listed in Table S16.

Table S16 The assignment of the UV-vis absorption peaks (Fig. S29) to the f-f electronic transitions of Ho^{III} centres in compounds **1**–**3**.[S17–S19]

peak	λ / nm	wavenumber / cm^{-1}	f-f electronic transition
a	304	32895	$^5I_8 \rightarrow {}^3D_3$
	314	31847	
b	323	30960	$^5I_8 \rightarrow {}^5G_2$
c	331	30211	$^5I_8 \rightarrow {}^3F_4 + {}^3K_6$
d	361	27701	$^5I_8 \rightarrow {}^5G_5 + {}^3H_6$
e	384	26042	$^5I_8 \rightarrow {}^3K_7$
f	392	25510	$^5I_8 \rightarrow {}^5G_4$
g	418	23923	$^5I_8 \rightarrow {}^5G_5$
	423	23641	
h	447	22371	$^5I_8 \rightarrow {}^5F_1 + {}^5G_6$
	452	22124	
	457	21882	
i	471	21231	$^5I_8 \rightarrow {}^5F_2 + {}^3K_8$
j	485	20619	$^5I_8 \rightarrow {}^5F_3$
	490	20408	
k	536	18657	$^5I_8 \rightarrow {}^5F_4$
l	545	18349	$^5I_8 \rightarrow {}^5S_2$
m	636	15723	$^5I_8 \rightarrow {}^5F_5$
	641	15601	
	651	15361	
	659	15175	
	663	15083	

(S17) J. B. Gruber, G. W. Burdick, U. V. Valiev, K. L. Nash, S. A. Rakhimov and D. K. Sardar, *J. Appl. Phys.*, 2009, **106**, 113110.

(S18) J. B. Gruber, M. D. Seltzer, V. J. Pugh and F. S. Richardson, *J. Appl. Phys.*, 1995, **77**, 5882.

(S19) D. M. Moran, A. D. Piante and F. S. Richardson, *Phys. Rev. B*, 1990, **42**, 3317–3330.

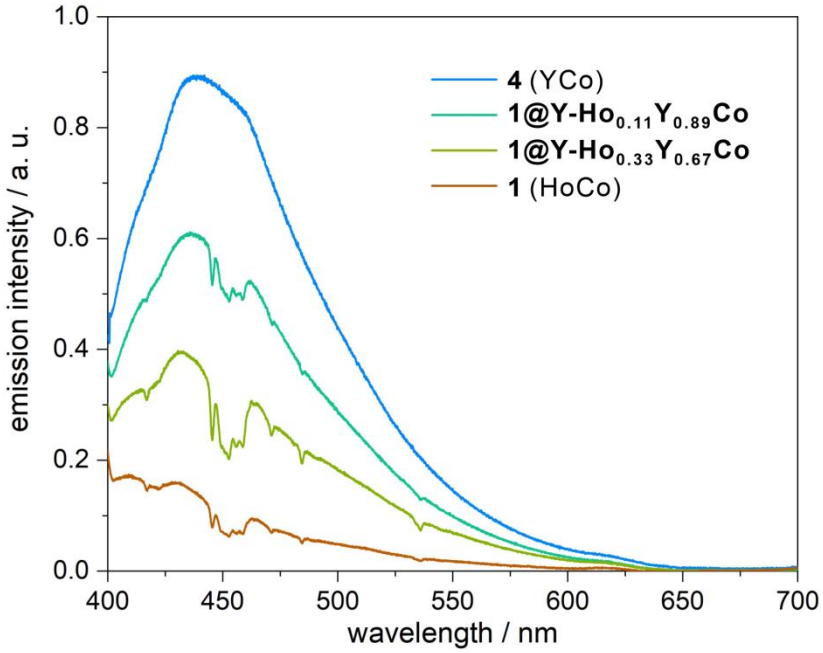

Fig. S30 Room temperature solid-state emission spectra of bimetallic compounds **1** and **4**, and their trimetallic analogues of **1@Y–$Ho_{0.11}Y_{0.89}Co$** (also named **1@Y**) and **1@Y–$Ho_{0.33}Y_{0.67}Co$**. The emission spectra were collected under the 370 nm excitation light.

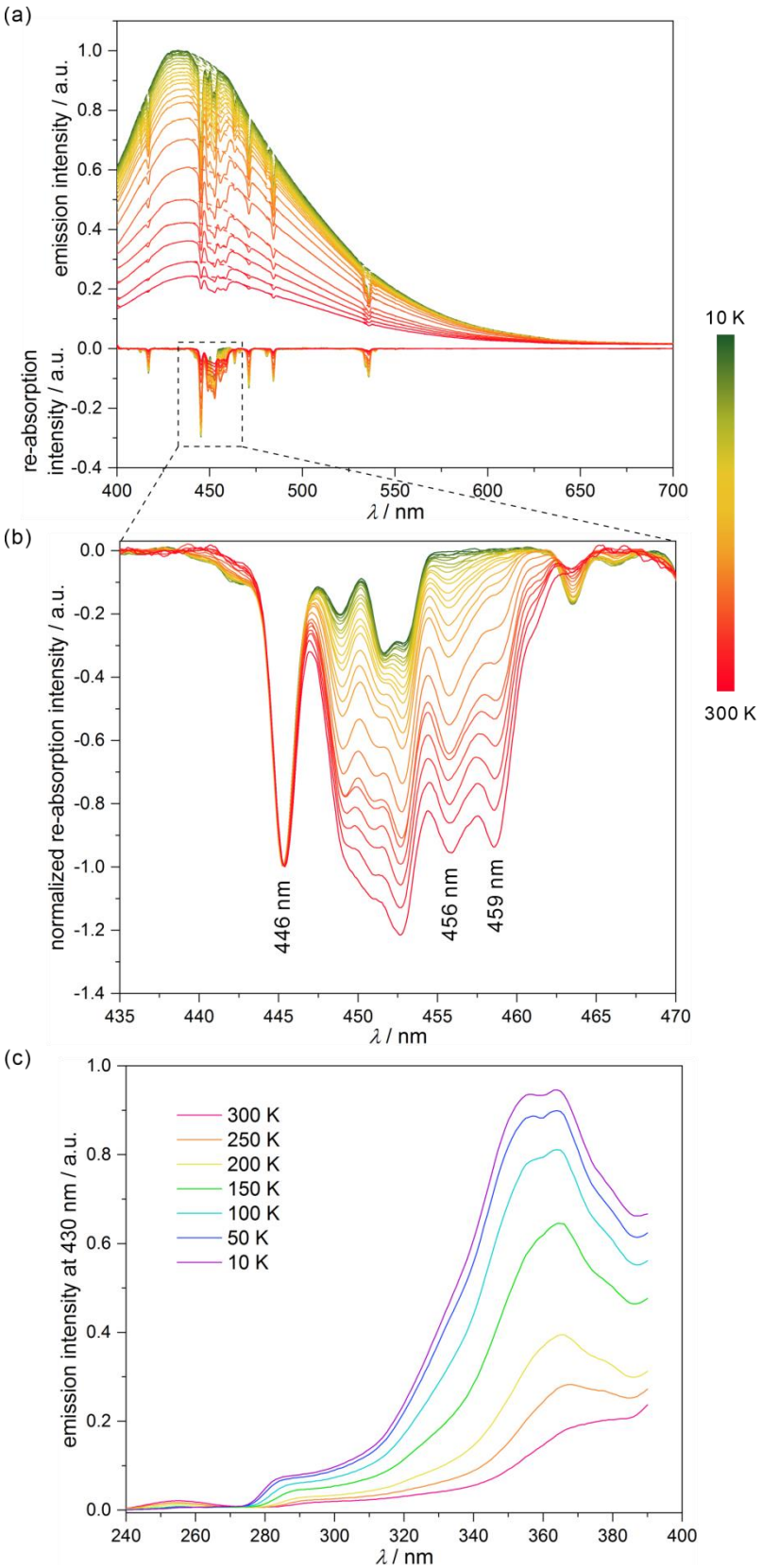

Fig. S31 Temperature-dependent emission spectra of **1@Y** measured under the 370 nm light irradiation along with the extracted luminescent re-absorption spectra obtained after the subtraction of the broad ligand-based emission component (*a*), the enlargement of the re-absorption spectra in the limited range of 435–470 nm showing the most pronounced thermometric effect (*b*), and temperature-variable excitation spectra for the monitored emission at 430 nm (*c*). In (*a*), top part, the dashed lines represent the simulated shape of each ligand emission band while the solid lines represent the experimental emission involving re-absorption effect. The spectra in (*b*) were normalized to the constant re-absorption signal of the distinct peak at 446 nm. The indicated peaks at 446, 456, and 459 nm were employed in the thermometric parameters, Δ (Fig. 5, Table S17).

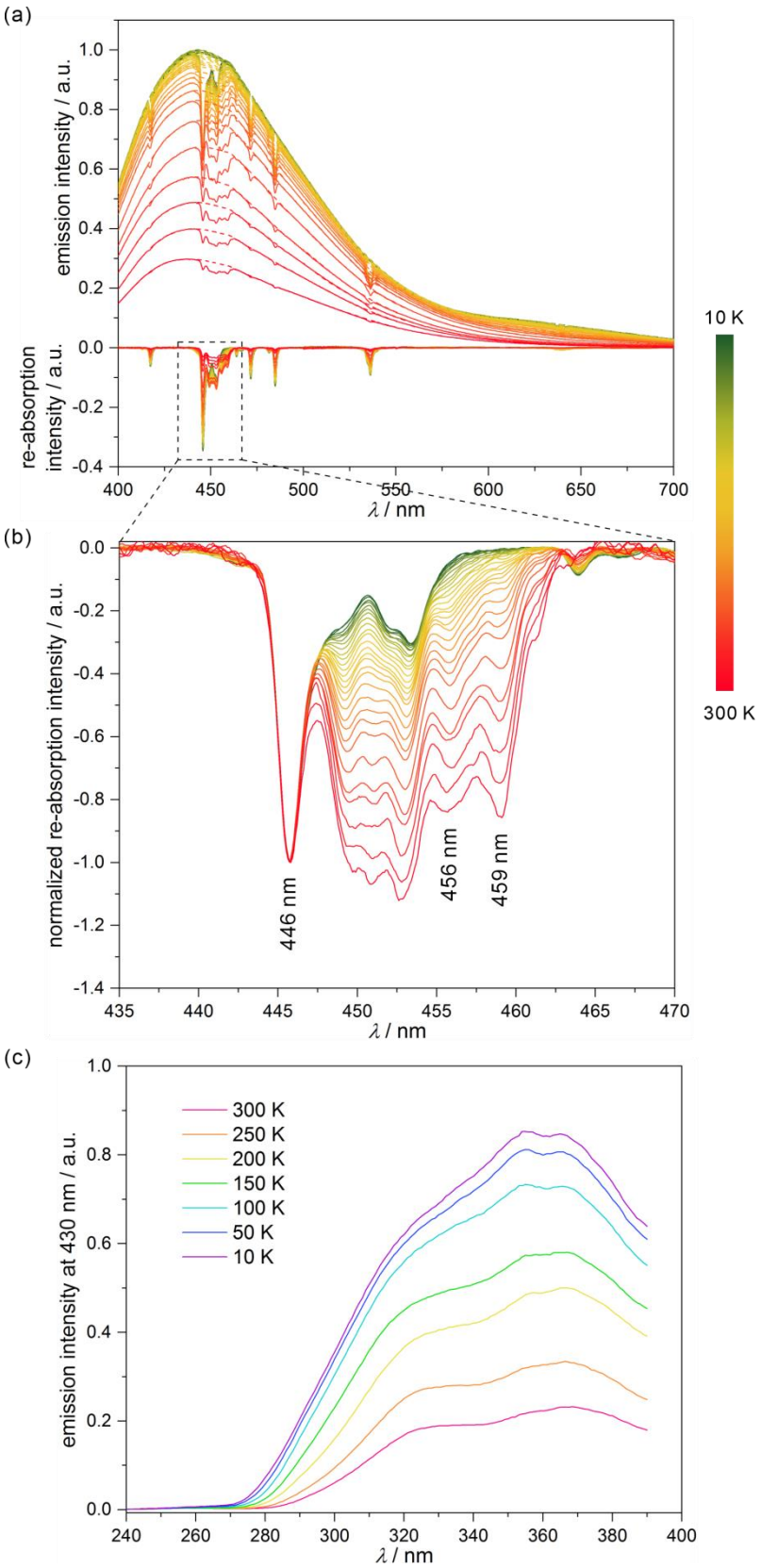

Fig. S32 Temperature-dependent emission spectra of **2@Y** measured under the 360 nm light irradiation along with the extracted luminescent re-absorption spectra obtained after the subtraction of the broad ligand-based emission component (*a*), the enlargement of the re-absorption spectra in the limited range of 435–470 nm showing the most pronounced thermometric effect (*b*), and temperature-variable excitation spectra for the monitored emission at 430 nm (*c*). In (*a*), top part, the dashed lines represent the simulated shape of each ligand emission band while the solid lines represent the experimental emission involving re-absorption effect. The spectra in (*b*) were normalized to the constant re-absorption signal of the distinct peak at 446 nm. The indicated peaks at 446, 456, and 459 nm were employed in the thermometric parameters, Δ (Fig. 5, Table S17).

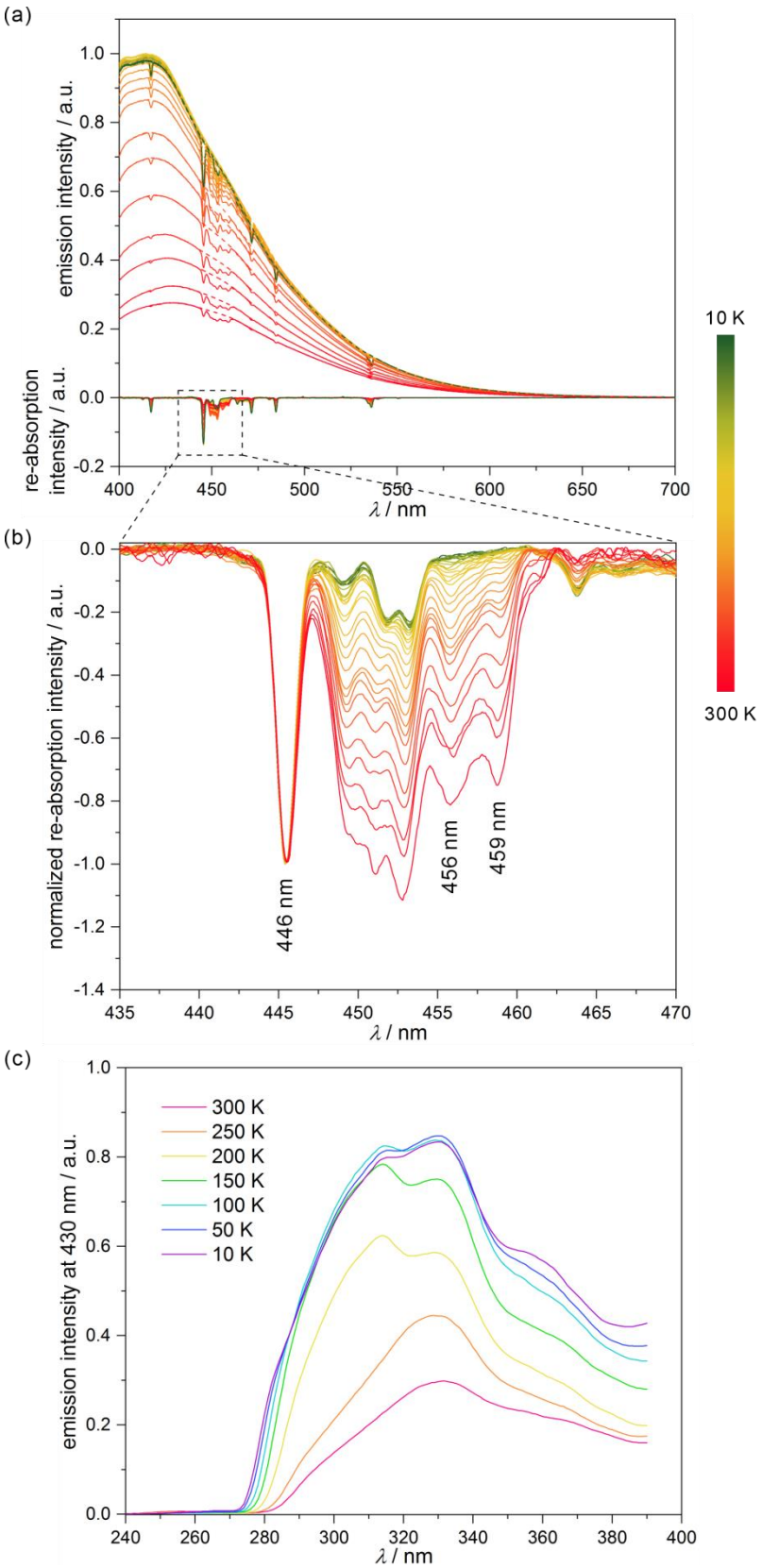

Fig. S33 Temperature-dependent emission spectra of **3@Y** measured under the 350 nm light irradiation along with the extracted luminescent re-absorption spectra obtained after the subtraction of the broad ligand-based emission component (*a*), the enlargement of the re-absorption spectra in the limited range of 435–470 nm showing the most pronounced thermometric effect (*b*), and temperature-variable excitation spectra for the monitored emission at 430 nm (*c*). In (*a*), top part, the dashed lines represent the simulated shape of each ligand emission band while the solid lines represent the experimental emission involving re-absorption effect. The spectra in (*b*) were normalized to the constant re-absorption signal of the distinct peak at 446 nm. The indicated peaks at 446, 456, and 459 nm were employed in the thermometric parameters, Δ (Fig. 5, Table S17).

Table S17 Comparison of the best-fit parameters for the thermometric calibration curves, $\Delta(T)$ according to the equation (2) (see main text) for compounds **1@Y**, **2@Y**, and **3@Y**.

parameter (the equation (2) in the main text)	**1@Y** (Figures 5a and S31)		**2@Y** (Figures 5a and S32)		**3@Y** (Figures 5a and S33)	
	Δ for λ = 456 nm Δ = *Int*(446nm)/ *Int*(456nm)	Δ for λ = 459 nm Δ = *Int*(446nm)/ *Int*(459nm)	Δ for λ = 456 nm Δ = *Int*(446nm)/ *Int*(456nm)	Δ for λ = 459 nm Δ = *Int*(446nm)/ *Int*(459nm)	Δ for λ = 456 nm Δ = *Int*(446nm)/ *Int*(456nm)	Δ for λ = 459 nm Δ = *Int*(446nm)/ *Int*(459nm)
Δ_0	3.5(2)	0.73(9)	4.6(3)	0.63(7)	4.9(4)	1.5(3)
ΔE_v / K	108(2)	305(9)	115(4)	349(7)	129(5)	314(19)
C	–0.955(3)	–0.9939(8)	–0.787(14)	–0.9916(13)	–0.930(4)	–0.9930(10)
$\Delta_{0,\mathrm{corr}} = \Delta_0 / (1 + C)$	78(3)	119(4)	22(2)	75(3)	70(4)	214(6)

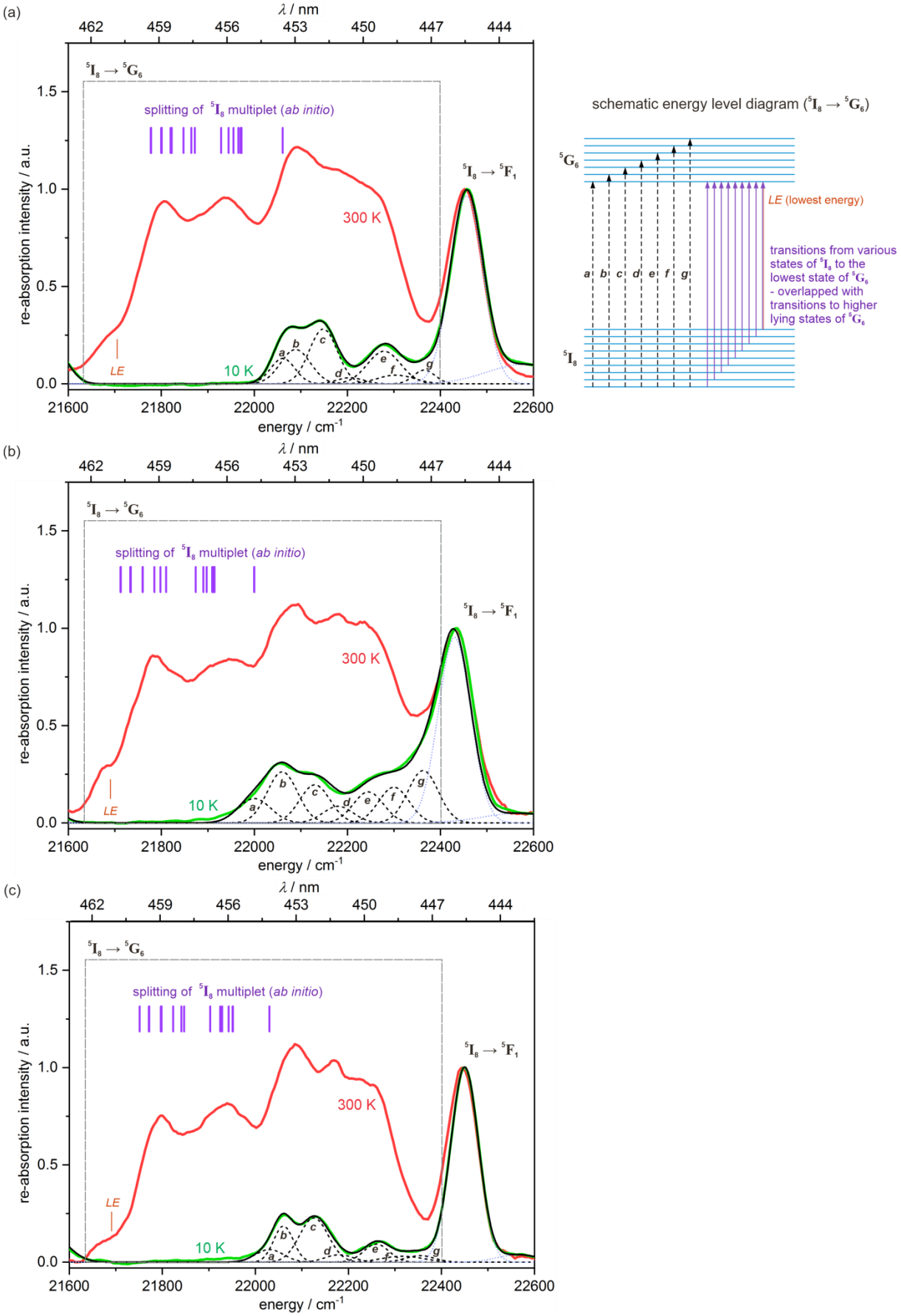

Fig. S34 Comparison of low (10 K) and high (300 K) temperature re-absorption spectra for **1@Y** (*a*), **2@Y** (*b*), and **3@Y** (*c*) in the representative region related to the $^5I_8 \rightarrow {}^5G_6, {}^5F_1$ electronic transitions applied for optical thermometry (see Fig. 4 and S31–S33). The ranges corresponding to the $^5I_8 \rightarrow {}^5G_6$ transitions were indicated by the grey dashed boxes. The low-temperature spectra were deconvoluted into seven components assignable to the electronic transitions from the lowest state of the $^5I_8$ multiplet to various states of the $^5G_6$ multiplet (*a*–*g*). The high-temperature spectra

were compared with the energy splitting of the ground multiplet obtained from the *ab initio* calculations (violet sticks, Table S8). The experimental lowest energy (*LE*) band assignable to the $^5I_8 \rightarrow {}^5G_6$ transitions was depicted by orange colour. On the right side, the schematic energy level diagram depicting the observed electronic transitions was also shown.

Comment to Figure S34 (magneto-optical correlations based on the luminescent re-absorption spectra)

The comparison between low (10 K) and high (300 K) temperature spectra of the luminescent re-absorption effect of **1@Y**, **2@Y**, and **3@Y** (Fig. S34) can be analysed in the context of magneto-optical correlations. Such correlations between magnetic and optical properties are sometimes achievable for luminescent molecular nanomagnets based on lanthanide(III) complexes.[S20–S22] In these cases, lanthanide ions reveal intrinsic photoluminescent properties related to their f-f electronic transitions. Therefore, the emission spectrum is composed of sharp peaks which detailed pattern is the illustration of the crystal-field effect. This enables the correlation between the low-temperature high-resolution emission pattern of the highest energy band (related to the electronic transitions from the emissive multiplet to the ground multiplet) and magnetic properties as the energy difference of the deconvoluted emission peaks represents the energy splitting of the ground multiplet, which is critical for slow magnetic relaxation effects.

The analogous correlation in the case of absorption spectra is much more complicated, and usually impossible, as the low-temperature absorption spectra represent the electronic transitions from the lowest-lying state of the ground multiplet to the multiple states of excited multiplets while the electronic transitions from higher-lying states of the ground multiplet appear only on increased temperature. This leads to the complex absorption spectrum which rarely can provide useful information regarding the energy splitting of the ground electronic multiplet.[S23] The analogous difficulty remains for the reported case of the luminescent re-absorption spectra of **1@Y**, **2@Y**, and **3@Y** (Fig. S34).

We considered the representative region of these spectra related to the $^5I_8 \rightarrow {}^5G_6,{}^5F_1$ electronic transitions which were also applied for optical thermometry (Fig. 4 and S31–S33). As the peak assignable to the $^5I_8 \rightarrow {}^5F_1$ transitions was used for the normalization process, we followed the temperature changes within the bands related to the $^5I_8 \rightarrow {}^5G_6$ transitions. In this range, the low temperature (10 K, LT) re-absorption pattern can be assigned to the electronic transitions occurring exclusively from the lowest-lying state (the quasi-doublet with a very small tunnelling gap as depicted by the *ab initio* calculations, Table S8) of the ground $^5I_8$ multiplet to the series of excited states within the $^5G_6$ multiplet (Fig. S34a). Seven representative components (out of theoretical 13 possible states differing in the m_J composition) were applied in the successful fitting of the related LT emission patterns (Fig. S34). This results in the experimental determination of the excited $^5G_6$ multiplet but does not contain useful information regarding the ground multiplet.

On the contrary, the high temperature (300 K, HT) re-absorption spectra contain the contributions related to the electronic transitions from various states of the ground $^5I_8$ multiplet to the lowest state of the $^5G_6$ multiplet as visualized in the comparison of the HT re-absorption pattern with the energy splitting of the ground $^5I_8$ multiplet obtained from the *ab initio* calculations (Fig. S34, assuming that the bottom of the energy splitting corresponds to the lowest energy peak of the LT spectrum, peak ***a***, as deduced from the schematic energy level diagram).

However, the re-absorption pattern at 300 K contains also the contributions from various states of the ground $^5I_8$ multiplet to the higher lying components of the $^5G_6$ multiplet. Thus, its reliable deconvolution, which may provide the experimental estimation of the anisotropic energy barrier of magnetic Orbach relaxation (related to the energy difference for the two lowest-lying states of the ground multiplet, Fig. 3), is not achievable. Nevertheless, the obtained HT re-absorption pattern seems to confirm the calculated energy splitting of the ground $^5I_8$ multiplet as indicated by the maxima around 21900–21950 cm^{-1} and 21750–21850 cm^{-1} which correspond to the two distinguishable groups of closely lying excited states of the ground $^5I_8$ multiplet (Fig. S34). The more precise experimental determination of the critical energy difference between two lowest-lying states of the $^5I_8$ multiplet demands, for instance, the reliable

indication of the absorption peak assignable to the transitions from the first excited state of the $^5I_8$ multiplet to the bottom of the $^5G_6$ multiplet. It is expected to appear at a relatively low temperature, before the transitions from higher-lying states of the $^5I_8$ multiplet. The related *T*-dependences of the re-absorption peaks suggest that such expected peaks appear upon heating at ca. 456 nm (ca. 21930 cm^{-1}, Fig. S31–S33). However, they are not well distinguished from other accompanying peaks which can be explained by the very close energy position of higher-lying states. This observation stays in perfect agreement with the results of *ab initio* calculations (Fig. 3) but precludes the reliable determination of the anisotropic energy barrier from this pattern.

On the other hand, in the HT re-absorption pattern, the lowest energy component (*LE*, Fig. S34) is relatively well separated from other peaks because it is related to the transition from the highest lying state of the ground multiplet to the lowest-lying state of the $^5G_6$ multiplet. This component is detected as a shoulder on the broad pattern. Therefore, it can provide the rough experimental estimation of the whole energy splitting of the ground multiplet when compared with the lowest energy peak of the LT spectrum (peak ***a***). The resulting estimated energy splitting values are 360, 320, and 330 cm^{-1} for **1@Y**, **2@Y**, and **3@Y**, which is in reasonable agreement with the energy splitting of 280–310 cm^{-1} determined by the *ab initio* calculations (Tables S7–S10). All these findings indicate that the luminescent re-absorption spectra provide useful information regarding the energy splitting of the Ho^{III} ground multiplet which supports the results of *ab initio* calculations, supporting also the interpretation of magnetic relaxation effects in **1**–**3**.

(S20) G. Cucinotta, M. Perfetti, J. Luzon, M. Etienne, P.-E. Car, A. Caneschi, G. Calvez, K. Bernot and R. Sessoli, *Angew. Chem. Int. Ed.*, 2012, **51**, 1606–1610.

(S21) K. Soussi, J. Jung, F. Pointillart, B. Le Guennic, B. Lefeuvre, S. Golhen, O. Cador, Y. Guyot, O. Maury and L. Ouahab, *Inorg. Chem. Front*., 2015, **2**, 1105–1117.

(S22) Y. Xin, J. Wang, M. Zychowicz, J. J. Zakrzewski, K. Nakabayashi, B. Sieklucka, S. Chorazy and S. Ohkoshi, *J. Am. Chem. Soc*., 2019, **141**, 18211–18220.

(S23) K. S. Pedersen, J. Dreiser, J. Weihe, R. Sibille, H. V. Johannesen, M. A. Sorensen, B. E. Nielsen, M. Sigrist, H. Mutka, S. Rols, J. Bendix and S. Piligkos, *Inorg. Chem*., 2015, **54**, 7600–7606.